Accretion Driven Outflows from Black Holes Across the Mass Scale

by

Ashley L. King

A dissertation submitted in partial fulfillment
of the requirements for the degree of
Doctor of Philosophy
(Astronomy and Astrophysics)
in The University of Michigan
2014

Doctoral Committee:

Associate Professor Jon M. Miller, Chair
Professor Joel N. Bregman
Assistant Professor Elena Gallo
Professor Timothy A. McKay
Professor Chris S. Reynolds

“To confine our attention to terrestrial matters would be to limit the human spirit.”

–Stephen Hawking

For Marcia Anne King

ACKNOWLEDGEMENTS

Thanks to Christina King-Wertman, Pablo Damesceno, Michelle Lovasz, Jordan Zastrow, Melissa McClure, Alex Turner, Dan Fabbri, Kate Woods, James King, and all my friends and family for believing and supporting me thru this process.

I would also like to thank Mark Reynolds, Kayhan Gültekin, Nathalie Degenaar, Rubens Reis, Chris Reynolds, Andy Fabian, Dipankar Maitra, Ed Cackett, John Raymond, Tim Kallman, Michael Rupen, Michael Beintenholtz, Steve Allen, Amy Mioduszewski, Vivek Dhawan, Elena Gallo, Enrico Rameriz, Julie Hlavacek-Larrondo, Fiona Harrison, Tim Kallman, Sera Markoff, Cole M. Miller, Enrico Rameriz, and John Tomsick for their help, effort, and contributions during my thesis.

Finally, I would especially like to thank my advisor Jon M. Miller. Without his advice, enthusiasm and overall confidence in me, I would never have strived to such heights. Thanks Jon.

TABLE OF CONTENTS

CHAPTER

LIST OF FIGURES

Figure

LIST OF TABLES

Table

ABSTRACT

Accretion Driven Outflows From Black Holes Across the Mass Scale

by

Ashley L. King

Chair: Jon M. Miller

Accretion driven outflows in the form of highly collimated jets and wide-angle winds carry away immense amount of material and energy from the accretion disks surrounding black holes. During my thesis, I examine the connection between the accretion onto black holes and the resulting outflows that are produced. I begin with two case studies of a supermassive and stellar-mass black hole. In the former, I examine the disk-jet connection, while in the later, I examine the accretion driven winds from the system. Both studies indicate that much can be learned from studying the sources in great detail as well as from comparing the results to other black holes, including their low or high mass counterparts, respectively. As a result, my final study examines both winds and jets across the mass scale. My study indicates that by comparing the outflows across such a large mass range, there is a common dependence of outflow power on bolometric luminosity, i.e., mass accretion rate. Consequently, this relation suggests that winds and jets may be regulated by a common mechanism. In the conclusion of my thesis, I briefly discuss future work that is left to be done in order to understand accretion driven outflows from black holes.

CHAPTER I

Introduction

1.1 Large Scale Interactions

Supermassive black holes in the center of every galaxy (*Richstone et al.*, 1998) have masses that span from a million solar masses to ten billion solar masses (*Gültekin et al.*, 2009b). Though extreme in many ways, a black hole's gravitational "sphere of influence" only extends to a small fraction of its host galaxy, $R_{SoI} = GM_{BH}/\sigma_* = 1.1\left(\frac{M_{BH}}{10^9 M_\odot}\right)\left(\frac{200\text{km/s}}{\sigma_*}\right)\text{pc}$, where σ_* is the velocity dispersion of the host galaxy. Outside of this radius, the self-gravitating force of the bulge of the host galaxy dominates. But there is substantial evidence that the central black holes still interact with their galactic surroundings, despite their small gravitational reach.

Figure 1.1(a) depicts supermassive black hole masses as a function of host galaxy luminosity (*Gültekin et al.*, 2009b). This relation illustrates that the mass of central black hole is not arbitrary when comparing to that of its host galaxy. In fact, the more stellar-light in a galaxy (L), the higher the black hole mass ($M_{BH} \propto L^{1.1}$, *Gültekin et al.*, 2009b). As the stellar-light in each galaxy is a function of the number of stars, and thus the total mass of the galaxy, this relation indicates that the most massive galaxies have the most massive black holes. Though intuitive, the particular slope of this relation is quite informative. It signals that there is a specific coupling in galaxy and black hole formation, whereby the ratio between their masses is well regulated.

Not only does the stellar-light of a galaxy correlate with black hole mass, but the stellar-velocity dispersion does as well. (See Figure 1.1(b), *Gültekin et al.*, 2009b) This illustrates the kinematics is also well coupled to the mass of the central black hole. Energetically, only a small fraction of the black holes rest-mass energy is needed to match the energy in the velocity dispersion of the galaxy, where $\eta M_{BH} c^2 \approx M_{Galaxy} \sigma_*^2$. Typical parameters are $M_{BH} \sim 0.001 M_{Galaxy}$ and $\sigma_* \approx 0.001c$. Therefore η only needs to be $\eta \approx 0.001$ for the energetics to be comparable. Feedback, in the form of radiation, winds and jets from the accreting black holes has been invoked to explain these couplings, as the radiation and outflows carry energy away from the vicinity of the black hole that can reach much greater extents than the gravitational influence of the black hole.

Feedback from the accreting black holes affects extra-galactic structure as well. This is witnessed in "cool core clusters". In these massive clusters with hundreds of galaxies, the X-ray gas suggests that there should be large cooling flows with massive star forming rates in the center of these clusters. This is due to the vast radiative losses and short cooling time scales (*Fabian et al.*, 1994). However, the star formation rates are only on 10-100's of $M_\odot \ yr^{-1}$, suggesting that there is a mechanism that is preventing the rapid star formation (e.g., *Peres et al.*, 1998). In order to resolve this discrepancy, feedback from the central black hole is again invoked.

Simple estimates suggest that the feedback required to produce the $M - \sigma$ and $M - L$ relations or to stop cooling flows in the center of galaxies is viably attainable by either radiation or mechanical feedback (*Fabian et al.*, 2014). However, it is not clear how these mechanisms couple to both the stellar and gaseous components in the bulge and intra-cluster medium. Therefore, in order to better understand how feedback from accreting black holes couples to its surrounds, we first need to understand the physical nature of the feedback mechanisms themselves.

During my thesis, I have focused on the accretion-driven outflows from black holes.

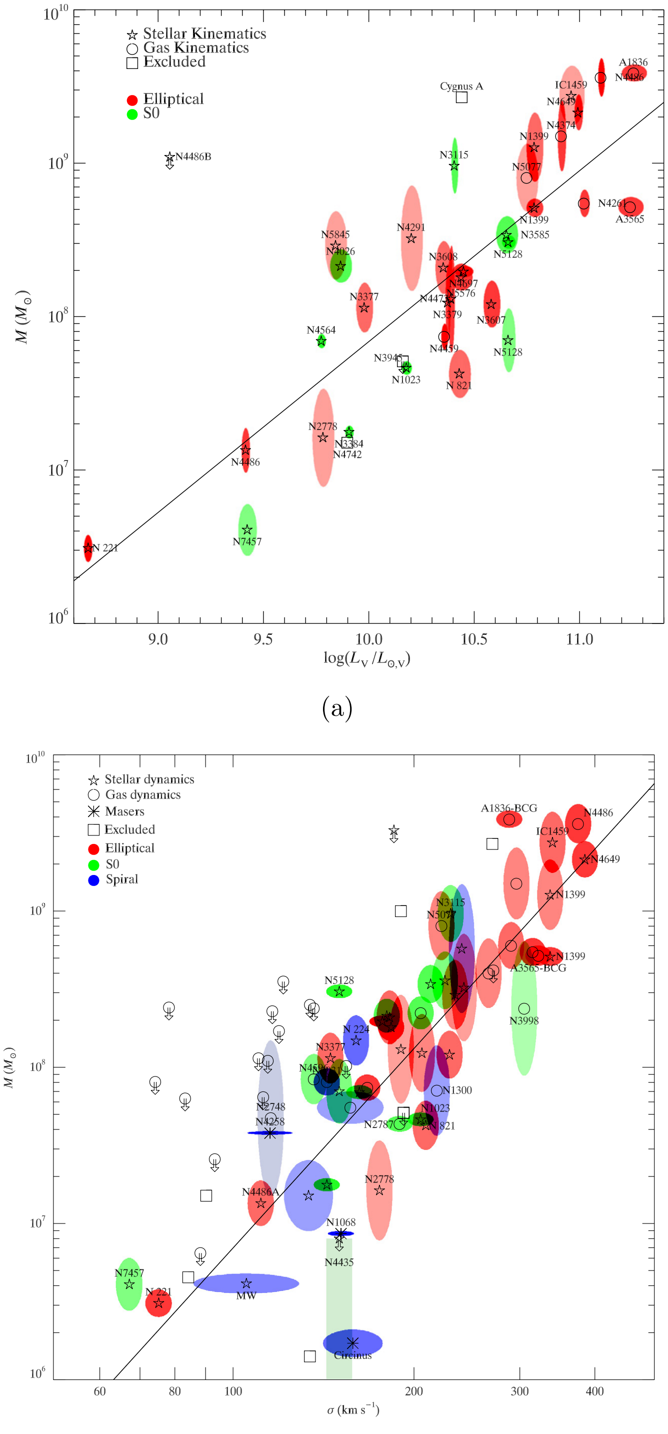

Figure 1.1 The top panel shows the mass of the central black hole versus versus the luminosity of its host galaxy *Gültekin et al.* (2009b). The bottom panel shows the mass of the central black hole versus the velocity dispersion of the bulge component of galaxies *Gültekin et al.* (2009b). These panels demonstrate the connection between the mass of the central black hole and its host properties. Feedback in terms of radiation and mechanical outflows have been invoked to explain these correlations. However, the exact coupling is still being investigated.

Quantifying the nature of these outflows is required to determine how black holes couple to their surroundings, as well as how efficiently a black hole can grow. There is mounting evidence that only a few million years after the Big Bang, there were already extremely large black holes with masses of a few billion solar masses (*Mortlock et al.*, 2011). It is extremely hard to grow a black hole to this size by conventional (sub-Eddington) accretion methods and with accretion driven outflows that remove material from the accretion disk. These outflows not only remove material, but can also heat and ionize the surrounding gas, preventing further accretion onto the black hole. Understanding the exact nature of these outflows is then necessary to determine how efficiently a black hole is fed and precisely how massive a seed is needed to produce a supermassive black hole. This is especially important when determining whether a stellar-remnant or "heavy seed" is required to grow a supermassive black hole (*Volonteri*, 2012).

In the following sections, I will briefly discuss the observational and theoretical constraints we have on the accretion driven outflows from black holes in an aim to characterize the known properties of these power outflows and what is left to be explored.

1.2 Jets

Jets from accreting black holes are highly collimated, bi-polar outflows with relativistic velocities. Structurally, these outflows are typically millions to billions of gravitational radii in length. The collimation of the jets must occur within a few tens to hundreds of gravitational radii (*Doeleman et al.*, 2012), while the acceleration of the jet can occur at much larger radii (*Asada et al.*, 2014). With less than a handful of objects that have resolved jet structures at small scales, the exact nature of the acceleration and collimation of the jets is not well understood. Theoretically, magnetic fields are invoked to collimate and accelerate the jets. In *Lovelace* (1976) and

Blandford and Znajek (1977) magnetic dynamos – generated and driven by the accretion disk – are used to produce a current from which ionized material is accelerated along the jet. The model put forth by *Blandford and Znajek* (1977) taps the angular momentum of the black hole to power the jets. A different jet model has magneto-centrifugal forces accelerate particles along magnetic field lines that are anchored in the accretion disk (e.g., *Blandford and Payne*, 1982). However, in this model, a collimation mechanism is still needed to generate the small opening angles on order of a few degrees that are observed. External pressure gradients in the inter-stellar medium could collimate the outflow, which is suggested by *Heinz and Begelman* (2000), who also suggest jets could be accelerated by small-scale, disordered magnetic fields in the accretion disk.

Though the acceleration and collimation regimes are still observationally under investigation, large-scale structures are well studied. Active galactic nuclei (AGN) jets are divided into two classes: radio-loud and radio-quiet (*McLure and Jarvis*, 2004). Radio-loudness is defined as the ratio between B band and 5 GHz flux densities. Examining the radio-loud class of jets, there is a second morphological division: Fanaroff-Riley I jets are core dominated, low surface brightness jets with edge-brightened flows; Fanaroff-Riley II jets are lobe-dominated and edge-darkened (*Fanaroff and Riley*, 1974). The division between the two morphological regimes tends to occur at an accretion luminosity of $\sim 10^{-3} L_{Edd}$ (*Ghisellini and Celotti*, 2001; *Meyer et al.*, 2011), where L_{Edd} is the Eddington luminosity, $L_{Edd} = 1.8 \times 10^{38} (\frac{M_{BH}}{M_\odot})$. Interestingly, stellar-mass black holes show qualitatively the same structure as AGN in that at low Eddington fractions the jets are unresolved and core-dominated (e.g., *Gallo et al.*, 2003; *Cadolle Bel et al.*, 2011), and at high Eddington fractions, the stellar-mass jets show knot ejections with little to no core emission (e.g., GRS 1915+105 *Mirabel et al.*, 1998; *Mirabel and Rodríguez*, 1999).

The spectral energy density of the emission from these jets generally has a power-law dependence in the radio band, indicating a non-thermal origin. The core jet emission is believed to be composed of a superposition of self-absorbed synchrotron spectra that peak at different frequencies along the jet *Blandford and Konigl* (1979). The resulting composite spectrum is roughly constant in the radio band i.e., $F_\nu \propto \nu^\alpha$; $\alpha \approx 0$ where these self-absorbed spectra overlap. At longer wavelengths, the jet spectrum follows $F_\nu \propto \nu^{5/2}$, corresponding the the tail of the last self-absorbed spectrum. At shorter wavelengths and in the extended jet structures, the emission becomes optically-thin and goes as $F_\nu \propto \nu^{-(p-1)/2}$, where p describes the electron distribution. As is shown in Figure 1.2(a) & 1.2(b), this qualitative behavior of the jet spectrum is observed in both stellar-mass and supermassive black hole jets (*Maitra et al.*, 2011; *Migliari et al.*, 2007). As the mass of the central black hole increases, one can see that the optically thin transition occurs at smaller frequencies (*Falcke et al.*, 2004a).

The jet luminosity not only scales with mass of the black hole, but also with X-ray luminosity. Depicted in Figure 1.3(a) is the radio luminosity of the jet as compared to the X-ray luminosity and mass of the black hole, known as the "fundamental plane of black hole activity" (*Merloni et al.*, 2003). The exact scaling of the radio luminosity goes as $\log L_R = (0.60 \pm 0.11) \log L_X + (0.78^{+0.11}_{-0.09}) \log M_{BH} + 7.33^{+4.05}_{-4.07}$, where L_R is the radio luminosity at 5 GHz, L_X is the 2–10 keV X-ray luminosity and M_{BH} is the black hole mass (*Merloni et al.*, 2003). The radio emission is thought to trace the jet power, where as the X-ray luminosity is thought to trace the accretion luminosity from the disk, which is ultimately set by the accretion rate onto the black hole (*Merloni et al.*, 2003; *Falcke et al.*, 2004b; *Gültekin et al.*, 2009a). The fact that the slope of this relation with respect to both the mass and X-ray luminosity is less than unity, implies that as the black hole accretes at a higher Eddington fraction, i.e., L_X/L_{Edd}, the jet is less efficient at producing radio luminosity in the jet.

It is important to also note that the universality of the relation in Figure 1.3(a),

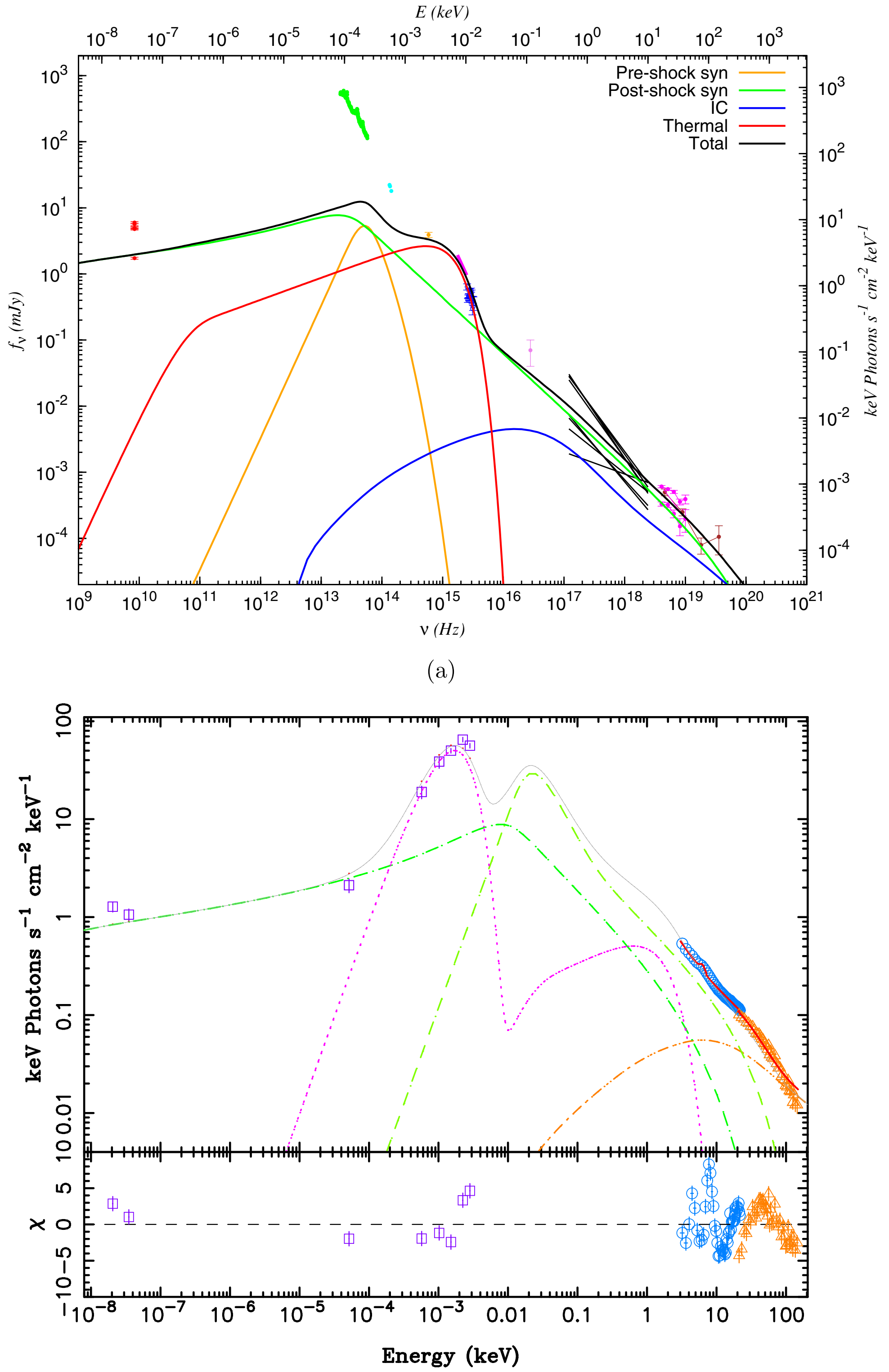

(a)

(b)

Figure 1.2 The top panel shows the broadband SED of AGN, NGC 4051 (*Maitra et al.*, 2011), while the In this model, the bottom panel shows an SED of the stellar-mass black hole, GRS J1655−40(*Migliari et al.*, 2007). The green and orange line in the top panel (green dashed lines in the bottom) show synchrotron emission from the jet. The red line (purple dotted line) is the thermal emission from the accretion disk (and companion), and the blue (orange dotted-dashed) is inverse-Compton from the synchrotron and soft disk photons. The black is the total of all of these components.

as it utilizes both stellar-mass and supermassive black holes, both of which accrete at a range of different Eddington rates. A universal trend need not necessarily be the case, as the local characteristics of the accretion disk vastly vary between stellar-mass and supermassive black holes. For instance, assuming a standard thin-disk (*Shakura and Sunyaev*, 1973), the temperature in the accretion disk scales inversely with mass as $T \propto M_{BH}^{-1/4}$. This is primarily a result of the surface area increasing with mass, allowing for a less dense and cooler accretion disk to surround the most massive black holes. Because there is a universal trend despite these physical differences, it indicates that the relation is set by global processes that regulate the accretion driven jets, i.e., the macro-physics of the system, not the microphysics in the accretion disk.

This is not to say micro-physical properties intrinsic to the accretion disk, like temperature, density or even type of accretion flow, cannot have an influence on this fundamental plane. Figure 1.3(b) depicts the X-ray−radio plane for only stellar-mass black holes (*Gallo et al.*, 2012). Instead of showing a universal trend, *Gallo et al.* (2012) show there are two different X-ray−radio tracks that are statistically significantly separated from each other. The upper track follows a relation that is consistent with the fundamental plane across the mass scale and scales as $L_R \underset{\sim}{\propto} L_X^{0.6}$, while the lower track is much steeper at $L_R \underset{\sim}{\propto} L_X^{1.0}$ (*Gallo et al.*, 2012). Even more interesting is the fact that sources can move from one track or the other. Though the exact nature of the differences between the tracks is still yet to be resolved, speculations on types of accretion flow or jet production may be responsible for the diversity of behavior observed in this $L_R - L_X$ plane. In fact, separate “tracks” or relations may occur in supermassive black holes and could explain some of the large scatter associated with the fundamental plane when including black holes from across the mass scale.

Though the radiation from these jets is easily detectable and gives a rough estimate of the radiative energy that is liberated in these outflows, the total energy loss –

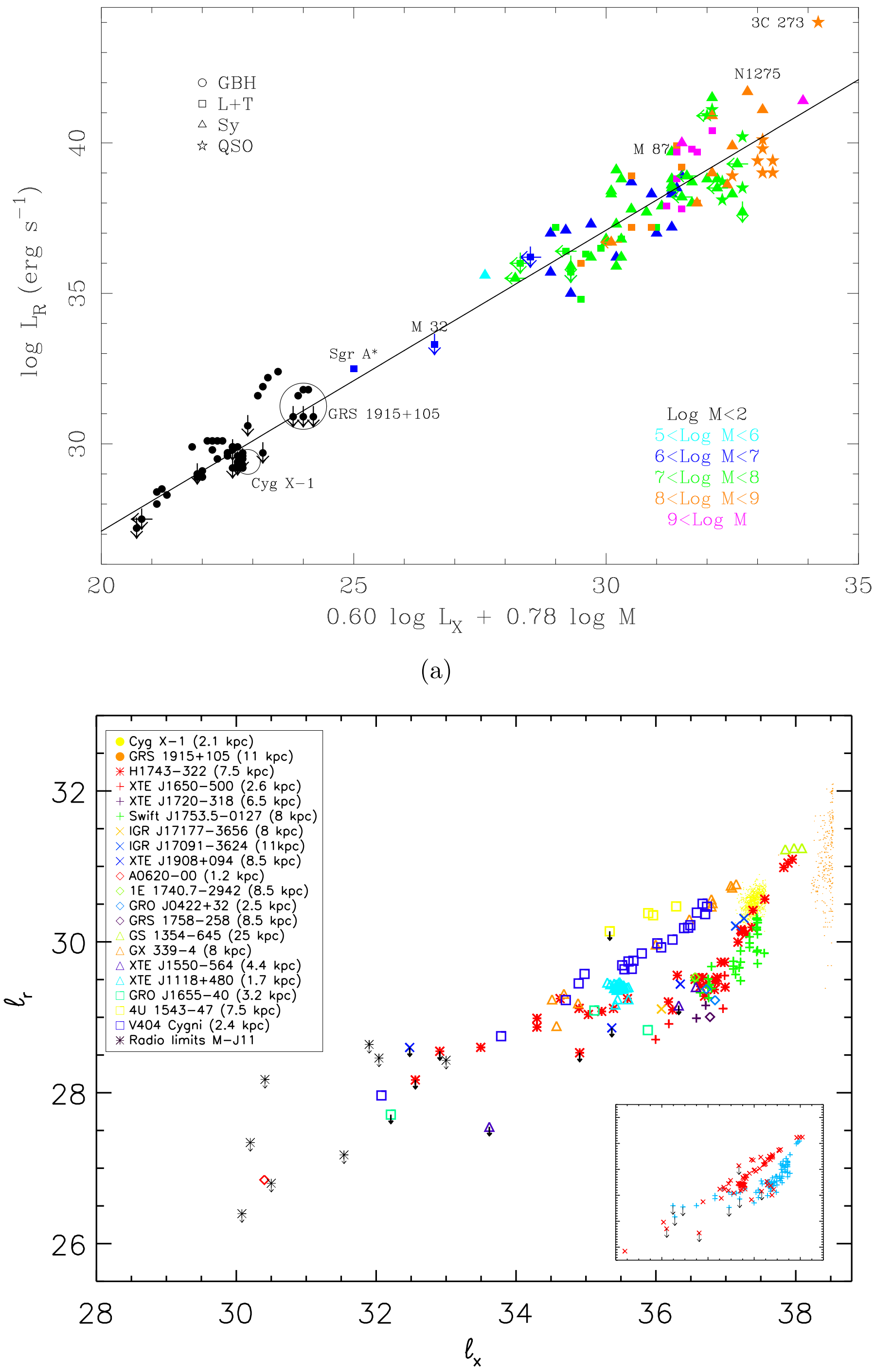

(a)

(b)

Figure 1.3 The top panel shows the "fundamental plane of black hole activity" that plots the radio luminosity versus the mass and X-ray luminosity of black holes across the mass scale *Merloni et al.* (2003). The bottom panel shows the X-ray versus radio luminosity for only stellar mass black holes. The top panel shows the universality of this relation suggesting jet production is set by global properties rather than local gas characteristics in the accretion disk. However, the lower panel demonstrates that though there is a universal correlation, there are several individual sources that follow a distinctly separate relation. Studying the similarities and differences between these two tracks may help to understand the broader physical mechanisms at work.

radiative plus kinetic – is harder to measure. As the mass loading of jets is quite uncertain, it is not a straightforward measurement to calculate the kinetic energy from a jet. However, *Allen et al.* (2006) and *Merloni and Heinz* (2007) have used the radio and X-ray cavities that are carved out by the most massive jets as a calorimeter for the kinetic energy. This method uses the energy needed to inflate these cavities divided by an inflation timescale to estimate the kinetic power of the jets. Though it relies on a time averaged calculation, it is the most direct method available for measuring the kinetic power in jets. *Merloni and Heinz* (2007) found using this method that the kinetic energy of the jets exceeds the radio luminosity by orders of magnitude. (See Figure 1.4). The one stellar-mass black hole where this same method has been utilized has shown a similar trend where the kinetic power is vastly greater than the radiative power. Interestingly, when looking at the sample of AGN, the kinetic power versus radio luminosity relation indicates that more radio luminous a jet has, the less (relative) kinetic energy it puts out, i.e., $\log L_K = (0.81 \pm 0.11) \log L_R + 11.9^{+4.1}_{-4.4}$, i.e., the jets are becoming less kinetically dominated (*Merloni and Heinz*, 2007).

Understanding these relations between X-ray luminosity and radio luminosity in the "fundamental plane" as well as the kinetic power and radio luminosity relation, is vital to uncovering the of physics of jet production. Moving forward, we will need to better constrain these trends with more observations and sources. As in the dual tracks seen in the stellar-mass black holes (*Gallo et al.*, 2012), compiling samples with the best data quality and monitoring campaign has revealed clear structure in the $L_X - L_R$ relation. Determining the differences between sources in each track and why sources switch between tracks will allow us to better constrain the physical processes that are producing this relation (e.g., H 1743−322, *Coriat et al.*, 2011). Further observations of AGN are waiting to reveal structure in these relations that will be vital in determining the mechanisms that generate jets.

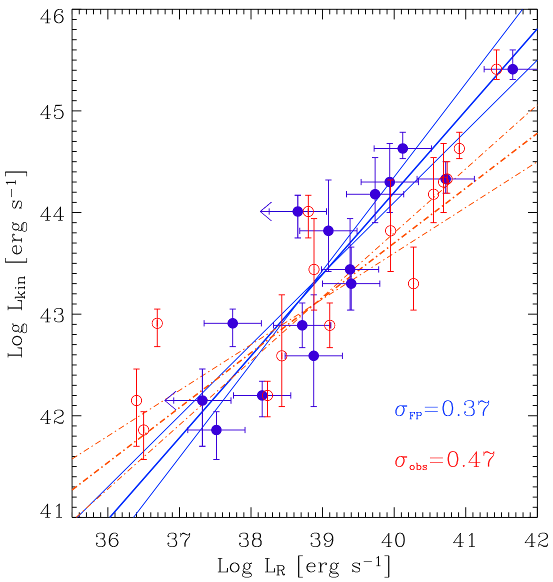

Figure 1.4 This figure shows the jet kinetic energy measured from radio and X-ray cavities versus the radio luminosity *Merloni and Heinz* (2007). The red points are the observed radio luminosity, and the blue data points are the de-beamed.

1.3 Winds

Outflows from accreting black holes are not always as collimated as those observed in relativistic jets. Winds are outflows with a much wider opening angle; they are observed as absorption features against the continuum of the accretion disk in ultraviolet (UV) and X-ray bands (e.g, *Crenshaw and Kraemer*, 2012). They too can span a wide range in scales, from galactic-sized outflows on kpc scales to unresolved flows on sub-pc scales.

Theoretically, winds can be driven by a number of different mechanisms. Radiation from the accretion disk can push on the gas in bound−bound and bound−free transitions. This is most effective when there is a strong UV continuum and the gas is only moderately ionized, so the UV resonance line transitions are accessible (*Proga et al.*, 2000). UV line driving predominantly happens in AGN because the radiation from accretion disk tends to peak in the optical and UV. The X-ray radiation must be weak to prevent over ionization of the gas. However, if the wind is overly ionized, then radiation can accelerate the gas via pressure from electron-scattering, though this is only efficient if the radiative luminosity is above the Eddington limit. Conversely, if the gas is sufficiently cool and dust can form in the gas, then the radiation pressure on dust can be more efficient due to the increased opacity and cross section at short wavelengths. In general, radiation pressure on the gas and dust can be responsible for driving AGN winds, especially the large scale winds observed on kpc scales (*Proga et al.*, 2000). The spectral energy distribution from stellar-mass black hole accretion disks peaks in the X-ray with little contribution at UV wavelengths. This serves to ionize the gas, making radiation pressure an unviable source for driving these winds.

Thermal pressure can also drive winds from an accretion disk, especially in stellar-mass black hole accretion disks. A corona or atmosphere above an accretion disk that is in hydro-static equilibrium will have a thermal distribution of particle velocities. A small portion of these particles will have velocities greater than the local escape velocity and form a wind. X-rays from the continuum will also Compton heat the gas, increasing the particle velocity and generate a stronger outflow from these system (*Begelman et al.*, 1983; *Woods et al.*, 1996). Because high temperatures and X-ray heating are needed to generate a thermal wind, it is predominantly viable in the accretion disks that surround stellar-mass black holes and only in the outskirts of AGN accretion disks where the escape velocity is lowest.

A third pathway for generating accretion driven winds is via magnetic mechanisms, which includes both magneto-centrifugal forces and magnetic pressure. Magneto-centrifugal winds rely on poloidal magnetic field lines that are anchored in the accretion disk, using the disk's rotation to generate the centrifugal force that accelerates the wind (e.g., *Blandford and Payne*, 1982). Toroidal magnetic field lines dominate in magnetic pressure driven winds, accelerating particles as the toroidal field lines are wrapped up because of the rotation of the disk (e.g., *Lovelace*, 1976). Winds from both stellar-mass and supermassive accretion disks can be accelerated via magnetic processes.

Observationally, winds are observed as absorption features from a range of different elemental species, e.g., C, N, O, Ne, S, & Fe. They range in ionization from $\log \xi \sim 0 - 2$, which are observed in the UV, to $\log \xi \gtrsim 5$, which are observed in the X-ray (*Crenshaw and Kraemer*, 2012), where $\xi = \frac{L_{ion}}{nr^2}$, and L_{ion} is the ionizing luminosity, n is the wind number density, and r is the radius from the ionizing source to the absorbing cloud. The ionization is determined by comparing the relative strengths of the absorption lines to each other as well as to predictions from self-consistent photoionization models (*Ferland et al.*, 1998; *Bautista and Kallman*, 2001). The strength of the absorption also varies between sources from very narrow features in warm-absorbers to broad absorption features that have widths of 1000's km s^{-1} in broad-absorption line (BAL) quasars. BAL quasars are typically observed at very high Eddington fractions, and the winds are thought to be driven by radiation pressure on kpc scales (*Gibson et al.*, 2009). Warm-absorbers are observed in Seyfert galaxies (*Reynolds*, 1997), and are located on pc scales. Warm-absorbers could be driven by radiation pressure or from magnetic processes depending on their launching radius and the geometry of the outflow.

The column density inferred from the absorption lines is associated with an increase in the ionization of the absorbing gas. Figure 1.5 shows this relation from *Crenshaw and Kraemer* (2012), which plots column density versus ionization. An increase in the column density as a function of ionization suggests that the highest ionized gas is removing more material. It also suggests that the wind is being emitted at smaller radii when both the ionization and column density increases, as the ionization scales as $\xi \simeq \frac{L_{ion}}{N_H r}$, if the size of the absorbing cloud is on order of the radius of the cloud from the ionizing continuum, i.e. $N_H = n\Delta r$, where $\Delta r \approx r$.

Winds not only vary in size and strength between sources but also in individual sources as well. Variability is observed on timescales as short as days, but on average

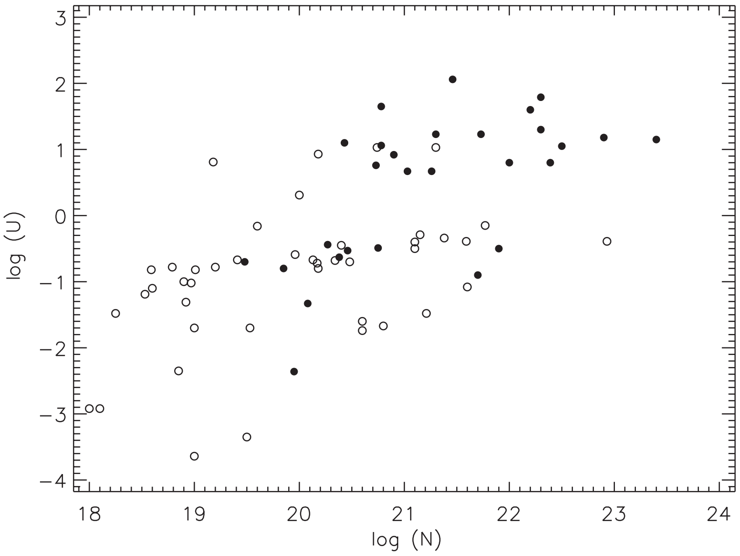

Figure 1.5 This figure taken from *Crenshaw and Kraemer* (2012) shows the ionization, $\log U \simeq \log \xi - 1.5$, versus column density from AGN warm-absorbers. The plot indicates a positive correlation between ionization and column density, suggest that the more ionized material carries away more material as is located at smaller radii, i.e.,$\xi \simeq \frac{L_{ion}}{N_H r}$

variability occurs on weekly to monthly timescales (*Krongold et al.*, 2007; *King et al.*, 2013b; *Miniutti et al.*, 2014). The variability in each source may be the result of dissipation of the absorbing cloud, response to the ionizing continuum or motion across our line-of-sight. The later is supported by the velocities of the winds that are detected as blue shifts from the rest frame energy of each line species. The line-of-sight velocities range from a few 100 km s^{-1} (*King et al.*, 2013c; *Crenshaw and Kraemer*, 2012) to a few percent of the speed of light (*Tombesi et al.*, 2013; *King et al.*, 2012b). The highest velocities are typically associated with the highest ionization and therefore closest to the black holes (*Tombesi et al.*, 2013).

1.4 Relationship Between Winds and Jets

Though wide-angle winds and highly collimated jets can be found in the same source, they are not necessarily observed at the same time. This is especially true of stellar-mass black holes. Winds and jets appear to be mutually exclusive (*Miller et al.*, 2006b; *Neilsen and Lee*, 2009; *Miller et al.*, 2012) and associated with particular accretion states. Jets in stellar-mass black holes are associated with very sub-Eddington accretion, i.e., low luminosity. This type of accretion is usually associated with an advection dominated accretion flow (ADAF) that has a geometrically thick structure (e.g., *Narayan and McClintock*, 2008). In addition, a thick disk is thought to be necessary to anchor sufficiently strong magnetic fields to generate and collimate jets (*Reynolds et al.*, 2006). This accretion state is typically referred to as the "low/hard" state as the luminosity is relatively low and the X-ray spectral index is hard at $\Gamma \lesssim 2$.

During this low/hard state, the jet emission and accretion luminosity follow the aforementioned fundamental plane of black hole activity. The jet emission is typically unresolved compact radio emission that is optically thick. When the accretion rate rises and approaches the Eddington limit (though still spectrally hard), the jet emission becomes optically thin and discrete knots are ejected (*Fender and Belloni*, 2012). This X-ray state is known as the "very high state" and is associated with relativistic and even apparently superluminal jet emission (*Mirabel et al.*, 1998; *Mirabel and Rodríguez*, 1999).

At high Eddington fractions, when the spectra is no longer hard and becomes dominated by the thermal component from the accretion disk instead of a hard power-law, winds are observed in the X-ray band. This state is denoted as the "high/soft" state and is thought to have accretion via a "standard" optically thick, geometrically thin accretion disk (*Shakura and Sunyaev*, 1973). A typical transient X-ray binary is shown to traverse these three different accretion states in Figure 1.6(a) (*Fender and Belloni*, 2012). The associated outflows are denoted in the bottom three panels.

We have yet to observe both winds and jets simultaneously in a stellar-mass black hole. This suggests the two outflows are integrally related due to their mutual

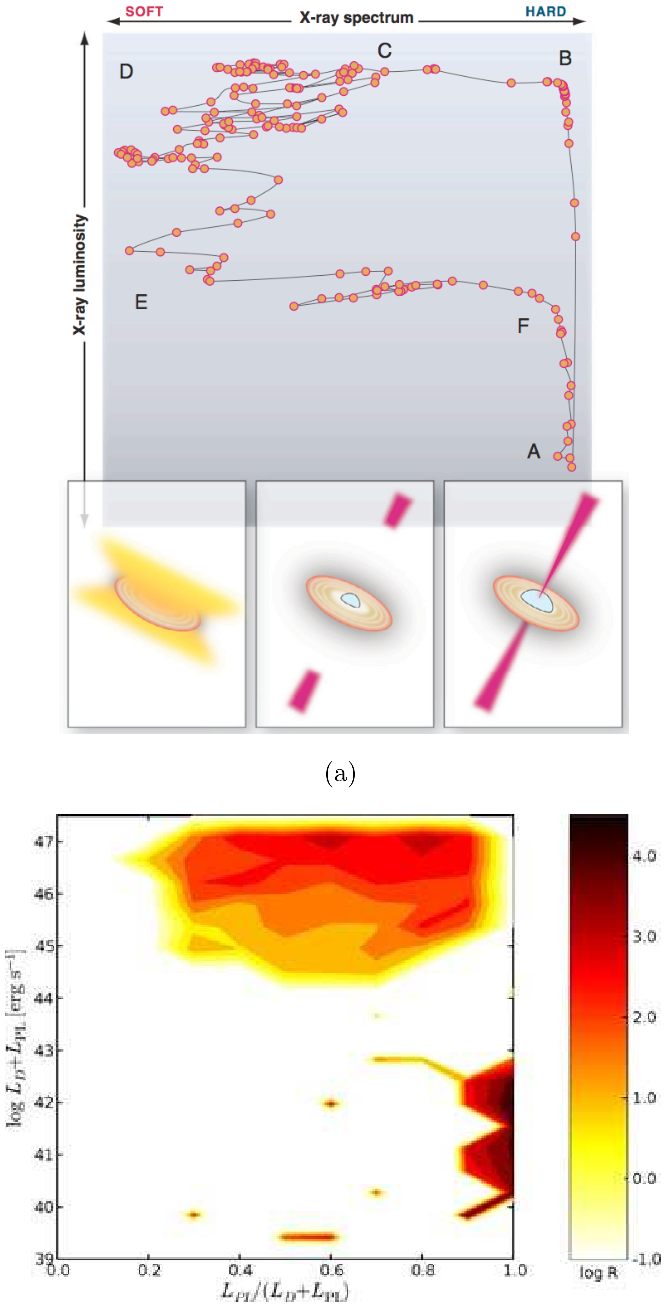

(a)

(b)

Figure 1.6 **a)**The top panel shows the hardness intensity diagram for a stellar-mass black hole. It plots the hardness ratio which denotes the contribution from the phenomenological powerlaw component (hard) to the thermal disk component (soft) versus the luminosity of the source. The three lower panels indicate the type of outflows associated with each hardness regime, with jets being at hard to intermediate range and winds being at soft spectral types. (*Fender and Belloni*, 2012) **b)** This figure is qualitatively the same as the top panel, but shows the radio-loudness of AGN as a function the hardness intensity diagram. The darker the color the more radio-loud and prominent the jet is in this diagram. One can see that AGN generally fill out the same qualitative parameter space as stellar-mass black holes. (*Körding et al.*, 2006) exclusiveness. *Neilsen and Lee* (2009) suggest that winds quench the jets by removing material from the most inner parts of the accretion disk that fuel the jets. In such a scenario, we might be able to observe both outflows at the same time when winds first initiate. Conversely, winds and jets could be one and the same and simply a function of collimation, where changes in accretion geometry and flow brings about changes in collimation and funneling ability of the magnetic fields. This is assuming the winds and jets are both generated via magnetic mechanisms, where the former scenario does not assume anything about the outflow generating mechanism.

In supermassive black holes, winds and jets generally follow this same trend, where winds are observed in AGN with softer X-ray spectra and at a relatively high Eddington fraction, i.e., Seyferts (e.g, *Crenshaw and Kraemer*, 2012). Conversely, compact jets are observed in low Eddington sources (*Körding et al.*, 2006). Jets with discrete knots are observed in the highest Eddington fractions, also similar to stellar-mass black hole jet activity. Figure 1.6(b) shows a hardness intensity diagram for AGN for comparison to stellar-mass black holes. This figure shows that AGN follow the same spectral (i.e., accretion) behavior as stellar-mass black holes and their respective outflows occur in qualitatively the same regions as denoted in stellar-mass black holes in Figure 1.6(a). The color bar denotes radio loudness, indicating the strongest jets occur when the power-law component dominates. The main difference in AGN outflows is that winds and jets can co-exist (e.g., *King et al.*, 2011, 2012a), albeit one outflow is generally more dominant than the other. This could be a result of physically different launching mechanisms on the different black hole scales or simply a sensitivity limit that biases detections against stellar-mass black holes.

1.5 Overview of the Thesis

In my thesis, I examine the nature of accretion driven outflows with a focus on determining the underlying physics at work. In Chapter II, I examine the disk-jet connection in Seyfert NGC 4395. This study is aimed at understanding the interplay between the material and energy that is accreted into the black hole and how it correlates to the jet that is produced. It utilizes X-ray and radio observations in order to examine the mass accretion rate and jet power, respectively. This type of case-study has been undertaken in many stellar-mass black holes, but the same accessible timescales are too long in most supermassive black holes. NGC 4395 is the smallest black hole hole with a robust mass measurement, making it the ideal candidate for this study. The goal of the study is to examine whether supermassive black holes follow the same fundamental plane in individual sources as do stellar-mass black holes.

In Chapter III, I examine the accretion driven winds in the stellar-mass black hole, IGR J17091−3624. In this work, the goal is to examine and test the accretion state dependence of outflows in stellar-mass black holes. I discover winds during the "high/soft" state which gives support to the current paradigm. These winds are located within a few thousand gravitational radii, and are outflowing at a few percent of the speed of light. The winds also place strong constraints on the launching mechanisms, delving into the physics behind the disk-wind connection in stellar-mass black holes. In addition, the high velocity winds resemble those of several AGN's, and suggests a connection between wind production across the mass scale.

In Chapter IV, I examine the accretion disk outflows across the mass scale. This builds off a number of different studies that examine jet production as a function of mass and mass accretion rate, but takes the relations one step further to include wind production as well. This work begins to reveal the importance of examining both types of outflows, as the connection between them and their environment is crucial to understanding accretion driven feedback.

Finally, in Chapter V, I will briefly summarize these studies in the context of disk-jet-wind couplings. I will then discuss where the current field is headed and what major questions need to be answered. I will discuss how current and future instruments and observations can answer these open questions.

CHAPTER II

A Distinctive Disk-Jet Coupling in the Lowest-Mass Seyfert, NGC 4395

Ashley L. King[1], Jon M. Miller[1], Mark T. Reynolds[1], Kayhan Gültekin[1], Elena Gallo[1], Dipankar Maitra[1]

[1]Department of Astronomy, University of Michigan, 500 Church Street, Ann Arbor, MI 48109-1042, ashking@umich.edu

2.1 Abstract

Simultaneous observations of X-rays and radio luminosities have been well studied in accreting stellar-mass black holes. These observations are performed in order to understand how mass accretion rates and jetted outflows are linked in these individual systems. Such contemporaneous studies in supermassive black holes (SMBH) are harder to perform, as viscous times scale linearly with mass. However, as NGC 4395 is the lowest known mass Seyfert galaxy, we have used it to examine the simultaneous X-ray (*Swift*) and radio (VLA) correlation in a SMBH in a reasonably timed observing campaign. We find that the intrinsic X-ray variability is stronger than the radio variability, and that the fluxes are only weakly or tentatively coupled, similar to prior results obtained in NGC 4051. If the corona and the base of the jet are one and

the same, this may suggest that the corona in radio-quiet AGN filters disk variations, only transferring the strongest and/or most sustained variations into the jet. Further, when both NGC 4395 and NGC 4051 are placed on the stellar-mass L_X-L_R plane, they appear to reside on the steeper L_X-L_R track. This suggests that SMBHs also follow two distinct tracks just as stellar-mass black holes do, and supports the idea that the same physical disk-jet mechanisms are at play across the mass scale.

2.2 Introduction

Observations have revealed a plane connecting the X-ray and radio luminosity of black holes that spans the mass scale: the fundamental plane of black hole activity (*Merloni et al.*, 2003; *Falcke et al.*, 2004a; *Gültekin et al.*, 2009a; *Plotkin et al.*, 2012). This plane suggests there is an underlying physical mechanism driving the relation, which acts across the mass scale (A similar relation across the mass scale is also seen in black hole disk-winds and is consistent with disk-jet power relations, *King et al.*, 2013c). In the fundamental plane of black hole activity, the black hole mass is thought to set a limit to the amount of power that can be extracted from the system. The radio luminosity is taken to be a rough proxy for the jet power as the emission is thought to be synchrotron emission along the jet. Finally, the X-ray luminosity is either directly associated with accretion rate (e.g., *Merloni et al.*, 2003) or with the base of the jet (e.g., *Falcke et al.*, 2004a; *Plotkin et al.*, 2012).

In stellar-mass black holes one can examine how individual sources move across this fundamental plane, as the timescales for variations are particularly short (e.g., *Corbel et al.*, 2003; *Gallo et al.*, 2003, 2012; *Corbel et al.*, 2013). However, the viscous times on which stellar-mass black holes have been probed scale with mass, resulting in relatively long observing campaigns for all but the smallest of SMBHs.

Fortunately, there are a select few low-mass SMBHs with short enough viscous timescales for a simultaneous observing campaign. In particular, the Seyfert NGC

4395 is the smallest mass SMBH whose mass has been measured with reliable, reverberation mapping techniques. NGC 4395 has a mass of $M_{BH} = (3.6 \pm 1.1) \times 10^5 M_\odot$ (*Peterson et al.*, 2005) and is accreting at <0.1% of its Eddington luminosity (e.g., *Shih et al.*, 2003). It has a very variable X-ray flux (e.g. *Nardini and Risaliti*, 2011) and harbors a compact, non-thermal radio source (*Wrobel and Ho*, 2006), making it ideal for a simultaneous campaign aimed to examine the disk-jet connection in an SMBH.

We present the results of a nearly-simultaneous *Swift* X-ray and Karl G. Jansky Very Large Array (VLA) radio observing campaign. We begin with a brief description of the observations taken, followed by a discussion of the correlation between the two bands. We end by discussing the relation of NGC 4395 with other Seyferts as well as its stellar-mass counter parts.

2.3 Observations

2.3.1 Radio

As part of our radio-X-ray monitoring campaign, 16 radio observations were taken with the VLA from 11 June 2011 to 06 August 2011 with an average spacing of 3.7 days. The data were taken at 8.4 GHz with 256 MHz bandwidth in the A configuration. This gave a beam size of $\sim 0.29\,\mathrm{arcsec} \times 0.26\,\mathrm{arcsec}$. 3C 286 was used as the flux calibrator and J1242+3720 was used as the phase calibrator. We adopted the flux scale Perley-Butler 2010. Approximately 15 minutes were spent on source, NGC 4395, during each observation. The residuals reached an rms of approximately 2×10^{-5}Jy/beam. We used CASA version 3.4.0 (*McMullin et al.*, 2007) to perform standard flagging, and to create a primary beam corrected image. We utilized the *clean* routine with natural weighting of the visibilities. The images showed unresolved point sources and were fit with `imfit`. The errors reported include the observational errors and a 3% systematic error added in quadrature. Although, this systematic error is relatively small, we note that the phase calibrator in Figure 2.1(a) shows a vary stable flux density, with an rms at $< 3\% \langle F_\nu \rangle$. In addition, the flux calibrator 3C 286 is known to be extremely stable (*Perley and Butler*, 2013), which is a necessity for this study. The flux-densities are shown in Figure 2.1(a), divided by the mean flux-density, which for NGC 4395 is $\langle F_R \rangle = 5.6 \times 10^{-4}$ Jy.

2.3.2 X-rays

The 50 X-ray observations were taken with *Swift* in the photon counting mode on 5 June 2011 to 9 August 2011 with an average spacing of 1.3 days. The observations had approximately 1 ks exposures, and an average count rate of 0.13 cts s^{-1}, with a minimum count rate of 0.016 cts s^{-1}, and a maximum count rate of 1.08 cts s^{-1} in the 0.3-10 keV band. See Figure 2.2(a).

To analyze the data, we used `XSPEC` (v. 12.8.0) (*Arnaud et al.*, 1999) and `FTOOLS` (v. 6.13) (*Blackburn*, 1995). We used the standard `xrtpipeline` with the current response files from `CALDB` (v. 4.5.1). Exposure maps were generated with `xrtexpomap` and ancillary response matrices were made with `xrtmkarf`. The ungrouped spectra were fit to a phenomenological power-law and two absorption components (`tbabs` × `tbabs` × `power-law`) in `XSPEC` using *cstat* statistics (*Cash*, 1979). The average cstat per degree of freedom is $cstat/dof = 0.40$. The background was included as an annulus around the point source with inner radius of 140" and outer radius of 210", but in general the position and size of the background did not strongly affect our fits. The first absorption component was frozen at N_H=1.85×10^{20} cm^2 (*Kalberla et al.*, 2005), the Galactic column density, while the second absorption component was allowed to vary to model the neutral absorption within NGC 4395 (See Figure 2.2(b)). Although the neutral absorption is highly variable, it primarily affects the low energy part of the spectrum, thus limiting the impact in the unabsorbed flux

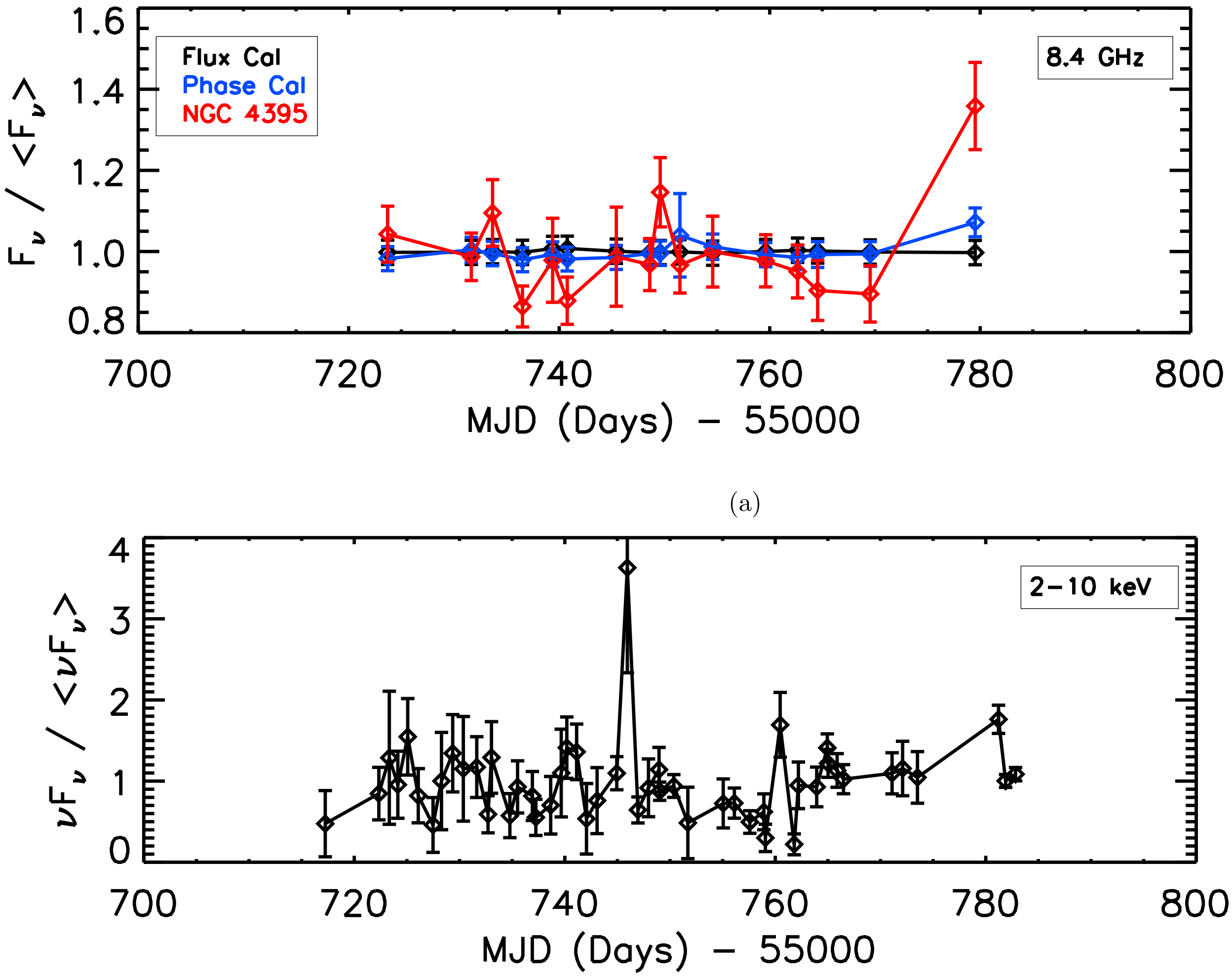

(a)

(b)

Figure 2.1 a) This plot shows the radio variability of NGC 4395 (red) at 8.4 GHz. The flux calibrator (3C 286) is shown in black, and the phase calibrator (J1242+3729) is shown in blue. The flux densities are divided by the mean ($\langle F_R \rangle = 5.6 \times 10^{-4}$ Jy) for easy comparison with the X-ray variability shown in Figure 2.1(b). b) This plot shows the X-ray variability light curve for the unabsorbed 2–10 keV *Swift* band. The X-ray flux is also divided by the mean of the observations, $\langle F_X \rangle = 8.2 \times 10^{-12}$ ergs cm^{-2} s^{-1}.

measurements in the 2–10 keV range we are concerned with.

We froze the power-law spectral index at $\Gamma = 1.8$ due to the small number of counts, while still varying the normalization. Although some of the literature on NGC 4395 finds a much lower spectral index of $\Gamma \lesssim 1.5$ (e.g., *Lira et al.*, 1999; *Shih et al.*, 2003; *Moran et al.*, 2005; *Iwasawa et al.*, 2010), a higher spectral index, $\Gamma \approx 2.0 \pm 0.2$, was found by *Nardini and Risaliti* (2011) when fitting an averaged *Swift/BAT* spectrum above 10 keV. This suggests that the hard spectral index at low X-ray energies is partly due to absorption and not intrinsic. Further, in Figure 2.2(c) we show the confidence contours when we allow the spectral index and column density to both vary in one particular observation. The power-law index is consistent with a wide range of values, including $\Gamma = 1.8$ at better than 1σ confidence, and the column density is constrained to a high column, i.e. $> 1 \times 10^{22} cm^{-2}$. Finally, we note that when we fit our *Swift* data with $\Gamma = 1.5$, the resulting variability analysis does not change within 1 σ statistical errors, as we are mainly concerned with the unabsorbed flux between 2–10 keV.

Important to our campaign is the unabsorbed continuum flux which is shown in Figure 2.1(b), as the flux divided by the average flux. This shows the amount of intrinsic variability of the X-ray emission, which can be easily compared to the radio variability shown in Figure 2.1(a).

2.4 Analysis

2.4.1 Cross-Correlation Timing Analysis

The variability in this data set is primarily seen in the X-ray and has a standard deviation, σ, divided by the mean, $\langle F_X \rangle$, of $\sigma / \langle F_X \rangle = 0.51$ (Figure 2.1(b)) The radio observations are less variable but do show statistically significant fluctuations. Three data points are above 2σ deviations from the mean, with the very last data

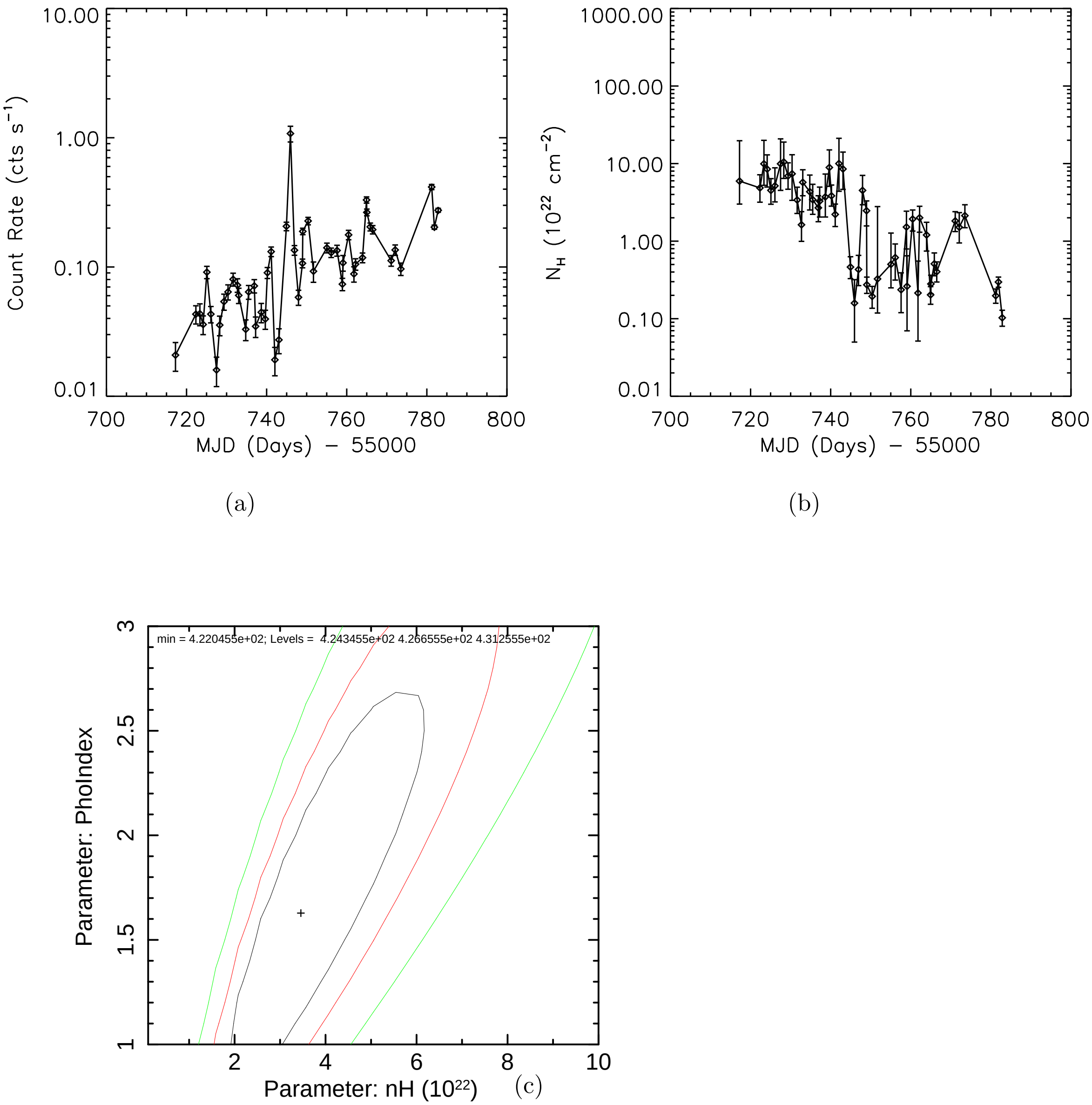

(a)

(b)

(c)

Figure 2.2 a) This plot shows the total (absorbed) count rate from the *Swift* observations. An increase in total count rate is observed throughout the campaign. This is consistent with the total column density changing by nearly two order of magnitude (See Figure 2.2(b)), rather than the intrinsic continuum changing by the same order of magnitude (See Figure 2.1(b)). b) This plot shows the column density (N_H) varying throughout the course of the observations. c) This plot shows the confidence contours when the column density and spectral index are allowed to vary in one particular observation (mjd=55740.2), with contours at 1, 2, & 3 σ confidence levels. The column density is constrained to be a relatively high column density.

point deviating from the mean by over 3.3σ. See Figure 2.1(a). Using a normal distribution of fluctuations, one would expect only one data point to be above a 2σ deviation out of 16, suggesting the fluctuations we do see are real. In the radio data, the standard deviation divided by the mean flux-density is $\sigma/\langle F_R \rangle = 0.12$. These standard deviations are each dominated by the intrinsic variability rather than the measurement uncertainties.

We also checked for any apparent time-lags between the X-ray flux and the radio flux-density variability, which could influence our correlation analysis. We used the z-transformed discrete correlation function with a minimum of 11 data points per bin to determine a time lag (*Alexander*, 2013). See Figure 2.3. We find no evidence of a time lag, as there were no statistically significant correlation coefficients different from zero at a 5σ confidence level. This was determined by dividing each correlation coefficient by its minus side error.

2.4.2 X-ray vs. Radio Correlation

Because the data are consistent with no time lag, we used the nearly simultaneous X-ray and radio observations in our correlation analysis. The average temporal separation between the X-ray and radio observations was 0.55 days, with a maximum separation of 1.6 days. When correlating the data, we find a Spearman's ρ correlation coefficient of $\rho = 0.18$ with a null probability of $p = 0.51$, and a Kendall's τ correlation coefficient of $\tau = 0.15$ with a null probability $p = 0.42$. The correlation test indicates that the weak correlation is not statistically significant.

The X-ray flux versus the radio flux-density is plotted in Figure 2.4(a). As the ranking correlation suggested only a weak correlation, we fit the data with a linear relation. We found that the data are consistent with a flat relation but were also consistent with the fundamental plane given by the red dashed line. We used a bootstraping analysis to determine the linear-fit coefficients. Figure 2.4(b) shows the

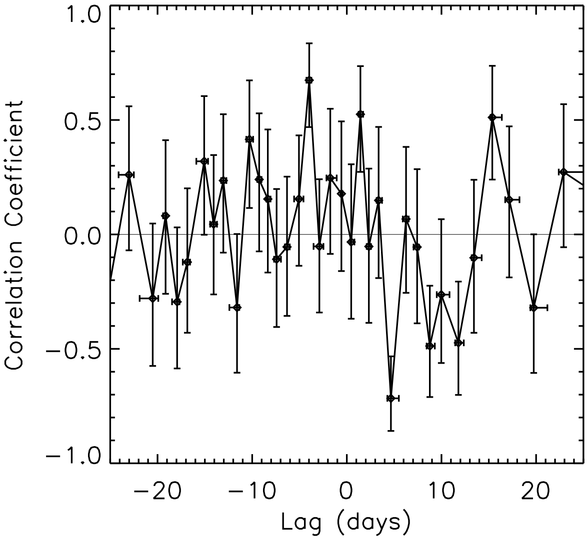

Figure 2.3 This plot shows the z-transformed discrete correlation function for the X-ray fluxes versus radio flux-densities (*Alexander*, 2013). We do not find any evidence of a statistically significant ($> 5\sigma$) delay in the times series.

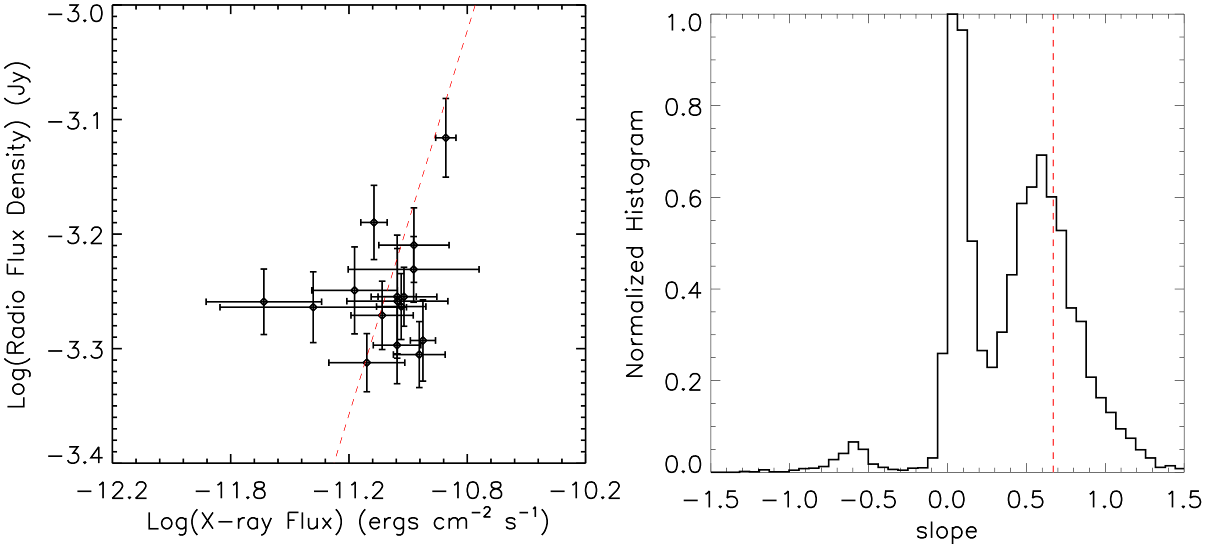

(a)

(b)

Figure 2.4 a) This plot shows the X-ray flux versus the radio flux-density. The red dashed line has a slope of the fundamental plane of black hole activity (*Gültekin et al.*, 2009a). b) This is a histogram of the slopes from a bootstrap of N=10^4 resampling of the data shown in Figure 2.4(a). The peak is at m =0.06. The slope is driven by the the lowest X-ray flux at $\log F_{X-ray} = -11.61$ and the highest X-ray flux at $\log F_{X-ray} \approx -10.84$ as shown in Figure 2.4(a). This is evidenced by the two main peaks at $m = 0.06$ and $m = 0.60$ and the small tail at $m < 0$. The red dashed line is the slope 0.67 of the FP (*Gültekin et al.*, 2009a).

normalized histogram of the 10^4 bootstrap re-samplings of the data, and the resulting slope, m, from these linear fits. There is a peak in the distribution at $m = 0.06$, a second broad peak at $m = 0.6$, and a small tail of the distribution at slopes less than 0. This shows that the data favor a flat slope, but are also consistent with the fundamental plane slope, $m = 0.67$ (*Gültekin et al.*, 2009a).

2.5 Discussion

The goal of this study was to examine the disk-jet coupling in an accreting SMBH. We chose to probe the viscous timescale of the inner accretion disk, as jets are thought to be launched within this region (eg., *Doeleman et al.*, 2012). In SMBHs, this timescale is on the order of a few days to months, making a simultaneous X-ray and radio observing campaigns feasible. Conversely, in stellar-mass black holes, this timescale is only a few 10's of seconds.

In particular, we chose NGC 4395 because it is a bright, nearby Seyfert with the lowest known mass, making the appropriate cadence of such a campaign only a few days. We used *Swift* and the VLA to monitor both the X-ray from 2–10 keV and radio at 8.4 GHz over a two month period.

In detail, we found that the X-ray variability was dominated by neutral absorption, but both the intrinsic X-ray continuum and compact radio emission did show variability. There was no statistically significant time delay between the X-ray and radio variability. We also correlated the nearly simultaneous X-ray and radio observations using a Spearman's ranking correlation test and found a weak positive correlation, $\tau = 0.15$. Further, a linear fit to the data gave the relation $\log(L_R) = 0.06 \log(L_X) + 32.6$, but the data were also consistent with the fundamental plane of black hole activity with a slope of $m = 0.67$. See Figures 2.4(a) & 2.4(b). This is consistent with the idea that the amplitude of the X-ray variability is greater than the radio variability, and the latter is responsible for driving NGC 4395 horizontally in the L_X-L_R plane.

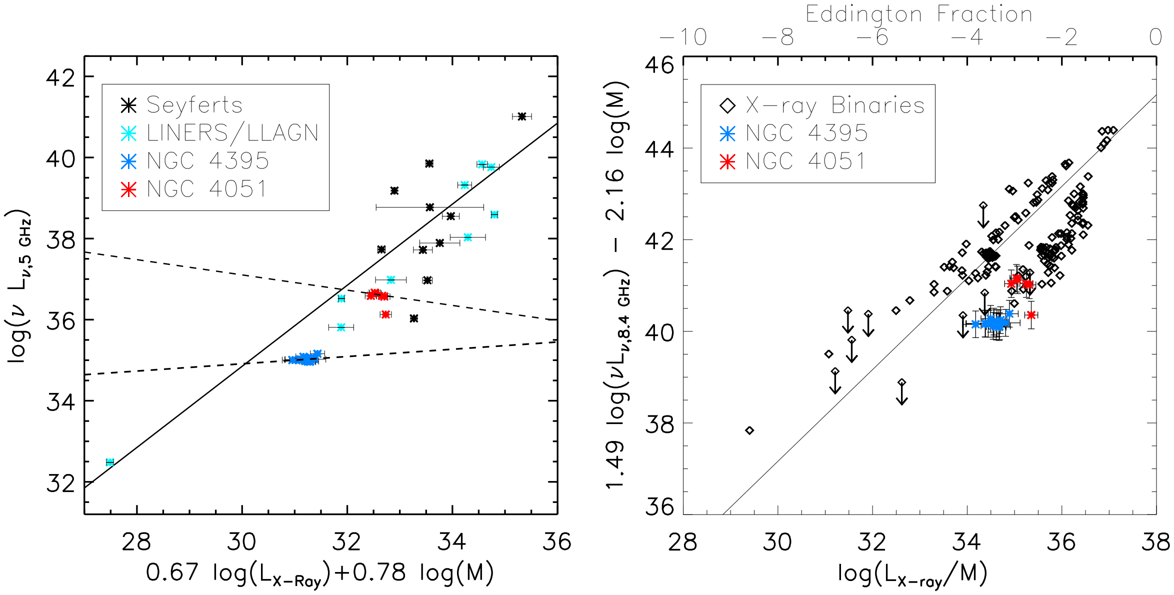

(a) (b)

Figure 2.5 a) The above plot shows both NGC 4395 and NGC 4051 as they lie on the fundamental plane of black hole activity measured by *Gültekin et al.* (2009a). The solid line in both Figure 4.8 & 2.5(b) shows the plane derived by *Gültekin et al.* (2009a), $\log(\nu L_{\nu,5GHz}) = 4.8 + 0.78 \log(M_{BH}) + 0.67 \log L_X$. The radio observations were converted to 5 GHz assuming $F_\nu \propto \nu^{-1}$. The dashed line shows the best fit lines to each of the Seyferts. In general NGC 4395 and NGC 4051 lie on the fundamental plane but move out of it when looking at simultaneous X-ray and radio observations on viscous timescales of the inner disk. b) This plot shows NGC 4395 and NGC 4051 plotted against the stellar-mass black holes as described in *Gallo et al.* (2012). The plot shows the Eddington ratio versus the radio luminosity corrected by the mass term, which is derived from the fundamental plane relation (black line, *Gültekin et al.*, 2009a). NGC 4395 and NGC 4051 appear to lie on the second, steeper track, which is suggestive that SMBH follow two distinct tracks just as stellar-mass black holes do.

NGC 4395 is not the only Seyfert that shows this general behavior. In our previous work, we show that NGC 4051 has higher variability in the X-ray as compared to its simultaneous radio observations (*King et al.*, 2011). NGC 4051 is slightly larger at $1.73^{+0.55}_{-0.52} \times 10^6 M_\odot$ (*Denney et al.*, 2010), and the simultaneous X-ray and radio observing campaign of NGC 4051 probed the same viscous times as in NGC 4395 (*King et al.*, 2011).

Shown in Figure 4.8 are both NGC 4395 and NGC 4051, as they move out of the fundamental plane as given for Seyferts by *Gültekin et al.* (2009a). Both sources are fairly constant in the radio, while the X-ray drives them out of the plane. Each of their respective best fit slopes are plotted as the dashed lines on Figure 4.8. As the two sources do lie on the plane, the X-ray variability may be partially responsible for the observed scatter of the fundamental plane.

In Figure 2.5(b), the two Seyferts are now plotted against the fundamental plane of stellar-mass black holes taken from work by *Gallo et al.* (2012). All the black holes have been corrected for mass using the fundamental plane derived from *Gültekin et al.* (2009a), and a mass of $10 M_\odot$ has been assumed for the stellar-mass black holes. As noted in *Gallo et al.* (2012), the stellar-mass black holes occupy two different tracks: 1) the typical "fundamental plane" track that scales a s $L_R \propto L_X^{0.63\pm0.03}$, and 2) a second track that is steeper that scales as $L_R \propto L_X^{0.98\pm0.08}$. NGC 4395 and NGC 4051 do lie on and may follow this steeper L_X-L_R relation. If some SMBH also follow a second, steeper L_X-L_R relation, it would imply that two distinct modes of accretion and jet production occur in both stellar-mass and SMBHs, and gives rise to a picture that the underlying physical mechanisms in disk-jet coupling scale across the black hole mass scale.

Further, the flat slope in the L_X-L_R plane traced by NGC 4395 and NGC 4051 suggests they are tracing a branch between the two tracks. This would be similar to the behavior of H1743-322, which jumps between the two tracks (*Coriat et al.*, 2011; *Gallo et al.*, 2012). However, the slope of NGC 4395 is also consistent with a steeper slope. In addition, as the amplitude of the X-ray variability is more variable than the radio variability, it is possible that strong variations in the disk or corona may get washed out when transferred to the jet on larger scales (e.g., *Maitra et al.*, 2009). In essence, the base of the jet might act as a low-pass filter for transferring only sufficiently large or sustained variations to the jet. This would imply that on short timescales and any Eddington ratio, a source would follow a flat relation and move out of the L_X-L_R relation in Figure 2.5(b). On longer timescales variations the SMBH may trace out the fundamental plane, $L_R \underset{\sim}{\propto} L_X^{0.7}$ or the steeper relation of $L_R \underset{\sim}{\propto} L_X^{1}$. This is interesting because jets are known to be launched within 10's of gravitational radii (*Doeleman et al.*, 2012), which would correspond to viscous times of the inner disk. Yet our study points to longer timescales for disk-jet couplings, indicating global effects that propagate from further out in the accretion disk are vital to the disk-jet coupling.

Additional tracks in the L_X-L_R plane have also been seen in not only stellar-mass black holes, but also in a few samples of low excitation galaxies (LEG) and Fanaroff-Riley I (FR I) galaxies (e.g., *Chiaberge et al.*, 2002; *Hardcastle et al.*, 2006; *Evans et al.*, 2006; *Hardcastle et al.*, 2009; *de Gasperin et al.*, 2011). These sources generally fall above the conical "fundamental plane", i.e. are radio bright or X-ray dim (*Hardcastle et al.*, 2009; *de Gasperin et al.*, 2011). It has been suggested that the discrepancy between these sources is due to the LEG and FR I jet-dominated X-ray emission, while sources on the fundamental plane from (e.g., *Merloni et al.*, 2003) have accretion dominated X-ray emission (*Chiaberge et al.*, 2002; *Evans et al.*, 2006; *de Gasperin et al.*, 2011). Interestingly, NGC 4395, NGC 4051 and the second stellar-mass track do the opposite and lie below the "fundamental plane", i.e. are X-ray bright and radio dim. This would argue that unlike the LEG and FR I sources whose X-ray emission is jet-dominated, that the X-ray emission is accretion-dominated like the fundamental plane sources but more efficiently radiating. This argument has also been suggested for AGN by *Wu et al.* (2013), who find low luminosity AGN form a second track as well, but in the L_B-L_R plane where L_B is the B band luminosity, another accretion disk proxy.

2.6 Conclusion

In this study, we have observed NGC 4395 for approximately two months with nearly simultaneous 8.4 GHz radio observations with the VLA and 2–10keV *Swift* X-ray observations. We find that the X-ray flux has large variability that is dominated by variable neutral absorption. When we correlate the unabsorbed continuum X-ray variability with the radio variability, we find that the data are consistent with no time delay between the two bands and that the X-ray variability dominates over the radio variability. In addition, the data are consistent with the slope of the fundamental plane but also with a flat slope in the L_X-L_R plane.

The average X-ray and radio luminosity of NGC 4395 as well as NGC 4051 are consistent with lying on the fundamental plane of black hole activity, and the X-ray variability driving some of the observed scatter. Furthermore, both Seyferts appear to lie on the “second” L_X-L_R stellar-mass black hole track discussed in *Gallo et al.* (2012). These sources may be probing a second, distinct disk-jet coupling, which is also seen in stellar-mass black holes. Our future work will be to probe higher accretion regimes in SMBHs to see if at higher Eddington ratios the SMBHs follow one of the two tracks or still move out of the plane like NGC 4395 and NGC 4051. In addition, longer timescales will be examined in order to assess global accretion affects.

Acknowledgements

We would like to thank the anonymous referee for their invaluable comments, as well as Michael Rupen for his instrumental help. A.L.K. gratefully acknowledges support through the NASA Earth and Space Sciences Fellowship. The National Radio Astronomy Observatory is a facility of the National Science Foundation operated under cooperative agreement by Associated Universities, Inc.

CHAPTER III

An Extreme X-ray Disk Wind in the Black Hole Candidate IGR J17091−3624

A. L. King[1], J. M. Miller[1], J. Raymond[2], A. C. Fabian[3], C. S. Reynolds[4], T. .R. Kallman[5], D. Maitra[1], E. M. Cackett[3,6], M. P. Rupen[7]

[1]Department of Astronomy, University of Michigan, 500 Church Street, Ann Arbor, MI 48109-1042, USA, ashking@umich.edu

[2]Smithsonian Astrophysical Observatory, 60 Garden Street, Cambridge, MA, 02138, USA

[3]Institute of Astronomy, University of Cambridge, Madingley Road, Cambridge, CB3 OHA, UK

[4]Department of Astronomy, University of Maryland, College Park, MD, 20742, USA

[5]Laboratory for High Energy Astrophysics, NASA Goddard Space Flight Center, Code 662, Greenbelt, MD 20771, USA

[6]Wayne State University, Department of Physics and Astronomy, Detroit, MI, 48201, USA

[7]National Radio Astronomy Observatory, Socorro, NM 87801, USA

3.1 Abstract

Chandra spectroscopy of transient stellar-mass black holes in outburst has clearly revealed accretion disk winds in soft, disk–dominated states, in apparent anti-correlation with relativistic jets in low/hard states. These disk winds are observed to be highly ionized, dense, and to have typical velocities of ∼1000 km/s or less projected along our line of sight. Here, we present an analysis of two *Chandra* High Energy Transmission Grating spectra of the Galactic black hole candidate IGR J17091−3624 and contemporaneous EVLA radio observations, obtained in 2011. The second *Chandra* observation reveals an absorption line at 6.91±0.01 keV; associating this line with He-like Fe XXV requires a blue-shift of 9300^{+500}_{-400} km/s ($0.03c$, or the escape velocity at 1000 R_{Schw}). This projected outflow velocity is an order of magnitude higher than has previously been observed in stellar-mass black holes, and is broadly consistent with some of the fastest winds detected in active galactic nuclei. A potential feature at 7.32 keV, if due to Fe XXVI, would imply a velocity of $\sim$ 14600 km/s ($0.05c$), but this putative feature is marginal. Photoionization modeling suggests that the accretion disk wind in IGR J17091−3624 may originate within 43,300 Schwarzschild radii of the black hole, and may be expelling more gas than accretes. The contemporaneous EVLA observations strongly indicate that jet activity was indeed quenched at the time of our *Chandra* observations. We discuss the results in the context of disk winds, jets, and basic accretion disk physics in accreting black hole systems.

3.2 Introduction

A detailed observational account of how black hole accretion disks drive winds and jets remains elusive, but the combination of high resolution X-ray spectroscopy, improved radio sensitivity, and comparisons across the black hole mass scale hold great potential. The broad range in X-ray luminosity covered by transient stellar-mass black holes makes it possible to trace major changes in the accretion flow as a function of the inferred mass accretion rate; this is largely impossible in supermassive black holes. Disk winds and jets, for instance, appear to be state-dependent and mutually exclusive in sources such as H 1743−322 (*Miller et al.*, 2006b; *Blum et al.*, 2010), GRO J1655−40 (*Miller et al.*, 2008; *Luketic et al.*, 2010; *Kallman et al.*, 2009), and GRS 1915+105 (*Miller et al.*, 2008; *Neilsen and Lee*, 2009). This may offer insights into why many Seyfert AGN, which are well known for their disk winds, are typically radio–quiet (though not necessarily devoid of jets; see *King et al.*, 2011; *Jones et al.*, 2011; *Giroletti and Panessa*, 2009).

The proximity of Galactic black hole binaries (BHB) ensures a high flux level and spectra with excellent sensitivity in the Fe K band. This is of prime importance because He-like Fe XXV and H-like Fe XXVI lines can endure in extremely hot, ionized gas (see, e.g. *Bautista and Kallman*, 2001), and therefore trace the wind region closest to where it is launched near the black hole. Studies of some stellar-mass black hole disk winds find that the gas is too ionized, too dense, and originates too close to the black hole to be expelled by radiative pressure or by thermal pressure from Compton heating of the disk, requiring magnetic pressure (*Miller et al.*, 2006b,a; *Kubota et al.*, 2007). Winds that may originate close to the black hole and carry high mass fluxes are also observed in AGN (e.g., *Kaspi et al.*, 2002; *Chartas et al.*, 2002; *King et al.*, 2012a; *Tombesi et al.*, 2010).

In this Letter, we present evidence of a particularly fast disk wind in the black hole candidate IGR J17091−3624. The current outburst of IGR J17091−3624 was first reported on 2011 January 28 (*Krimm et al.*, 2011). Our observations caught IGR J17091−3624 in the high/soft state, but it is important to note that the source has also showed low/hard state episodes with flaring and apparent jet activity in radio bands (*Rodriguez et al.*, 2011). X-ray flux variations in IGR J17091−3264 bear similarities to the microquasar GRS 1915+105 (e.g., *Altamirano et al.*, 2011a).

3.3 Observation and Data Reduction

IGR J17091−3624 was first observed with *Chandra* on 2011 August 1 (ObsID 12405), starting at 06:59:16 (UT), for a total of 30 ksec. The High Energy Transmission Gratings (HETG) were used to disperse the incident flux onto the Advanced CCD Imaging Spectrometer spectroscopic array (ACIS-S). To prevent photon pile-up, the ACIS-S array was operated in continuous clocking or "GRADED_CC" mode, which reduced the nominal frame time from 3.2 seconds to 2.85 msec. The zeroth

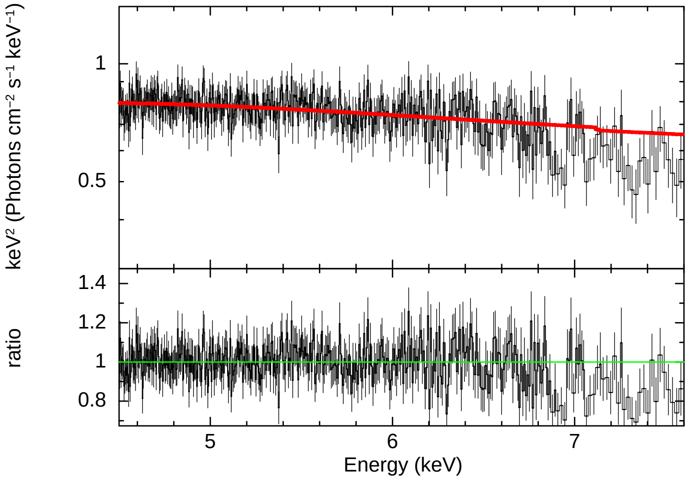

Figure 3.1 The second *Chandra*/HETG spectrum of IGR J17019−3624 is shown above, fit with a simple disk blackbody plus power-law continuum. The continuum fit excluded the Fe K band to prevent being biased by line features. The line at 6.91 keV is clearly apparent in the data/model ratio. Associating this line with He-like Fe XXV implies an outflow velocity of 9300^{+500}_{-400}km/s. Weak evidence of a line at 7.32 keV, plausibly associated with Fe XXVI, would imply an even higher outflow velocity. The data were binned for visual clarity.

order flux is incident on the S3 chip, and frames from this chip can be lost from the telemetry stream if a source is very bright. We therefore used a gray window over the zeroth order aimpoint; only one in 10 photons were telemetered within this region. For a longer discussion of this mode, please see, e.g., Miller et al. (2006) and Miller et al. (2008). The source was observed for a second time on 2011 October 6, starting at 11:17:02 (UT), again for a total of 30 ksec. The relatively low flux observed during the first observation indicated that the ACIS-S array could be operated in the standard “timed event” imaging mode during this second observation.

Data reduction was accomplished using CIAO version 4.1 (*Fruscione et al.*, 2006). Time-averaged first-order High Energy Grating (HEG) and Medium Energy Grating (MEG) spectra were extracted from the Level-2 event file. Redistribution matrix files (rmfs) were generated using the tool “mkgrmf”; ancillary response files (arfs) were generated using “mkgarf”. The first-order HEG spectra and responses were

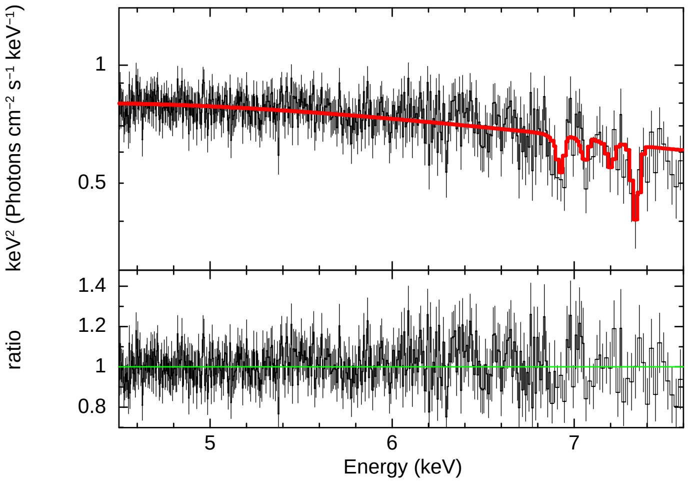

Figure 3.2 The second *Chandra*/HETG spectrum of IGR J17019−3624 is shown above, fit with a simple disk blackbody plus power-law continuum. A self-consistent photoionization model, generated using XSTAR, was used to model the absorption in the Fe K band. The data were binned for visual clarity.

combined using the tool "add_grating_orders". The spectra were then grouped to require a minimum of 10 counts per bin. All spectral analyses were conducted using XSPEC version 12.6.0. All errors quoted in this paper are 1σ errors.

Nearly simultaneous radio observations were made with the EVLA at each *Chandra* pointing. The first radio epoch included a two hour integration at 8.4 GHz on 2011 August 2 (MJD 55776) at 1:01:04 (UT), while the second was a two hour integration at both 8.4 and 4.8 GHz on 2011 October 6 (MJD 55841) at 22:10:16 (UT). The flux and bandpass calibrator was 3C 286. The phase and gain calibrators were J1720-3552 and J1717-3624, for the first and second observations, respectively. The data are reduced using CASA version 3.2.1 (*McMullin et al.*, 2007).

3.4 Analysis and Results

A black hole mass has not yet been determined for J17091−3624; a value of 10 $M_\odot$ is assumed throughout this work. Preliminary fits to the HETG spectra of IGR J17091−3624 suggested a relatively high column density, in keeping with values predicted from radio surveys (e.g. $N_{\rm H} = 7.6\times10^{21}$ cm^{-2}; *Dickey and Lockman*, 1990). Due to this high column that predominantly affects lower energies, the MEG spectra have comparatively low sensitivity as compared to the HEG, and were therefore excluded.

The limitations of the HEG and our instrumental configuration enforce an effective lower energy bound of 1.3 keV. In the second observation, the instrumental configuration served to enforce an upper limit to the fitting range of 7.6 keV. This limit was adopted for the first observation as well.

3.4.1 The Spectral Continuum

The HEG spectra were fit with a fiducial spectral model including an effective H column density (*TBabs*), a disk blackbody component, and a power-law component.

The first observation (MJD 55775) is well described by column density of N_H=9.9±0.1× 10^{21} cm^{-2}, and a disk blackbody temperature of 1.3±0.1 keV. The resulting fit gave a χ^2/ν = 2657/3156 = 0.84. This spectrum is dominated by the disk black body component, typical of the high soft state of BHB. A power-law continuum component is not statistically required. An unabsorbed flux of $F_{2-10keV}$ = 1.5±0.1 × 10^{-9} ergs cm^{-2} s^{-1} was measured.

The second observation (MJD 55841) also had a consistent flux, $F_{2-10keV}$ = 1.9 ±0.5 × 10^{-9} ergs cm^{-2} s^{-1}. Again, the column density was large, at N_H= 1.22±0.07 × 10^{22} cm^{-2}. A power-law photon index of $\Gamma = 1.7^{+0.07}_{-0.09}$ and a disk blackbody temperature of 2.3±0.3 keV were measured. This disk temperature is high but common in GRS 1915+105 (see, e.g., *Vierdayanti et al.*, 2010). The resulting χ^2/ν was 2754/3414=0.81.

3.4.2 The Line Spectra

In the second HEG spectrum, absorption features are noted in the Fe K band (See Figure 1), and these were initially fit with simple Gaussians. The two strongest lines are found at energies of 6.91±0.01 keV and $7.32^{+0.02}_{-0.06}$. Via an F-test, (see *Protassov et al.*, 2002, for some cautions), these lines are significant at the 99.94% and 99.67% confidence levels respectively. Dividing the flux normalization of each line by its minus-side error suggests that the feature at 6.91 keV is significant at the 4σ level of confidence, while the 7.32 keV line is marginal at a 2σ confidence level.

We also modeled the second observation continuum with a Comptonization model (*compTT*) instead of the disk blackbody and power-law. In general, this gave a reasonable fit at χ^2/ν =2884/3414 = 0.84. This model also showed residual absorption features at high energy, which again we modeled with Gaussian functions. Relative to this continuum, the features at 6.91 keV and 7.32 keV are detected at a higher level of significance (6σ).

It is reasonable to associate the line at 6.91 ± 0.01 keV with He-like Fe XXV, which has a rest energy of 6.70 keV (*Verner et al.*, 1996). This translates into a blue-shift of 9300^{+500}_{-400} km/s. This feature clearly signals an extreme disk wind in IGR J17091−3624. Typical velocities in X-ray Binaries are < 1000 km/s (*Miller et al.*, 2006b,a). If the feature at $7.32^{+0.02}_{-0.06}$ keV is real and can be associated with H-like Fe XXVI at 6.97 keV, it would correspond to a blue-shift of 14600^{+2500}_{-800}. For additional details, see Table 3.1. Although less likely, the 6.91 keV line could also be associated with a redshift from the H-like Fe XXVI line. The corresponding inflowing velocity would be 2600±400 km/s. If this is due to gravitational redshift, the corresponding radius would be $1.7^{+0.3}_{-0.2} \times 10^8$ cm (60±10 R_{Schw}).

The absence of emission lines in the second spectrum of IGR J17091−3624 is notable, but is only suggestive of an equatorial wind. Given that disk winds have only been detected in sources viewed at high inclination angles, and given the similarities between IGR J17091−3624 and GRS 1915+105, it is likely that IGR J17091−3624 is also viewed at a high inclination. However, there is no evidence of eclipses in this source, so inclinations above 70° can be ruled out.

Absorption lines like those detected in the second observation of IGR J17091−3624 are absent in the first observation. Fits to the Fe K band using a local continuum model, and narrow Gaussian functions with FWHM values corresponding to those measured in the second observation give 1σ confidence limits of 3 eV or less on lines in the 6.70–7.32 keV band. This is significantly below the equivalent widths measured in the second observation. (see Table 1) This may simply be due to a variable absorption geometry in IGR J17091−3624; this has previously been observed in H 1743−322 and GRS 1915+105 (*Miller et al.*, 2006b,a, 2008; *Neilsen and Lee*, 2009).

3.4.3 Photoionization Modeling

To get a better physical picture of the absorption in the second observation of IGR 17091−3624, we also fit the data with a grid of self-consistent photoionization models created with XSTAR (*Kallman and Bautista*, 2001). The ionizing luminosity for this model was derived from extrapolating the unabsorbed spectrum from the second observation to 0.0136–30 keV, ensuring coverage above 8.8 keV, which is required to ionize Fe XXV. A distance of 8.5 kpc is first assumed to derive this luminosity ($L_{ion}=3.5\times10^{37}$ ergs/s), owing to the location of J17091−3624 within the Galactic bulge. However, *Altamirano et al.* (2011b) also suggest the possibility that this source could be accreting at high Eddington fractions but further away, and a distance of 25 kpc was also adopted in a second XSTAR grid ($L_{ion}=3.5\times10^{38}$ ergs/s).

The density of the absorbing material was chosen to be $\log(n) = 12.0$. This is a reasonable assumption based on the modeling of similar X-ray binaries: GX 13+1, $n = 10^{13}$ cm^{-3}(*Ueda et al.*, 2004), GRO J1655-40, $n = 10^{14}$ cm^{-3}(*Miller et al.*, 2008), H1743-322, $n = 10^{12}$ cm^{-3} (*Miller et al.*, 2006b). A turbulent velocity of 1000 km/s was found to provide the best fit after various trials. A covering factor of 0.5 was chosen as the absence of emission lines suggests an equatorial wind. Finally, the Fe abundance was assumed to be twice the solar value after initial fits; this characterizes the Fe K lines but does not predict absorption lines, e.g. Si, that are not observed.

The initial, lower luminosity grid was fit to the data in XSPEC as a multiplicative model; free parameters included the column density, ionization, and velocity shifts of the absorbing gas (see Table 3.1 and Figure 2). For the disk blackbody and power-law continuum, an ionization parameter of $\log \xi = 3.3^{+0.2}_{-0.1}$ is required, as well as a wind column density of $\mathrm{N} = 4.7^{+1.7}_{-1.9} \times 10^{21}$ cm^{-2}. Velocity shifts consistent with simple Gaussian models are found using the XSTAR grid.

To fit the putative higher energy absorption, a second outflow component is required. An additional, lower luminosity XSTAR component is significant at the 3σ level, relative to both continua. The wind column density was higher at $\mathrm{N} = 1.7^{+1.2}_{-0.8} \times 10^{22}$ cm^{-2}, and the $\log \xi = 3.9^{+0.5}_{-0.3}$. This system is moving even faster at 15400±400 km/s = 0.05c. (See Table 3.1 and Figure 2)

Repeating this analysis, but utilizing the higher luminosity XSTAR grid, we find that the two components are again required. In fact, the values of the column density, ionization and velocity shifts are nearly identical and well within 1σ of the previous model.

To derive one estimate to the radius where these winds are launched, we can estimate the radius at which the observed velocity equals the escape velocity. This constrains the radius to be at $r \simeq 2.9 \times 10^9$ cm (970 R_{Schw}). Using $\xi = L/(nr^2)$ and N= nrf, where f is the 1-dimensional filling factor, we can then derive the filling factor and density of the region. Assuming the ionizing luminosity is 3.5×10^{37} erg/s, the resulting filling factor is $f \simeq 0.0008$, and the density is $n \simeq 2 \times 10^{15}$ cm^{-3}. However, if the luminosity is higher (L_{ion}=3.5×10^{38} erg/s), the filling factor decreases to $f \simeq 8 \times 10^{-5}$, and the density increases to $n \simeq 2 \times 10^{16}$ cm^{-3}.

These density estimates are quite high when compared to other X-ray binaries (e.g., *Ueda et al.*, 2004; *Miller et al.*, 2006b, 2008). However, we can invert the previous argument and instead derive the filling factor and radius from an assumed density, i.e. $n = 10^{12}\mathrm{cm}^{-3}$. We find a larger filling factor, ($f \simeq 0.04$), and radius, ($r \simeq 1.3 \times 10^{11}$ cm, 43,300 R_{Schw}), if we require a luminosity of 3.5×10^{37} erg/s. A larger luminosity, i.e. L_{ion}=3.5×10^{38} erg/s, reduces the filling factor, ($f \simeq 0.01$) but increases the radius ($r \simeq 3 \times 10^{11}$ cm, 100,000 R_{Schw}). At these radii the escape velocity is much lower than the observed velocity.

Finally, we can estimate the mass outflow rate ($\dot{m}_{wind}$) using a modified spherical outflow, which can be approximated as $\dot{m}_{wind} \simeq 1.23 m_p L_{ion} f v \Omega/\xi$. Here, we assume a covering factor $\Omega/4\pi = 0.5$, and an outflowing velocity of $v = 9,600$ km/s. A luminosity of $L_{ion} = 3.5 \times 10^{38}$ erg/s and filling factor of $f = 8 \times 10^{-5}$, gives a lower limit of $\dot{m}_{wind} \simeq 3.5 \times 10^{16}$ $(10^4/\xi)$ g/s. However, a much larger outflow rate of $\dot{m}_{wind} \simeq 1.7 \times 10^{18}$ $(10^4/\xi)$ g/s is found, if we assume $L_{ion} = 3.5 \times 10^{37}$ erg/s and filling factor of $f = 0.04$

For comparison, $L = \eta \dot{m}_{acc} c^2$, where η is an efficiency factor typically taken to be 10%. For IGR J17091−3624, $\dot{m}_{acc} = 3.8 \times 10^{17}$ g/s. Using $\log \xi = 3.3$ from the disk blackbody and power-law model, we find that the observed portion of the outflow is likely to carry away 0.4–20 times the amount of accreted gas. Unless a geometrical consideration serves to bias our estimates, a high fraction of the available gas may not accrete onto the black hole. This trend is not only seen in BHB but in Seyferts as well. *Blustin et al.* (2005) note that more than half of their observed Seyferts show $\dot{M}_{out}/\dot{M}_{acc} > 0.3$.

3.4.4 Radio Non-Detections

The EVLA radio observations at 8.4 GHz were made nearly contemporaneously with their X-ray counterparts. Both radio observations were nearly two hours in duration. Neither observation detected a source at the location of IGR J17091−3624. The RMS noise level for each observation was 0.02 mJy and 0.07 mJy for the two epochs, respectively. The second observation had extended coverage to 4.8 GHz that also had a non-detection. The RMS for this frequency was 0.13 mJy. In contrast, IGR J17091−3624 was detected at the 1–2 mJy level during the low/hard state (*Rodriguez et al.*, 2011). This supports prior findings that the radio jet is absent during the periods when winds are seen in BHB (*Miller et al.*, 2006b, 2008; *Neilsen and Lee*, 2010).

3.5 Discussion and Conclusions

At ionizations above 10^3, radiation pressure is inefficient, and it is not able to drive these winds (e.g., *Proga*, 2000). Thus, although the UV components of disk winds in AGN are driven at least partially by radiation pressure, the wind in IGR J17091−3624 likely cannot be driven in this way. A thermal wind can arise at radii greater than 0.2 R_C (*Woods et al.*, 1996), where $R_C = (1.0 \times 10^{10}) \times (M_{BH}/M_{\odot})/T_{C8}$, where T_{C8} is the Compton temperature of the gas in units of 10^8 K. The spectrum observed in the second observation gives $R_C \simeq 5 \times 10^{12}$ cm. Therefore, if we assume our conservative estimate of the launching radius, it is possible for IGRJ17091−3624 to have a thermally driven wind. However, if the wind originates closer to the black hole, then it is likely that magnetic processes – either pressure from magnetic viscosity within the disk (e.g., *Proga*, 2003) or magneto-centrifugal acceleration (e.g., *Blandford and Payne*, 1982) – must play a role in launching the wind observed in IGR J17091−3624.

Fast X-ray disk winds are not only seen in BHB like IGR J17091−3624, but also in AGN and quasars (e.g., *King et al.*, 2012a; *Chartas et al.*, 2002). The fastest UV winds observed in AGN are pushed to high velocities by radiation pressure. It remains to be seen whether a common driving mechanism works across the black hole mass scale to drive fast, highly ionized X-ray disk winds. *Chartas et al.* (2002) show that in the quasar APM 08279+5255 there are broad absorption features, which are likely highly relativistic Fe XXV and/or Fe XXVI lines. In these regards, it bears some similarities to the most extreme winds in BHB's.

Observations of BHB point to an anti-correlation of wind and jet outflows from accretion disks (*Miller et al.*, 2006b, 2008; *Blum et al.*, 2010; *Neilsen and Lee*, 2010). Winds appear to only be detected, or at least are considerably stronger, in soft, disk–dominated states, and absent in hard states where compact, steady jets are ubiquitous (*Fender et al.*, 2006). In H 1743−322, in particular, there is evidence that the absence of winds in hard states is *not* an artifact of high ionization hindering the detection of absorption lines, but instead represents a real change in the column density (and thus the mass outflow rate) in any wind (*Blum et al.*, 2010).

It appears that our coordinated *Chandra* and EVLA observations of IGR J17091−3624 support this anti-correlation. The EVLA observations place very tight limits on the radio flux when the disk wind is detected, orders of magnitude below the level at which IGR J17091−3624 was detected in radio during its low/hard state only a few months prior (*Rodriguez et al.*, 2011).

Neilsen and Lee (2009) suggested that the production of winds may be responsible for quenching jets in GRS 1915+105. It might then be the case that jets should be observed whenever winds are absent. In our first observation of IGR J17091−3624, however, neither a wind nor a jet is detected, with tight limits. Instead, the apparent dichotomy between winds and jets may signal the magnetic field topology in and above the disk is state-dependent. This is broadly consistent with multi-wavelength studies suggesting synchrotron flares above the disk, but only in the hard state (e.g. GX 339−4, XTE J1118+480, *Di Matteo et al.*, 1999; *Gandhi et al.*, 2010). It is interesting to speculate that the magnetic field might be primarily toroidal in the soft state, where a Shakura-Sunyaev disk is dominant, but primarily poloidal in the hard state, when the mass accretion rate is lower (e.g., *Beckwith et al.*, 2008). The type of outflow that is observed may also depend greatly on how much mass is loaded onto magnetic field lines; that could depend on variables including the mass accretion rate through the disk.

Acknowledgements

We would like to thank the anonymous referee. We thank Michael Nowak for his instrumental help as well. ALK gratefully acknowledges support through the NASA Earth and Space Sciences Fellowship. JMM gratefully acknowledges support through the *Chandra* Guest Observer program. The National Radio Astronomy Observatory is a facility of the National Science Foundation operated under cooperative agreement by Associated Universities, Inc.

Table 3.1. Spectral Modeling Parameters of the 2^{nd} HEG observation

Parameter	Model 1	Model 2	Model 3	Model 4
	diskbb + po + Gauss + Gauss	(diskbb + po) × Xstar × Xstar	comptt + Gauss + Gauss	(comptt) × Xstar × Xstar
N_H (10^{22} cm^{-2})	1.14 ± 0.06	1.13 ± 0.06	$0.475^{+0.017}_{-0.018}$	$0.558^{+0.025}_{-0.028}$
-				
T_{in} (keV)	1.53 ± 0.09	$1.51^{+0.11}_{-0.09}$	-	-
Norm	$13.1^{+3.6}_{-2.5}$	$13.8^{+4.0}_{-1.7}$	-	-
Γ	$1.93^{+0.15}_{-0.16}$	1.91 ± 0.17	-	-
Norm	$0.35^{+0.07}_{-0.08}$	0.34 ± 0.08	-	-
-				
T_0 (keV)	-	-	0.58 ± 0.01	0.59 ± 0.01
kT (keV)	-	-	$10.5^{+30}_{-1.7}$	9.8 ± 0.02
τ_{plasma}	-	-	2.24 ± 0.01	2.28 ± 0.01
Norm	-	-	0.0584 ± 0.0001	$0.062^{+0.002}_{-0.05}$
-				
E_{FeXXV} (keV)	6.91 ± 0.01	-	$6.91^{+0.02}_{-0.01}$	-
FWHM (keV)	$0.091^{+0.022}_{-0.049}$	-	$0.13^{+0.19}_{-0.04}$	-
EW (keV)	$0.021^{+0.005}_{-0.002}$	-	$0.040^{+0.007}_{-0.009}$	-
Norm (10^{-4})	$3.5^{+0.8}_{-0.6}$	-	$6.0^{+1.1}_{-1.3}$	-
v (km/s)	9300^{+500}_{-400}	-	9300^{+400}_{-800}	-
-				
E_{FeXXVI} (keV)	$7.32^{+0.02}_{-0.06}$	-	7.30 ± 0.02	-
FWHM (keV)	$0.081^{+0.079}_{-0.027}$	-	$0.25^{+0.13}_{-0.01}$	-
EW (keV)	$0.032^{+0.018}_{-0.004}$	-	$0.089^{+0.013}_{-0.014}$	-
Norm (10^{-4})	$3.4^{+1.9}_{-0.4}$	-	$11.8^{+1.7}_{-1.6}$	-
v (km/s)	14600^{+2500}_{-800}	-	13800 ± 800	-
-				
N (10^{22} cm^{-2})	-	$0.47^{+0.17}_{-0.19}$	-	$0.45^{+0.33}_{-0.17}$
$\log\xi$(ergs cm s^{-1})	-	$3.3^{+0.2}_{-0.1}$	-	$3.4^{+0.2}_{-0.1}$
v (km/s)	-	9600^{+400}_{-500}	-	9600 ± 300
-				
N (10^{22} cm^{-2})	-	$1.66^{+1.18}_{-0.83}$	-	$1.97^{+1.26}_{-0.51}$
$\log\xi$(ergs cm s^{-1})	-	$3.9^{+0.5}_{-0.3}$	-	$3.7^{+0.3}_{-0.1}$
v (km/s)	-	15400 ± 400	-	15400^{+400}_{-300}
-				

Table 3.1 (cont'd)

Parameter	Model 1 diskbb + po + Gauss + Gauss	Model 2 (diskbb + po) × Xstar × Xstar	Model 3 comptt + Gauss + Gauss	Model 4 (comptt) × Xstar × Xstar
χ^2/ν	$2725/3408 = 0.80$	$2731/3408 = 0.80$	$2793/3408 = 0.82$	$2761/3408 = 0.81$

Note. — This Table lists the line detections using Gaussian functions as well as more self-consistent, photoionization components created with XSTAR, assuming two different continuum models. *TBabs* is applied to all the models and the errors are 1σ confidence level.

CHAPTER IV

Regulation of Black Hole Winds and Jets across the Mass Scale

A. L. King[1], J. M. Miller[1], J. Raymond[2], A. C. Fabian[3], C. S. Reynolds[4], K. Gültekin[1], E. M. Cackett[3,5], S. W. Allen[6,7], D. Proga[8,9], T. R. Kallman[10]

[1]Department of Astronomy, University of Michigan, 500 Church Street, Ann Arbor, MI 48109-1042, ashking@umich.edu

[2] Smithsonian Astrophysical Observatory, 60 Garden Street, Cambridge, MA 02138, USA

[3]Institute of Astronomy, University of Cambridge, Madingley Road, Cambridge, CB3 OHA, UK

[4]Department of Astronomy, University of Maryland, College Park, MD 20742, USA

[5]Wayne State University, Department of Physics and Astronomy, Detroit, MI 481201, USA

[6]Kavli Institute for Particle Astrophysiccs and Cosmology, Department of Physics, Stanford University, 452 Lomita Mall, Stanford, CA 94305, USA

[7]SLAC National Accelerator LAboratory, 2575 Sand Hill Road, Menlo Park, CA 94025, USA

[8]Department of Physics, University of Nevada, Las Vegas, NV 89154, USA

[9]Princeton University Observatory, Peyton Hall, Princeton, NJ 08544, USA

[10]Laboratory for High Energy Astrophysics, NASA Goddard Space Flight Center, Code 662, Greenbelt, MD 20771, USA

4.1 Abstract

We present a study of the mechanical power generated by both winds and jets across the black hole mass scale. We begin with the study of ionized X-ray winds and present a uniform analysis using *Chandra* grating spectra. The high quality

grating spectra facilitate the characterization of the outflow velocity, ionization and column density of the absorbing gas. We find that the kinetic power of the winds, derived from these observed quantities, scales with increasing bolometric luminosity as $\log(L_{\rm wind,42}/C_v) = (1.58 \pm 0.07)\log(L_{\rm Bol,42}) - (3.19 \pm 0.19)$. This suggests that supermassive black holes may be more efficient than stellar-mass black holes in launching winds, per unit filling factor, C_v. If the BHB and AGN samples are fit individually, the slopes flatten to $\alpha^{BHB} = 0.91 \pm 0.31$ and $\alpha^{AGN} = 0.63 \pm 0.30$ (formally consistent within errors). The broad fit and individual fits both characterize the data fairly well, and the possibility of common slopes may point to common driving mechanisms across the mass scale. For comparison, we examine jet production, estimating jet power based on the energy required to inflate local bubbles. The jet relation is $\log(L_{\rm Jet,42}) = (1.18 \pm 0.24)\log(L_{\rm Bondi,42}) - (0.96 \pm 0.43)$. The energetics of the bubble associated with Cygnus X-1 are particularly difficult to determine, and the bubble could be a background supernova remnant. If we exclude Cygnus X-1 from our fits, then the jets follow a relation consistent with the winds, but with a higher intercept, $\log(L_{\rm Jet,42}) = (1.34 \pm 0.50)\log(L_{\rm Bondi,42}) - (0.80 \pm 0.82)$. The formal consistency in the wind and jet scaling relations, when assuming $\mathrm{L_{Bol}}$ and $\mathrm{L_{Bondi}}$ are both proxies for mass accretion rate, suggests that a common launching mechanism may drive both flows; magnetic processes, such as magneto-hydrodynamics and magnetocentrifugal forces, are viable possibilities. We also examine winds that are moving at especially high velocities, $v > 0.01c$. These ultra-fast outflows tend to resemble the jets more than the winds in terms of outflow power, indicating we may be observing a regime in which winds become jets. A transition at approximately $L_{\rm Bol} \approx 10^{-2} L_{\rm Edd}$ is apparent when outflow power is plotted versus Eddington fraction. At low Eddington fractions, the jet power is dominant, and at high Eddington fractions, the wind power is dominant. This study allows for the total power from black hole accretion, both mechanical and radiative, to be characterized in a simple manner and suggests possible connections between winds and jets. X-ray wind data and jet cavity data will enable stronger tests.

4.2 Introduction

Both winds and jets are thought to be driven by accretion disks; jets may be launched from the innermost regions, while winds may originate further out in the accretion disk (e.g., *Blandford and Payne*, 1982; *Proga*, 2003). It remains to be seen just how winds and jets relate. Are winds and jets driven by similar mechanisms? Does one quench the other? What role does the geometry of the magnetic field lines play? One might expect the same physical launching mechanisms across the mass scale. Jet production is predominantly ascribed to magneto-hydrodynamics (MHD) across all mass scales; whether it is purely through MHD in the disk (e.g., *Lovelace*, 1976; *Blandford and Payne*, 1982), or through the disk and black hole (e.g., *Blandford and Znajek*, 1977; *Krolik and Hawley*, 2010). However, it has yet to be shown how wind properties scale with mass. Does radiation driving, thermal driving or magnetic processes drive these winds?

"Warm-absorbing" winds detected as X-ray absorption features are seen in up to 50% of Active Galactic Nuclei (AGN) (*Reynolds*, 1997; *George et al.*, 1998) and in the soft spectral state in stellar-mass black holes (*Miller et al.*, 2006a,b, 2008; *Ueda et al.*, 2009; *Neilsen and Lee*, 2009; *King et al.*, 2012b; *Ponti et al.*, 2012). These blue-shifted absorption features are highly ionized and can potentially probe regions close to the black hole and basic disk physics.

The winds observed in both black hole binaries (BHB) and supermassive black holes (SMBH) are capable of removing enormous amounts of material, even exceeding the mass accretion rates (e.g., *Blustin et al.*, 2005; *King et al.*, 2012b). They are typically wide angle outflows moving at a few hundreds of km s^{-1}. Jets, on the other hand, are highly collimated and have a much higher outflowing velocity, i.e.

near the speed of light. Consequently, the mechanical energy in these jets can be much higher than in winds. In addition, using only the radiative luminosity in jets severely underestimates the power released in these systems because a majority of the energy is mechanical (e.g., *Gallo et al.*, 2005; *Churazov et al.*, 2005; *Allen et al.*, 2006; *Merloni and Heinz*, 2007). More importantly, strong mechanical feedback from a black hole can have a significant impact on its surroundings, including galactic formation, structure and co-evolution (e.g., *Haehnelt and Kauffmann*, 2000; *Churazov et al.*, 2002; *Croton et al.*, 2006; *Ostriker et al.*, 2010; *Gaspari et al.*, 2011; *Fabian*, 2012).

On the low end of the black hole mass scale, the driving mechanisms of BHB X-ray winds are generally ascribed to either thermal pressure or magnetic mechanisms (*Begelman et al.*, 1983; *Woods et al.*, 1996; *Proga*, 2003). Absorption features of highly ionized Fe XXV and Fe XXVI are the most commonly detected, implying the ionization parameters of the gas in BHB are very high, i.e. $\log\xi > 3$ (*Miller et al.*, 2006b; *King et al.*, 2012b; *Ponti et al.*, 2012). At such high ionization states, line driving from the radiation field is inefficient at accelerating the winds to high velocities (e.g., *Proga and Kallman*, 2002). On the high mass end, X-ray winds from SMBH systems span a larger range in ionization ($0 < \log\xi < 5$). Therefore, not only are Compton heating and magnetic mechanisms plausible driving mechanisms, but radiation pressure at low ionizations is also a plausible driving mechanism (*Proga et al.*, 2000).

In this paper, we begin to examine the mechanical outflow power released in both winds and jets. In addition, we examine the outflow power across the mass scale, including stellar-mass and supermassive black holes. This will permit a complete characterization of the output of black holes: both radiative and mechanical. Characterization of the mechanical power can be particularly important on larger scales with respect to AGN feedback. AGN outflows, both jets and winds, may be responsible for shaping their environment, whether providing a source of hot ionized gas or by influencing the stellar velocity dispersion as evidenced by the $M-\sigma$ relation (e.g., *Gültekin et al.*, 2009b). These outflows may also play a vital role in the growth of black holes (e.g., *Hopkins et al.*, 2005; *Loeb*, 2005).

We describe how we derive the samples in Section 4.3. Then, we estimate the kinetic power generated by winds and jets in these systems in Section 4.4. Next, in Section 4.5, we describe the results for both the wind and jet relations, while in Section 4.6 we present the conclusions as well as context for this study. We assumed $H_0 = 70$ km s^{-1} Mpc^{-1}, $\Omega_\Lambda = 0.7$, $\Omega_M = 0.3$ throughout this work. All errors are 1σ statistical uncertainties unless otherwise stated.

4.3 The Mechanical Outflow Sample

4.3.1 X-ray Winds

The central goal in assembling this wind sample is to create a uniform, unbiased and cohesive set of standards to ensure high quality spectra and rigorous results. These requirements are: (1) blue-shifted X-ray absorption features, (2) *Chandra* grating spectra, (3) photoionization modeling, (4) at least a 3σ significant detection, and (5) velocity outflows of less than 3,000 km s^{-1}.

Wind and jet launching mechanisms are of prime interest in this analysis, so it is important to probe the wind regions that are likely to be closest to the base of the flow, and closest to the black hole. This points to a comparison of X-ray winds across the mass scale. Pragmatic considerations also make this the only consistent comparison that can be drawn. In AGN, UV radiation pressure may help to accelerate winds (but radiation pressure may not be sufficient to lift gas off of the disk in the first place); however, UV winds are not observed in BHB's, likely owing to the high ionization parameters found in these winds ($3 \leq \log\xi \leq 5$). Fortuitously, restricting our analysis to X-ray winds in AGN captures the bulk of the mass outflow rate. Prior treatments of "warm absorbers" in AGN have found that the mass outflow rate scales with the ionization parameter estimated in different components (e.g., *Blustin et al.*, 2005; *Crenshaw and Kraemer*, 2012). We also require that observations of the X-ray winds be made with the gratings spectrometers aboard *Chandra.* Although the XMM-Newton reflection grating spectrometer (RGS) is similar in many respects, it covers a narrower energy range, and it has a lower spectral resolution. The higher resolution of the Chandra gratings means that it is more sensitive to lines that are intrinsically narrow and weak, because more line flux is concentrated in fewer spectral bins. Thus, this selection criterion serves the aim of not biasing our result against weak or slow X-ray winds. Similarly, we do not consider CCD spectra of X-ray winds in our initial analysis since the modest resolution of such data inhibits the detection of weak lines and modest velocity shifts.

In addition, we require that the winds be observed as blue-shifted absorption features with respect to the host. A significance of at least 3σ for each component after fiducial fits with a canonical Galactic absorption and a power-law is also required. Further, to quantify these particular features, we demand that self-consistent photoionization modeling be performed to determine the gas parameters: the outflowing velocity, $v_{\rm out}$, and the ionization parameter, ξ. The ionization parameter is defined as $\xi = L_{ion}(nr^2)^{-1}$, where L_{ion} is the ionizing luminosity, n is the density, and r is the distance from the warm absorber to the ionizing source. There are also references in the literature to the ionization parameter U, which is defined as $U = Q(4\pi nr^2c)^{-1}$, where Q is the number of ionizing photons and c is the speed of light. We use $nr^2 = Q(4\pi Uc)^{-1} = L_{ion}\xi^{-1}$ to convert to the ionization parameter ξ. It should be noted that ξ depends on the X-ray continuum which is well constrained by observations, where as U depends on the number of ionizing photons, which is very model dependent. The physical characterization of ionization in the spectra relies on multiple lines to determine the column density, ionization state and velocity shifts of the wind components. We include fits published in the literature. A majority of those fits were obtained with XSTAR grids (*Bautista and Kallman*, 2001), which mainly use ξ to characterize the ionization of the gas. However, some fits were also obtained with CLOUDY grids (*Ferland et al.*, 1998), which mainly use U to characterize the ionization of the gas.

Finally, we restrict the outflowing velocity to be less than 3,000 km s^{-1} ($0.01c$). We reserve outflows with a velocity faster than this for a sub-sample of tentative ultra-fast outflows. As these fast winds approach such velocities they may resemble jets more so than the typical lower velocity outflows.

As a result of these criteria, we select thirteen AGN and ten BHB observations. Table 4.1 lists the ionization, velocity and kinetic power for each observed outflowing component that is used in this work. Table 4.2 reports the total kinetic luminosity from each observation, summing over all the outflowing components. Figure 4.1 plots the observed velocity shift as compared to the ionization parameter, and Figure 4.2 plots each individual absorption component's kinetic luminosity per filling factor, C_v, versus bolometric luminosity. We note here that our sample may suffer from a few selection biases. The first being that we may be biasing ourselves to high luminosity sources for which we get the best signal to noise. However, our sample does not necessarily include just the brightest sources, but also sources that are relatively faint and have long exposures in order to increase their signal to noise. (See the following sections for details of particular observations.) Therefore, a luminosity bias should not play a major role in our data. In addition, as will be shown in Section 4.4, the kinetic wind luminosity does not directly depend on the column density, i.e. signal to noise, but instead on the velocity and ionization of the gas. Therefore, as long as a significant detection is made, the depth of the absorption features will not serve to bias our samples. Another bias could be the exclusion of *XMM-Newton* data because

Table 4.1. Individual X-ray Wind Components

Object	Type	C	$\log \xi$ ergs cm s^{-1}	Velocity (km s^{-1})	L_{wind}/C_v (ergs s^{-1})	Reference
SMBH						
Akn 564	S1	1	0.40 ± 0.25	140 ± 62	42.52 ± 0.63	*McKernan et al.* (2007)
		2	2.60 ± 0.20	140 ± 62	40.32 ± 0.62	
IC 4329a	S1	1	0.20 ± 0.10	100 ± 65	42.14 ± 0.85	*McKernan et al.* (2007)
		2	2.20 ± 0.10	100 ± 47	40.14 ± 0.63	
IRAS 18325	S2	1	1.58 ± 0.09	340 ± 110	41.82 ± 0.43	*Zhang et al.* (2011a)
		2	2.35 ± 0.25	460 ± 220	41.45 ± 0.67	
MCG -6-30-15	S1	1	3.70 ± 0.20	1555 ± 105	40.89 ± 0.22	*McKernan et al.* (2007)
Mrk 290	S1	1	1.62 ± 0.15	540 ± 150	42.53 ± 0.39	*Zhang et al.* (2011b)
		2	2.42 ± 0.04	450 ± 30	41.50 ± 0.11	
Mrk 509	S1	1	2.26 ± 0.07	196 ± 80	41.93 ± 0.54	*Ebrero et al.* (2011)
NGC 3516	S1	1	2.40 ± 0.15	950 ± 147	41.55 ± 0.26	*McKernan et al.* (2007)
NGC 3783	S1	1	2.90 ± 0.10	505 ± 15	41.02 ± 0.12	*McKernan et al.* (2007)
		2	2.10 ± 0.10	515 ± 15	41.85 ± 0.12	
		3	0.40 ± 0.10	545 ± 25	43.62 ± 0.12	
		4	3.00 ± 0.10	1145 ± 42	41.99 ± 0.12	
NGC 4051	S1	1	1.00 ± 0.30	520 ± 82	41.26 ± 0.37	*McKernan et al.* (2007)
		2	2.60 ± 0.25	600 ± 77	39.85 ± 0.30	
		3	3.80 ± 0.10	2230 ± 55	40.36 ± 0.11	
NGC 4051	S1	1	4.50 ± 0.90	680 ± 40	37.81 ± 0.91	*King et al.* (2012b)
		2	3.28 ± 0.04	640 ± 45	38.95 ± 0.11	
		3	1.00 ± 0.11	400 ± 325	40.62 ± 1.06	
NGC 4151	S1	1	3.58 ± 0.30	491 ± 8	40.30 ± 0.30	*Kraemer et al.* (2005)
		2	2.26 ± 0.30	491 ± 8	41.62 ± 0.30	
NGC 4593	S1	1	2.61 ± 0.90	400 ± 121	40.47 ± 0.98	*McKernan et al.* (2007)
		2	0.50 ± 0.30	380 ± 137	42.51 ± 0.56	
NGC 5548	S1	1	2.20 ± 0.20	560 ± 77	41.77 ± 0.27	*McKernan et al.* (2007)
		2	3.90 ± 0.15	830 ± 172	40.59 ± 0.31	
BHB						
4U 1630		1	4.90 ± 0.40	300 ± 200	32.68 ± 0.96	this paper
GRO 1655−40		1	4.90 ± 0.20	500 ± 200	32.31 ± 0.56	*Miller et al.* (2008)
GRO 1655−40		1	4.20 ± 0.15	470 ± 230	33.42 ± 0.66	*Neilsen and Homan* (2012)
H 1743−322 a		1	5.50 ± 0.10	670 ± 170	33.43 ± 0.35	this paper

of its poorer resolution. However, as noted previously, the lower resolution of the RGS would serve to bias the sample against weak features. Further caveats are discussed in Section 4.6.3.

Table 4.1 (cont'd)

Object	Type	C	$\log \xi$ ergs cm s^{-1}	Velocity (km s^{-1})	$L_{\rm wind}/C_v$ (ergs s^{-1})	Reference
H 1743−322 b		1	5.60 ± 0.10	340 ± 170	32.32 ± 0.66	this paper
GRS 1915+105 s1		1	4.30 ± 0.20	300 ± 200	33.42 ± 0.89	*Ueda et al.* (2009)
GRS 1915+105 s2		1	5.60 ± 0.20	1000 ± 200	34.09 ± 0.33	*Miller et al.* (2006b)
GRS 1915+105 s3		1	5.50 ± 0.50	1400 ± 300	34.35 ± 0.57	this paper
GRS 1915+105 s4		1	6.00 ± 0.40	1100 ± 400	33.68 ± 0.62	this paper
GRS 1915+105 s5		1	6.20 ± 0.70	900 ± 400	33.22 ± 0.91	this paper

Note. — The above table lists all the components that are considered in this analysis. S1 stands for Seyfert 1 and S2 stands for Seyfert 2. C is the component number. The kinetic luminosity from the AGN that have more than one component for a single observation are summed and included as total kinetic luminosities in Table 4.2

Table 4.2. X-ray Wind and Jet Quantities

		Object	$\log L_{\rm Bol}$ (ergs s^{-1})	$\log L_{\rm wind}/C_v$ (ergs s^{-1})	$\log M_{BH}$ ($M_\odot$)	$\log D$ (cm)	Code	Reference
X-ray winds								
AGN	1	Akn 564*	44.50 ± 0.13	42.52 ± 0.63	6.9^e	26.51	X	*McKernan et al.* (2007)
	2	IC 4329a*	43.80 ± 0.13	42.15 ± 0.85	7.0^c	26.32	X	*McKernan et al.* (2007)
	3	IRAS 18325*	44.60 ± 0.13	41.98 ± 0.36	7.0^b	26.42	X	*Zhang et al.* (2011a)
	4	NGC 3516	43.50 ± 0.13	41.55 ± 0.26	7.5^a	26.07	X	*McKernan et al.* (2007)
	5	NGC 3783	44.20 ± 0.13	43.64 ± 0.12	7.5^c	26.11	X	*McKernan et al.* (2007)
	6	NGC 4051	42.60 ± 0.13	41.32 ± 0.32	6.2^a	25.50	X	*McKernan et al.* (2007)
	7	NGC 4051	42.60 ± 0.13	40.63 ± 1.04	6.2^a	25.50	X	*King et al.* (2012a)
	8	NGC 4151*	43.90 ± 0.13	41.64 ± 0.29	7.1^c	25.64	X	*Kraemer et al.* (2005)
	9	NGC 4593	43.70 ± 0.13	42.52 ± 0.55	6.7^c	26.04	X	*McKernan et al.* (2007)
	10	NGC 5548	44.30 ± 0.13	41.80 ± 0.26	7.6^a	26.35	X	*McKernan et al.* (2007)
	11	MCG -6-30-15*	43.40 ± 0.13	40.89 ± 0.22	6.5^d	26.01	X	*McKernan et al.* (2007)
	12	Mrk 290	44.40 ± 0.13	42.57 ± 0.36	7.4^a	26.60	C	*Zhang et al.* (2011b)
	13	Mkn 509	45.20 ± 0.13	41.93 ± 0.54	8.2^c	26.65	C	*Ebrero et al.* (2011)
BHB	14	4U 1630	38.20 ± 0.43	32.68 ± 0.96	1.0^i	22.42 ± 0.30^j	X	this paper
	15	GRO 1655−40a	37.70 ± 0.29	32.31 ± 0.56	0.83^g	21.79 ± 0.20^l	X	*Miller et al.* (2008)
	16	GRO 1655−40b	37.80 ± 0.29	33.42 ± 0.66	0.83^g	21.79 ± 0.20^l	X	*Neilsen and Homan* (2012)
	17	H 1743−322 a	38.60 ± 0.46	33.43 ± 0.35	1.0^i	22.42 ± 0.30^j	X	this paper
	18	H 1743−322 b	38.50 ± 0.43	32.32 ± 0.66	1.0^i	22.42 ± 0.30^j	X	this paper

Table 4.2 (cont'd)

		Object	$\log L_{\rm Bol}$ (ergs s^{-1})	$\log L_{\rm wind}/C_v$ (ergs s^{-1})	$\log M_{BH}$ ($M_\odot$)	$\log D$ (cm)	Code	Reference
	19	GRS 1915+105 S1	38.90 ± 0.13	33.42 ± 0.89	1.15^h	22.54 ± 0.03^m	X	*Ueda et al.* (2009)
	20	GRS 1915+105 S2	39.50 ± 0.13	34.09 ± 0.33	1.15^h	22.54 ± 0.03^m	X	*Miller et al.* (2006b)
	21	GRS 1915+105 S3	39.00 ± 0.13	34.35 ± 0.57	1.15^h	22.54 ± 0.03^m	X	this paper
	22	GRS 1915+105 S4	39.10 ± 0.13	33.68 ± 0.62	1.15^h	22.54 ± 0.03^m	X	this paper
	23	GRS 1915+105 S5	39.10 ± 0.13	33.22 ± 0.91	1.15^h	22.54 ± 0.03^m	X	this paper
Jets			$\log L_{Bondi}$ (ergs s^{-1})	$\log L_{Jet}$ (ergs s^{-1})				
AGN	24	NGC 507	44.41 ± 0.09	44.01 ± 0.15	8.9^f	26.34	-	*Allen et al.* (2006)
	25	NGC 4374	43.69 ± 0.30	43.18 ± 0.13	8.8^f	25.72	-	*Allen et al.* (2006)
	26	NGC 4472	43.79 ± 0.25	42.91 ± 0.13	8.9^f	25.72	-	*Allen et al.* (2006)
	27	NGC 4486	44.16 ± 0.35	43.54 ± 0.23	9.5^f	25.72	-	*Allen et al.* (2006)
	28	NGC 4552	43.37 ± 0.22	42.19 ± 0.11	8.7^f	25.72	-	*Allen et al.* (2006)
	29	NGC 4636	42.29 ± 0.24	41.48 ± 0.12	8.2^f	25.72	-	*Allen et al.* (2006)
	30	NGC 4696	43.40 ± 0.56	42.90 ± 0.17	8.6^f	26.14	-	*Allen et al.* (2006)
	31	NGC 5846	42.85 ± 0.42	41.87 ± 0.16	8.6^f	25.88	-	*Allen et al.* (2006)
	32	NGC 6166	43.49 ± 0.30	43.20 ± 0.13	8.9^f	26.62	-	*Allen et al.* (2006)
BHB	33	Cygnus X-1	37.30 ± 0.13	36.00 ± 2.00	1.0^i	21.76 ± 0.04^k	-	this paper
Ultra-Fast Outflows								
AGN	34	3C 111	45.9	45.8	9.0	26.81	X	*Tombesi et al.* (2011)

Table 4.2 (cont'd)

		Object	$\log L_{\mathrm{Bol}}$ (ergs s^{-1})	$\log L_{\mathrm{wind}}/C_v$ (ergs s^{-1})	$\log M_{BH}$ ($M_\odot$)	$\log D$ (cm)	Code	Reference
	35	APM 08279+5255	47.3	50.5	10.3	28.3	-	*Chartas et al.* (2002)
	36	PG 1115+080	46.5	51.2	9.0	28.1	-	*Chartas et al.* (2007)
BHB	37	J17091+3624	37.5	38.3	1.0^i	22.41	X	*King et al.* (2012b)

Note. — * These sources have bolometric luminosities estimated from their 2–10 keV fluxes ($L_{Bol} \approx 20L_{2-10keV}$, *Vasudevan and Fabian*, 2009). The masses are given by each reference unless otherwise stated; *a*: *Denney et al.* (2010), *b*: *Lee* (2005), *c*: *Peterson et al.* (2004), *d*: *McHardy et al.* (2005), *e*: *Collier et al.* (2001), *f*: derived from the relation given in *Tremaine et al.* (2002) using the σ given in *Allen et al.* (2006), *g*: *Shahbaz et al.* (1999), *h Greiner et al.* (2001), *i*: the mass of these BHB has not been determined so a M=10$M_\odot$ and 20% error has been assumed *j*: the distance to these sources is unknown and assumed to be 8.5±4 kpc, *k*: *Reid et al.* (2011), *l*: *Foellmi* (2009), *m*: *Harlaftis and Greiner* (2004). X= XSTAR, C=Cloudy

4.3.2 Supermassive Black Holes

This sample, seen in Table 4.1, is predominately derived from the work by *McKernan et al.* (2007), which is comprised of 15 nearby AGN that were all observed with *Chandra* High Energy Transition Grating Spectrograph (HETGS) before July 1, 2003. The summed MEG first-order spectra were used. For further details of the data reduction, we refer the reader to *McKernan et al.* (2007) and *Yaqoob et al.* (2003).

Owing to the observational selection criteria, only 7 of the 15 AGN show statistically significant blue-shifted absorption features. *McKernan et al.* (2007) perform a uniform analysis with XSTAR models, which characterizes the absorption and emission features seen in the sampled spectra. The XSTAR models were generated assuming an individual SED for each AGN. Each grid of models had an assumed density of $n_e = 10^8$ cm^{-3} and a turbulent velocity of 170 km s^{-1}. These AGN span a redshift range of z=0.003 to z = 0.046, a mass range of $6{\times}10^5 - 10^8$ M$_\odot$, and a range of environments from centers of clusters to field galaxies.

A majority of these AGN had more than one out-flowing component. See Table 4.1. These components were separated not only in velocity space but in ionization parameter as well. In these cases, we took the sum of all the components to evaluate the mass outflow rate, $\dot{M}_{wind}$, and kinetic wind luminosity, $L_{\rm wind}$, so as to compare the total out-flowing material and consequently the total power generated by these winds. See Section 4.4 for details. The values for the kinetic wind power and bolometric luminosities are given in Table 4.1 for individual components and Table 4.2 for the summed components. We have assumed a covering fraction, Ω, of $\Omega = 2\pi$, and given the results per filling factor, C_v.

In addition, six other AGN observations are included in our sample: NGC 4051, NGC 4593, Mkn 509, IRAS 18325−5926, NGC 4151 and Mrk 290. These are all relatively nearby AGN, z = 0.002 – 0.034, with comparable masses spanning M = 2 – 160 $\times 10^6 M_\odot$. *King et al.* (2012a) report observations of the nearby, Seyfert-1

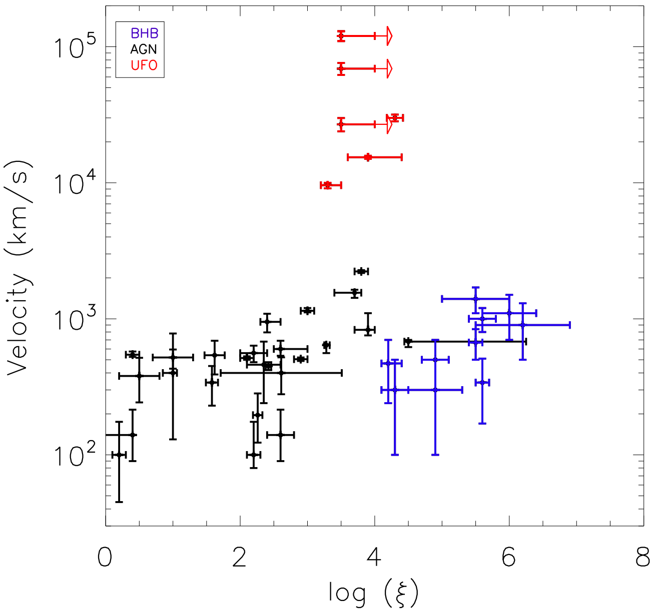

Figure 4.1 The above figure plots the observed velocity components versus ionization, for the slow and "ultra-fast" winds in our black hole sample. In black are the AGN winds, in blue are the BHB winds and in red are the ultra-fast winds. The points with arrows denote lower limits to the ionization state, as the actual state for these ultra fast winds was not analyzed with a photoionization model.

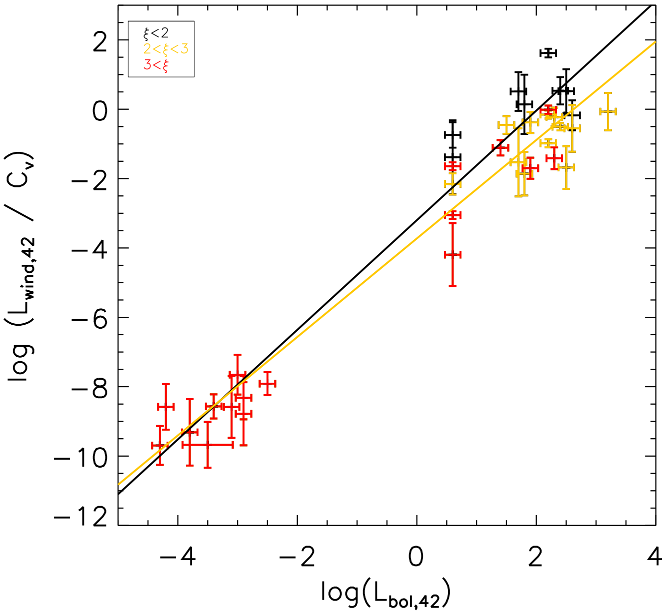

Figure 4.2 The plot above shows the correlation between bolometric luminosity and kinetic wind luminosity in individual outflowing components. The line represents the best fit to the total kinetic luminosities which are plotted in Figure 4.3, while the yellow line is the best fit to the individual components with $\log \xi > 2$. The high ionization parameters are described by the following form $\log(L_{\mathrm{wind},42}) = (1.42 \pm 0.06) \log(L_{\mathrm{Bol},42}) - (3.73 \pm 0.14)$, with an intrinsic scatter of $\sigma_0^{\log \xi > 2} = 0.57$

AGN, NGC 4051 which show evidence of warm-absorbers. They coadded 12 *Chandra* HEG and MEG spectra from November 2008 for a total exposure time of 308 ksec. Although, *McKernan et al.* (2007) report detections of warm-absorbers in NGC 4051, the work by *King et al.* (2012a) uses a different data set which was observed over 5 years later. *King et al.* (2012a) use both XSTAR and Cloudy photoionization codes to create grids of models to fit to the data. By modeling the spectra with two separate photoionization codes, they were able to determine that three different ionization components were required by the data, independent of the model used. For this analysis, we use the three components that were determined using the XSTAR photoionization grids, which span a wide range in ionization and velocity, i.e. $\log \xi = 1, 3.4, \& \ 4.5$ and $v = 400, 630, \& \ 680$.

We also used the work by *Steenbrugge et al.* (2003), who observed NGC 4593, both with *Chandra* LETGS and XMM-Newton. We used only the 108 ksec LETGS spectrum that was analyzed with an XSTAR model. The XMM-Newton observation, taken 7 months later, could not constrain the absorption component ionization; however, it was consistent with the LETGS observation. The statistically significant absorption component in the LETGS observation had an ionization of $\log \xi = 2.61 \pm 0.09$ with an outflowing velocity of 400±121 km s^{-1}.

Ebrero et al. (2011) also used the *Chandra* LETGS to observe the AGN Markarian 509. This 180 ksec observation was modeled with *xabs*, created using Cloudy. The fit to the spectra resulted in 3 components, one of which was significant at the 3σ confidence level. This had an ionization of $\log \xi = 2.26 \pm 0.07$ and a velocity of $v = 196^{+87}_{-73}$ km s^{-1}, and is included in our sample.

In addition, we used the work by *Zhang et al.* (2011a), who observed IRAS 18325−5926 . The authors coadd two exposures from March 2003 to get a total *Chandra* HETG spectrum of 108 ksec. Using a grid of XSTAR models, they find two outflowing absorption components with typical warm absorbing parameters of

$\log \xi = 1.58 \pm 0.09$ and $\log \xi = 2.35 \pm 0.25$ and $\mathrm{v}_{\mathrm{out}} = 340 \pm 110$ km s^{-1} and $\mathrm{v}_{\mathrm{out}} = 460 \pm 220$ km s^{-1}, respectively. We note that *Mocz et al.* (2011) also get results consistent with the higher velocity component.

Kraemer et al. (2005) describe an analysis of NGC 4151, a nearby Seyfert-2 (it is more like a Seyfert-1 in X-rays), using two coadded *Chandra* HETG spectra from May 2002. The total exposure time was 250 ksec. The focus of their work was to describe the absorption features seen in both the X-ray and UV using Cloudy models. *Kraemer et al.* (2005) do not quote the significance of the detection of these features; however, the individual lines are detected at several times their minus-side errors, and modeled together, should be quite significant. The X-ray absorption components taken from *Kraemer et al.* (2005) that are included in our study have ionization parameters of $\log U \approx -0.27$ and $\log U \approx 1.05$ and outflowing velocities of $v_{\mathrm{out}} \approx 500$ km s^{-1}.

Finally, the last AGN in our sample, Markarian 290, is taken from *Zhang et al.* (2011b). We note these authors use both *Chandra* and *XMM-Newton* grating spectra in their analysis. However, we only include the *Chandra* HETG spectra in our analysis. This particular spectrum had three coadded observations giving an exposure time of 166 ksec. The two XSTAR grid components that were statistically significant spanned a range of ionization states from $\log \xi = 1.62 \pm 0.15$ to $\log \xi = 2.45 \pm 0.04$ and a range of velocities from $v_{\mathrm{out}} = 450 \pm 30$ to $v_{\mathrm{out}} = 540 \pm 150$ km s^{-1}, respectively.

4.3.3 Stellar-Mass Black Holes

To the greatest extent possible, values in the literature were used to estimate the kinetic power in winds observed in stellar-mass black holes. As with supermassive black hole winds, only observations obtained with high resolution gratings spectra and some level of photoionization modeling are included. As a result of these considerations, only *Chandra*/HETG spectra were selected. In total, ten observations from four stellar-mass black holes and black hole candidates are included in our initial analysis. It should be noted that many more HETG observations are available – GRS 1915+105 has been observed regularly – but we have only included prominent low- and high-flux spectra from GRS 1915+105 in order to represent the properties of the group rather than just one source. The winds in X-ray binaries have only been detected in the "high/soft" X-ray spectral state (e.g., *Ponti et al.*, 2012). We do not include upper limits when the sources are in the "low/hard" state. See Section 5.2 for more discussion of spectral state dependence.

GRO J1655−40: This is a famous and recurrent transient, and its mass and distance are well-determined ($\mathrm{M} = 7.0 \pm 0.2\ \mathrm{M}_\odot$ and $d = 3.2 \pm 0.2$ kpc *Hjellming and Rupen*, 1995; *Orosz and Bailyn*, 1997). The presence of density-sensitive Fe XXII absorption lines in a *Chandra* spectrum (ObsID 5461) of GRO J1655−40 allowed for direct constraints on the density of the disk wind in this source ($\log(n) = 14$; *Miller et al.*, 2008). Fits with an independent photoionization code, grids of Cloudy models, and grids of XSTAR models are reported in *Miller et al.* (2008). Based on that work, we have used values of $L = 5.0 \pm 0.1 \times 10^{37}$ ergs s^{-1}, an outflow velocity of $v = 500$ km s^{-1}, $\log(\xi) = 4.9 \pm 0.1$, and $\Omega = 2.5$ in estimating the kinetic power of the wind in GRO J1655−40. The wind observed in GRO J1655−40 is particularly complex, and no single velocity characterizes all of the lines observed; $v = 500$ km s^{-1} is a representative value that is used throughout *Miller et al.* (2008) because it captures the outflow well. The resulting kinetic power is broadly consistent with numbers given in *Miller et al.* (2008) estimated using the wind density. We note that *Neilsen and Homan* (2012) also model a *Chandra* observation (ObsID 5460) that was made a month prior to this observation (ObsID 5461). We find evidence for an absorption feature at 6.97 keV, which is consistent with no outflow, and therefore do not include it in this analysis.

H 1743−322: This source is also a well-known and recurrent transient (see, e.g., *Homan et al.*, 2005; *Corbel et al.*, 2005; *Miller et al.*, 2006b; *Miller-Jones et al.*, 2012). The high column density along the line of sight to H 1743−322 has permitted the detection of a counterpart (*Steeghs et al.*, 2003) but has not permitted a radial velocity measurement. In this work, we have assumed a distance of 8.5±0.8 kpc (*Steiner et al.*, 2012), and a fiducial mass of 10 $M_\odot$. During its 2003 outburst, a disk wind was clearly detected in thwo *Chandra*/HETG observations (*Miller et al.*, 2006b); parameters obtained from photoionization modeling of each spectrum are used in this analysis.

In particular, the broadband X-ray spectral fits in table 2 of *Miller et al.* (2006b) were used to derive bolometric luminosities, and the ionization parameters given in table 5 in *Miller et al.* (2006b) are used. The first observation included has an outflowing velocity of 670±170 km s^{-1}, while the second observation included has an outflowing velocity of 340±170 km s^{-1}. The ionization of the two observations are roughly the same at $\log \xi = 5.5 \pm 0.1$ and $\log \xi = 5.6 \pm 0.1$, respectively. Less is known about the binary parameters of H 1743−322 than e.g. GRO J1655−40, and a larger value of $\Omega = 2\pi$ was adopted in calculating the photoionization models (the package used was an update of the code described in *Raymond*, 1993).

GRS 1915+105: This is an extremely well-known microquasar. The mass of the black hole and its distance have been determined (M $= 14 \pm 4$ $M_\odot$; $d = 12.5$ kpc; *Greiner et al.*, 2001). A long *Chandra*/HETGS observation of GRS 1915+105 in a soft phase was analyzed in detail by *Ueda et al.* (2009); some simple photoionization modeling techniques were applied to describe the disk wind that was detected. The broadband spectral fits detailed in that work were used to calculate a bolometric luminosity for this observation ($L = 7.5 \pm 0.8 \times 10^{38}$ ergs s^{-1}). As with the HETGS observation of GRO J1655−40 reported in *Miller et al.* (2008), this spectrum of GRS 1915+105 is particularly rich, and no single velocity can describe all of the ions observed. In this work, we adopt a value of $v = 300$ km s^{-1} because it is consistent with many ions and achieves a balance between the most and least ionized components of the flow. The line properties and analysis reported in *Ueda et al.* (2009) are consistent with $\Omega = 2.5$ and $\log(\xi) = 4.3$ (errors are not reported). We have used these values in calculating the kinetic power of the wind in this observation.

Neilsen and Lee (2009) treat a number of *Chandra*/HETGS observations of GRS 1915+105. *Ueda et al.* (2009) focused on the observation called "S1" in the *Neilsen and Lee* (2009) scheme; it is the lowest luminosity of five "soft" observations considered in their work. In each soft observation, an ionized X-ray disk wind is detected at high significance. To understand the range of wind properties in this important source, then, we have included observations S2–S4 in this analysis.

Reduced and calibrated spectral and response files for each observation were obtained through the *Chandra* "tgcat" facility (for details of the observations, please consult *Neilsen and Lee*, 2009). The combined first-order HEG spectrum from each observation was fit in the 2.3–9.0 keV band with a simple phenomenological model consisting of disk blackbody and power-law components. The lower energy bound was set by the high column density along the line of sight to GRS 1915+105 (N_H was fixed at 5.0×10^{22} cm^2 in each case); the upper bound was set by the likely calibration residuals in the high energy portion of the spectra. This continuum model is not unique, but it allows for a simple and accurate characterization of the flux in the observed energy band, and gives reasonable basis for extrapolating to the 0.5-10.0 keV band.

We then calculated and applied grids of XSTAR models. A customized grid was made for each observation, using the observed spectral continuum and the unabsorbed 0.5–10.0 keV luminosity as the spectral input (the power-law was truncated below 1 keV to prevent unphysical results). Again, additional details of this procedure can be found in *Miller et al.* (2006a, 2008) and *King et al.* (2012a,b). In all cases, a turbulent velocity of 500 km/s, an iron abundance of 2.0 times the solar value (e.g. *Ueda et al.*, 2009), a density of $\log(n) = 12.0$, and a covering factor of $\Omega = 2.5$ were assumed. In estimating the kinetic power in the wind for observations S2–S5, we used the velocity shifts reported by *Neilsen and Lee* (2009), and the ionization parameters measured through direct fits to the *Chandra* spectra with the XSTAR models. The values for all relevant parameters are given in Table 4.2.

4U 1630−47: Last, we considered an archival *Chandra* HETG observation of the black hole candidate 4U 1630−47. Observation 4568 started on 2005 August 9 at 20:16:02 (UT), with a duration of 50 ksec. The instrumental configuration and modes used were the same as those described in *Miller et al.* (2008). We again downloaded the calibrated first-order gratings spectra and responses using the *Chandra* "tgcat" facility, and generated a combined first-order HEG spectrum.

Fits to the continuum with an absorbed disk blackbody plus power-law model give a high column density ($N_H = 7.8 \times 10^{21}$ cm^{-2}), a fairly hot disk ($kT = 1.36 \pm 0.01$ keV), and a power-law index of $\Gamma = 2.00 \pm 0.02$. (The power-law index was checked by making fits to a simultaneous *RXTE* PCA spectrum over the 3–30 keV band.) Assuming a distance of 8.5 kpc, this continuum model gives a bolometric luminosity of $2.2 \pm 0.2 \times 10^{38}$ ergs s^{-1}. We further assume a mass of 10 $M_\odot$ for 4U 1630−47 in this work.

Again as per the procedure in *Miller et al.* (2008), this spectrum was used to illuminate gas in a grid of XSTAR models. Solar abundances were assumed, and a turbulent velocity of 500 km s^{-1} was found to give the best fits to the data. As with H 1743−322, the parameters of the binary system are not well known, and a covering factor of $\Omega = 2\pi$ was assumed in the generating the photoionization models. A fiducial density of $\log(n) = 12$ was also assumed in generating the models. As per the high luminosity observation of GRS 1915+105, only an H-like Fe XXVI line was detected, immediately indicating a high ionization. Direct fits with the XSTAR grid give an ionization of $\log(\xi) = 4.9 \pm 0.4$, and a blue-shift of $v = 300 \pm 200$ km s^{-1}.

4.3.4 Jet Power

In collecting a jet sample, we also wanted to create a set of uniform standards and conditions that would ensure high quality and rigorous results just as we had done for the wind sample. Jets are found in the radio as a result of synchrotron radiation, so it is tempting to utilize the radiative portion of the energy as an estimate for the jet power (e.g., *Merloni and Heinz*, 2007). However, the majority of the energy carried off by the jets appears to be mechanical, not radiative (*Heinz et al.*, 2002; *Di Matteo et al.*, 2003; *Gallo et al.*, 2005; *Allen et al.*, 2006; *Taylor et al.*, 2006). We note that *Merloni and Heinz* (2007) and *Cavagnolo et al.* (2010) do find a relation between radio emission and mechanical power in jets, but a direct determination of the power is preferred over a proxy such as radio luminosity. In addition, *Cavagnolo et al.* (2010) report the jet power relation to have a scatter of 0.70 dex and to be calibrated to high luminosity sources. It is unclear if extrapolation to lower luminosity sources is applicable. Likewise, the radio luminosities of jets are also subject to Doppler boosting (*Urry and Padovani*, 1991), which can be difficult to de-project, since the intrinsic spectrum must be known. We therefore restrict ourselves to only the most tentative of comparisons to radio luminosity via the fundamental plane of accretion onto black holes (*Merloni et al.*, 2003; *Falcke et al.*, 2004a; *Gültekin et al.*, 2009a). This plane relates the radio luminosity of SMBH to the accretion rate (via X-ray luminosity) and mass of the black hole. See Section 4.5.5 for further discussion.

For a more stringent comparison with our wind sample, we require that the jet power be a direct estimate of the mechanical energy, not an indirect estimate using the radiative luminosity as a proxy for jet power. One way of quantifying the amount of mechanical power released via jets is to look at the volume they carve out in the form of “cavities” or “bubbles”. These cavities are seen in both the radio and X-ray wavelengths. The energy ($E_{\rm Jet}$) is then estimated to be the sum of the internal energy and the PdV work done to inflate the bubble. The time needed to carve out such a region is estimated at t_{age}=R/c$_s$, where t_{age} is the age of the bubble, R is the distance from the black hole to the center of the cavity and c_s is the sound speed, typically estimated using X-ray observations. There are a number of different ways to estimate the age of the bubble, but using sound speed and bubble radius is a fine approximation as long as the bubble is still "attached" and is not buoyantly rising (*Dunn and Fabian*, 2004). Therefore, the power of the jet is $P_{\rm Jet} = E_{\rm Jet}/t_{age}$. We note here that this estimate is a long term average and is not sensitive to discrete episodes of jet emission, which would serve to increase the jet power estimate.

For this work, we draw directly from the sample described in *Allen et al.* (2006), who use this prescription to analyze a sample of nine elliptical galaxies that display such X-ray and radio cavities. They also estimated the Bondi mass accretion rates by constructing radial temperature profiles close to the black hole from *Chandra* X-ray observations. As the *Allen et al.* (2006) is a study of elliptical galaxies at low accretion rates, spherical accretion, i.e. Bondi accretion, is assumed with an efficiency conversion between mass accretion rate and luminosity ($\eta = 0.1$ as given in *Allen et al.*, 2006). Conversely, in the wind sample, the accretion rates are typically higher at a few percent of Eddington, and the accretion is assumed to be through a standard thin disk. We use both the jet power and Bondi luminosities reported in *Allen et al.* (2006). We used the Bondi luminosities instead of the bolometric luminosities because each is an appropriate estimate for the mass accretion rate in these particular systems. *Merloni and Heinz* (2007) report analysis of the same nine AGN as *Allen et al.* (2006) as well as six additional sources. We do not include these extra sources in our sample as the temperature inside the Bondi radius was not measured directly but extrapolated from much further, outside regions. However, as will be shown in Section 4.5.2, *Merloni and Heinz* (2007) report consistent analysis and results with *Allen et al.* (2006).

At the low mass end, it is much more difficult to use the same methods to estimate the jet power from bubbles and cavities. This is because most of the black hole candidates are not in regions with dense gas, making the bubbles hard to observe. The few that are embedded in dense clouds happen to also be in star forming regions. This means that the observed cavities can be carved out not only by their jets, but also by their high mass companion star's winds or even the supernovae associated with the black holes themselves. One such candidate is BHB, Cygnus X-1. This is a stellar mass black hole with an associated radio bubble that is thought to be created by its jet (*Gallo et al.*, 2005; *Russell et al.*, 2007). This is evidenced by the fact that the long axis of the bubble is aligned with the jet axis. However, there is no counter-jet seen, and the bubble may also be associated with a supernova remnant (*Russell et al.*, 2007).

Gallo et al. (2005) and *Russell et al.* (2007) have both used the observed cavity to estimate the power of the jet, employing similar techniques as *Allen et al.* (2006). We note that in making density estimates of the emitting region, both *Gallo et al.* (2005) and *Russell et al.* (2007) assume the emission is Bremsstrahlung radiation. However, as *Marti et al.* (1996) show, the radio emission in the limb brightened areas have steep spectra, which implies the regions are non-thermal in nature. Moreover, *Russell et al.* (2007) find that the emitting loop is not visible in the R band, indicating that the emission detected with an Hα filter, is in fact Hα rather than Bremsstrahlung emission, as assumed by Gallo et al. (2005).

One can use the observed Hα flux to estimate the average density of ionized gas (about 6 cm^{-3}) and follow the method of *Gallo et al.* (2005) to determine the jet power, $P_{\rm Jet} = 10^{34} - 10^{38}$ ergs s^{-1}. As is obvious by the four orders of magnitude, there are large uncertainties that go into this calculation. Clumpiness of the emitting gas would give an overestimate of the average density, and if the ionized gas is indeed produced by a 100 km s^{-1} shock, it occupies a very thin sheet compared to the apparent size of the emitting region. Second, the neutral fraction in the emitting region, taken to be 98% by *Gallo et al.* (2005) and zero by *Russell et al.* (2007), is not well known. Finally, when shocked gas has cooled to the point that Hα emission is efficient, its pressure is probably dominated by the magnetic field, so the sound speed should be replaced by the fast mode speed, which is several times larger.

Instead, if we combine the intensity measurements of *Russell et al.* (2007) with the shock wave models of *Raymond et al.* (1988) and the theory of interstellar bubbles blown by a continuous energy input (*Castor et al.*, 1975; *Weaver et al.*, 1977), we can get a tighter constraint on the power estimate. *Russell et al.* (2007) measured an intensity in the [O III] $\lambda\lambda$5007, 4959 lines of approximately 1.5×10^{-15} ergs cm^{-2} s^{-1} per square arcsec after correction for extinction, in a 2' section of a cut through the NE part of the shell. They also measured [O III] to Hα + [N II] ratios that indicate shock speeds of 90-200 km s^{-1} (their figure 7). Shock waves in that range produce 0.87±0.2 photons in the [O III] lines per H atom that passes through the shock (*Raymond et al.*, 1988). The shell is limb-brightened, and comparison of the 2' thickness with the 5' radius indicates an enhancement factor of 2.4. Thus

$$1.7 \times 10^7 = 2.4 * 0.87 * n_0 V_s/(4\pi) \text{photons cm}^{-2}\ \text{s}^{-1}\ \text{sr}^{-1} \tag{4.1}$$

where n_0 is the pre-shock density and V_s is the shock speed in units of cm s^{-1}. Thus $n_0 V_s = 1.0 \times 10^8$. The expression for the radius of a wind-blown bubble in the intermediate stage (when the shock is radiative as in the Cygnus X-1 bubble; equation 21 of *Weaver et al.*, 1977) can be converted to

$$L_{37} = 7.7 \times 10^{-8} n_0 V_s V_{100}^2 R_5^2 \tag{4.2}$$

where L_{37} is the jet luminosity in units of 10^{37} erg s^{-1}, $n_0 V_s$ is in units of cm s^{-1}, V_{100} is the shock speed in units of 100 km s^{-1} and R_5 is the bubble radius in units of 5 pc. For a shock speed of 90-200 km s^{-1} and an average bubble radius of 4 pc, this impies a jet luminosity of $4 - 20 \times 10^{37}$ erg s^{-1}.

There are two important caveats to keep in mind, both of which could lead to a severe overestimate of the jet luminosity. First, O stars in the region, including the companion of Cyg X-1 itself, might contribute ionizing flux that we are assuming to come from the bubble shock. Second, the shell could be a result of the explosion that created the Cyg X-1 black hole, rather than the jet. The alignment of the shell with the jet direction suggests, however, that the jet plays a significant role in the energetic of the bubble. In addition, there is some uncertainty involved with the reddening correction. In view of the uncertainties in the relevant quantities, in the best method of estimating the power required to inflate the bubble, and the origin of the bubble itself, we use the full range of power estimates noted above. We note there are tighter constraints if the bubble is only associated with inflation by the jet and reddening is unimportant.

4.3.5 Ultra-Fast Outflows

Finally, we also defined a smaller subsample of winds that are moving faster than 3,000 km s^{-1} (0.01c) relative to the systemic velocity. For this sample, we relax our standards for the AGN and include both *Suzaku* and *Chandra* imaging spectrometers. As we only discuss four examples of these outflows, (one BHB, one nearby quasar and two gravitationally lensed, higher redshift quasars), this additional data set is only meant to be illustrative not exhaustive. This sample still requires that the absorption features be at least 3σ significance.

The first of these ultra fast outflows is the BHB J17091−3624. *King et al.* (2012b) discus two *Chandra* HETG observations, one of which has clear absorption features above 6.9 keV. Using XSTAR photoionization grids, they model these features self-consistently and find an ionization of the absorbing gas to be $\log \xi = 3.3^{+0.2}_{-0.1}$, moving at $v_{\rm out} = 9600^{+400}_{-500}$ km s^{-1}. We also use the second component at a slightly higher ionization state $\log \xi = 3.9^{+0.5}_{-0.3}$ and velocity, $v_{\rm out} = 15,400 \pm 400$ km s^{-1}. These are the fastest outflows observed from a BHB candidate, and they bear resemblance to some of the outflows seen in quasars (e.g., *Chartas et al.*, 2002, 2007; *Tombesi et al.*, 2011).

Tombesi et al. (2011) used the *Suzaku* X-ray Imaging Spectrometer (XIS) to observe 3C 111, an AGN at z = 0.0485. Of the three observations in their study, one showed evidence of an absorption line in the Fe K band. This observation had an exposure of 59 ksec. Using XSTAR grids with turbulent velocity of 3000 km s^{-1}, this one feature was fit with an ionization parameter of $\log \xi = 4.32 \pm 0.12$ and an outflowing velocity of $v_{\rm out} = 0.106 \pm 0.006c$.

Chartas et al. (2002) observed the quasar APM 08279+5255 with the *Chandra* Advanced CCD Imaging Spectrometer (ACIS) and noted outflows in the absorption spectra. By using lensed quasars, one is able to probe outflows which would otherwise be too faint to observe. This quasar is at a redshift of $z = 3.91$. The spectra of APM 08279+5255 shows two features at 8.05 keV and 9.79 keV in the rest frame of the host galaxy (*Chartas et al.*, 2002). If these correspond to Fe XXV then the outflowing velocities would be $0.2c$ and $0.4c$, respectively. We utilized both components in this analysis.

Finally, *Chartas et al.* (2007) described a gravitationally lensed quasar PG 1115+080, which is at a redshift of $z = 1.72$. The authors also used ACIS and notice absorption features in the host Fe K band. PG 1115+080 has prominent absorption features at rest frame energies of 7.27 keV and 9.79 keV; both of which are used in our analysis. Associating these features with Fe XXV gives velocities of $0.09c$ and $0.40c$. These features were not modeled with a photoionization model, but an assumed ionization of $\log \xi = 3.5$ is taken as an estimate for the ionization parameter from XSTAR models (*Chartas et al.*, 2007). Bolometric luminosities are taken from *Chartas et al.* (2007), while estimates of the ionizing luminosities were taken as the rest frame X-ray luminosity from 0.2–10 keV from *Dai et al.* (2004).

4.4 Methods

After acquiring the sample, we calculate the mass outflow rate in the wind systems. This is done using simplified, order of magnitude estimates based on the expression for spherical wind. It is modified by both covering and filling factors to account for the fact that winds are not spherical outflows:

$$\dot{M}_{\rm out} = \Omega \rho r^2 v C_v \tag{4.3}$$

where, Ω is the covering factor ($0 < \Omega < 4\pi$), ρ is the mass density ($\rho = \mu m_p n_e$), μ is the mean atomic weight assumed to be $\mu = 1.23$, m_p is the mass of a proton, n_e is the electron density, r is the radius from the ionizing source, v is the out-flowing velocity, and C_v is the line of sight global filling factor. As the winds may be clumpy and filamentary, they are likely to have a small filling factor. This expectation is based on the observed variability of the absorption lines (e.g., *Crenshaw et al.*, 2003; *Elvis et al.*, 2004; *Risaliti et al.*, 2009) as well as density diagnostics (e.g., *King et al.*, 2012a). We note that variability can be due to both motion along our line-of-sight as well as the duty cycle of the wind. The short timescales of variability suggest that the variability is likely due to small filling factor and clouds moving across our line of sight rather then dissipation of the wind itself. Further, there is an inconsistency in the literature as to the actual filling factors, as there are few direct constraints on this quantity. This factor should vary between different sources as well as with ionization, ξ, but a range from 10^{-5} to 1 is seen in the literature across the full mass scale (e.g., *Miller et al.*, 2008; *Mocz et al.*, 2011; *Zhang et al.*, 2011b; *King et al.*, 2012a,b). Finally, as shown in *Giustini and Proga* (2012), the exact nature of the wind may depend on the ionization, velocity and density of the wind, and may be quite uncertain. Therefore, we do not assume a value for the filling factor for any of the measurements but leave the kinetic energy luminosity in terms of the filling factor.

Equation 4.3 can be rewritten in terms of observable quantities from the X-ray absorption features using $\xi = L_{ion}/n_e r^2$, where ξ is the ionization parameter and L_{ion} is the ionizing luminosity between $1 - 1000$ Ryd (1 Ryd = 13.6 eV).

$$\dot{M}_{\rm out} = \frac{\mu m_p \Omega L_{ion} v C_v}{\xi} \tag{4.4}$$

For consistency, we use $\Omega = 2\pi$ for all the AGN sources, based on findings by *Reynolds* (1997) who found half of all Seyferts show evidence for warm absorbers. We have not assumed a filling factor, C_v, but have reported our results of kinetic luminosity per filling factor. To convert the mass outflow rate to the kinetic energy carried away by the warm absorbing winds, i.e., power or kinetic luminosity, we use the following relation,

$$L_{\rm wind} = \frac{1}{2}\dot{M}_{\rm out} v^2 = \frac{\mu m_p \Omega L_{ion} v^3 C_v}{2\xi}. \tag{4.5}$$

The total kinetic luminosity is the amount of mechanical energy that is carried away by the wind. It is important to understand this in the context of the total escaping energy of the black hole and accretion disk. This can be done via comparison to the radiative power released, i.e., the bolometric luminosity. Further, the bolometric luminosity is often considered a proxy for the mass accretion rate by assuming an efficiency conversion, $L_{\rm Bol} = \eta \dot{M} c^2$. The efficiency, η, is usually assumed to be 10% (e.g., *Allen et al.*, 2006; *Vasudevan and Fabian*, 2009; *Fabian et al.*, 2009), which is consistent with the Soltan's argument (*Soltan*, 1982). However, in reality it is likely to vary between sources and with Eddington fraction. In our study, the bolometric luminosities for the AGN are taken from broad-band spectral energy distribution (SED) fitting performed by *Vasudevan and Fabian* (2009). In the few instances that the AGN lack a bolometric luminosity, we used the conversion $L_{\rm Bol} \approx 20 L_{2-10keV}$ (*Vasudevan and Fabian*, 2009). For the stellar-mass black holes, their SED peaks in the X-ray. Therefore, the bolometric luminosities are taken from the X-ray observations as the luminosity between 0.5-10.0 keV. Where values in the literature were quoted for different energy bands, the luminosity was converted to the 0.5-10.0 keV band for consistency by extrapolating the given models within Xspec. We also note that any uncertainty in distance, which could effect the bolometric and ionizing luminosities as well as estimates of the outflowing velocity, are small as compared to the uncertainties in these measured quantities.

The jet power is calculated using the energy estimates of radio and X-ray cavities and age of the bubble as described in Section 4.3.4, $P_{\rm Jet} = E_{\rm Jet}/t_{age}$. We again note that this estimate is a long term average and short, discrete episodes of jet emission would increase the jet power estimates.

4.5 Analysis and Results

4.5.1 Bolometric Luminosity versus Wind Power

After acquiring a sample of BHB and AGN with estimates for the wind power, we begin to analyze how $L_{\rm Bol}$ relates to the total kinetic outflowing power in each system. In this initial analysis, we only include the lower velocity winds (not the jets, which we consider in Section 4.5.2, or the ultra-fast outflows, which we consider in Section 4.5.4). Figure 4.1 shows the distribution of velocities and ionization parameters that are included in the kinetic power of the winds. Figure 4.2 shows the kinetic wind luminosity as compared to the source bolometric luminosity for individual components in each observation, while Figure 4.3 shows the same plot but for the total kinetic wind luminosity for each observation. The stellar-mass black holes cluster at the lower luminosities, while the SMBH are found at the higher luminosities as expected.

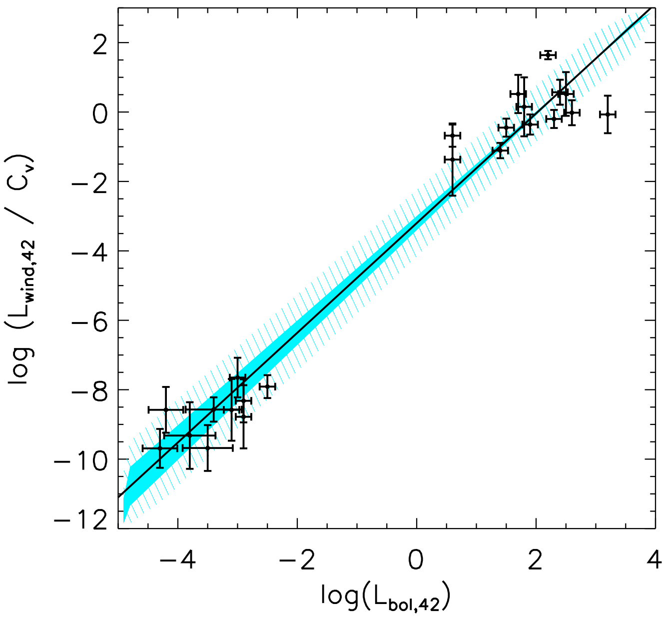

Figure 4.3 The plot above shows the correlation between bolometric luminosity and kinetic wind luminosity. The black line is described by $\log(L_{\mathrm{wind},42}) = (1.58 \pm 0.07)\log(L_{\mathrm{Bol},42}) - (3.19 \pm 0.19)$, with an intrinsic scatter of $\sigma_0 = 0.68$. The blue dashed region is the 1σ confidence region including the scatter of the relation. The solid region is the 1σ confidence region excluding the scatter. The wind kinetic luminosity is plotted per filling factor. The plot shows a simple regulation of wind production across a large mass scale, and the slope indicates that the SMBH winds are more efficient then the stellar-mass black holes.

A positive correlation is apparent in the data set.

In Figure 4.2 (as well as the following figures), we plot the kinetic luminosity per filling factor, C_v, versus the bolometric luminosity. Further, Figure 4.3 shows the total kinetic power for each observation, which uses the sum of the individual components plotted in Figure 4.2. We begin our analysis with the total kinetic power for each observation. Initially, we assume that there is a common relation between both the AGN and BHB. In Section 4.5.5, we relax this assumption and characterize the two groups separately.

To first characterize the trend given in Figure 4.3, we utilize two correlation tests: a Spearman's rank test and a Kendall's τ_K test. We find a Spearman's rank coefficient

$\rho_S = 0.89$, with a null hypothesis probability (i.e., no correlation) at $p = 1.8 \times 10^{-8}$, indicating a strong and positive correlation. The value for Kendall's coefficient is $\tau_K = 0.72$ with $p = 1.4 \times 10^{-6}$, also indicating a strong, positive correlation.

Following this, we assume that the data can be described by the linear relation,

$$y = \alpha x + \beta \tag{4.6}$$

where, $y = \log(L_{\mathrm{wind},42}/C_v)$, $x = \log(L_{\mathrm{Bol},42})$, and the subscript "42" denotes the units 10^{42} erg s^{-1}. We then minimize the function,

$$\chi^2 \equiv \sum_{i=1}^{N} \frac{(y_i - \beta - \alpha x_i)^2}{\alpha^2 \sigma_{xi}^2 + \sigma_{yi}^2 + \sigma_0^2} \tag{4.7}$$

to estimate α and β (e.g., *Press et al.*, 1992; *Tremaine et al.*, 2002). Here σ_{yi} and σ_{xi} are the errors associated with the kinetic wind luminosity and the bolometric luminosity, respectively. The quantity σ_0 is the intrinsic scatter in the relation and is determined by ensuring the reduced χ^2 is close to unity. We obtain $\alpha = 1.58 \pm 0.07$, $\beta = -3.19 \pm 0.19$ and $\sigma_0 = 0.68$, such that,

$$\begin{aligned} &\log\left(L_{\mathrm{wind},42}/C_v\right) = \\ &\quad (1.58 \pm 0.07) \log\left(L_{\mathrm{Bol},42}\right) - (3.19 \pm 0.19). \end{aligned} \tag{4.8}$$

These parameters are listed in Table 4.3. The large σ_0 implies that the intrinsic scatter in these measurements is dominant over the measurement errors. We can expect a high intrinsic scatter due to the high variability of each of these sources, especially because the observations used to derive the AGN bolometric and wind luminosities of individual sources were not made simultaneously. Environment may also play a large role in driving this scatter, evidenced by the fact that the larger scatter is associated with the SMBH measurements, which are located in dense groups

Table 4.3. Individual X-ray Wind Components

Data Set	α	β	γ	σ_0
Winds				
ALL	1.58±0.07	-(3.19±0.19)		0.68
BHB	0.91±0.31	-(5.58±1.68)		0
AGN	0.63±0.30	-(1.24±0.63)		0.58
$\log \xi > 2$	1.42±0.06	-(3.73±0.14)		0.56
ALL	0.2±0.4	1.2±0.3	24.5±0.2	0.68
Jets				
ALL	1.18±0.24	-(0.96±0.43)		0
AGN	1.34±0.50	-(0.80±0.82)		0

Note. — These are the best fit parameters for each of our linear models. The α parameter describes the coefficient of the bolometric or Bondi luminosity, β is the normalization of each linear fit except for the last wind fit. In that case it is the coefficient of the mass term and γ is the normalization of the fit. Finally, σ_0 is the intrinsic scatter of each fit.

and clusters to open field environments. This scatter may also be attributed to the bolometric correction applied to the X-ray luminosities of the AGN and not to the BHB which peak in luminosity in the X-ray band.

Finally, the scatter may be due to the inclusion of a range of ionization parameters, especially in the AGN. There appears to be a stratification in the power which may depend on the ionization parameters. This is shown in Figure 4.2 as the low ionization components tend to have higher powers as compared to the higher ionization parameters. Therefore, we also examine only the high ionization, i.e. $\log \xi > 2$, components with an aim to better compare the same sample in both AGN and BHB. We fit the individual components with high ionization and find the slope flattens to $\alpha^{\log \xi > 2} = 1.42 \pm 0.06$, $\beta^{\log \xi > 2} = -(3.73 \pm 0.14)$ and a scatter of $\sigma_0^{\log \xi > 2} = 0.57$. These results are given in Table 4.3 and shown in Figure 4.2.

4.5.2 Jet Power

We next include the relation between the Bondi luminosity and jet power as estimated via the radio bubbles seen in elliptical galaxies and Cygnus X-1 (See Figure

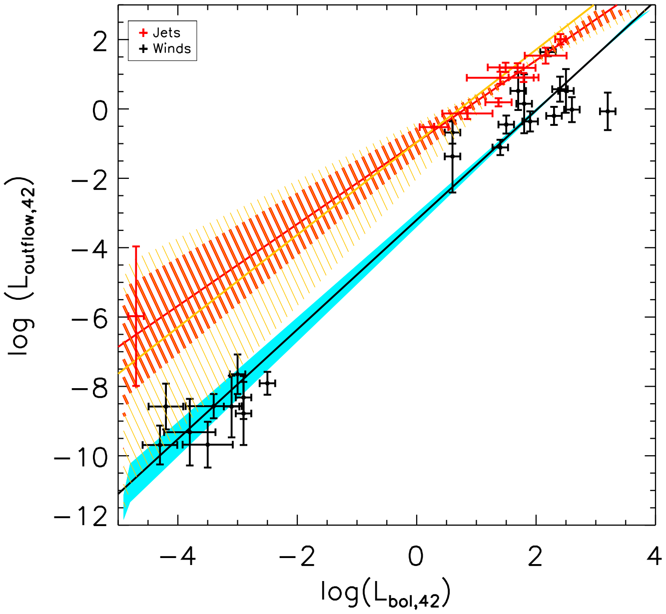

Figure 4.4 The plot above depicts the wind power versus the bolometric luminosity, just like Figure 4.3, but this figure includes the jet power as red data points. The red line describes all the jet points as $\log(L_{\mathrm{Jet},42}) = (1.18 \pm 0.24)\log(L_{\mathrm{Bondi},42}) - (0.96 \pm 0.43)$. The yellow line describes the data set if Cygnus X-1 is excluded from the fit is given as $\log(L_{\mathrm{Jet},42}) = (1.34 \pm 0.50)\log(L_{\mathrm{Bondi},42}) - (0.80 \pm 0.82)$. The dashed regions are the 1σ confidence regions. The orange line and dashed region is the best fit line and 1σ confidence region when excluding Cygnus X-1 from the fit. One can see that the normalization of the jets is higher, demonstrating that for a given bolometric luminosity they are more powerful. One can also see that the slope between the two relations is quite similar, perhaps indicating a common launching mechanism

4.4 and Table 4.2). Again, the Bondi luminosity is used for the ellipticals instead of bolometric luminosity as in the wind sample, but can be thought of as a proxy for mass accretion rate just as the bolometric luminosity is at high accretion rates. For the jet sample, a high degree of correlation between the Bondi luminosity and the jet power is indicated, as initially noted by *Allen et al.* (2006). We find a Spearman's rank coefficient of $\rho_S = 0.95$ with probability $p = 2.3 \times 10^{-5}$, and a Kendall's τ_K coefficient of $\tau_K = 0.87$ with probability $p = 4.9 \times 10^{-4}$. Clearly, there is a positive correlation for this data set as well.

As a correlation is quite apparent in this jet sample, we fit the data using the same technique as was used for Sections 4.5.1. We find a $\alpha^{jet} = 1.18 \pm 0.24$, $\beta^{jet} = -(0.96 \pm 0.43)$, and a intrinsic scatter consistent with zero ($\sigma_0^{jet} = 0$). These parameters are listed in Table 4.3 for comparison with the wind parameters. This relation is also shown in red in Figure 4.4. The reduced χ^2 is quite small at $\chi^2/\nu = 0.11$. This is a result of the large uncertainty estimates on the Bondi luminosities. The error in Bondi luminosity is estimated using the uncertainty given in *Allen et al.* (2006) as well as the uncertainty derived from the scatter in the $M - \sigma$ relation given by *Gültekin et al.* (2009b). These two uncertainties are added in quadrature, resulting in an uncertainty of approximately 0.62 dex.

As *Allen et al.* (2006) and *Merloni and Heinz* (2007) perform similar fits to exclusively the elliptical galaxies, we next exclude Cygnus X-1 from the fit and find $\alpha^{jet} = 1.34 \pm 0.50$, $\beta^{jet} = -(0.80 \pm 0.82)$ and an intrinsic scatter also consistent with zero. See the orange line in Figure 4.4. Our analysis is able to reproduce the results by *Allen et al.* (2006), who first published this sample. *Allen et al.* (2006) find $B = 0.77 \pm 0.20$, which is equivalent to $\alpha^{jet} = 1.30 \pm 0.34$ in our nomenclature. Our results are also consistent with *Merloni and Heinz* (2007) who find a slope of $\alpha^{jet} = 1.6^{+0.4}_{-0.3}$ when correlating $\text{Ł}_{Kin}/L_{\mathrm{Edd}}$ to $L_{Bondi}/L_{\mathrm{Edd}}$.

We note here that Cygnus X-1 nominally lies one or two orders of magnitude above the elliptical jet relation but is consistent within its large uncertainty. This begs the question whether the radio bubble seen around Cygnus X-1 is truly related to the black hole jet or in fact a chance alignment. Cygnus X-1 is located in a fairly active star forming region where massive young stars may be responsible for such a structure (*Reid et al.*, 2011). In fact, there have been X-ray winds associated with the Cygnus X-1 system, whether from the accretion disk or the companion O star is unclear. These may also have an effect on inflating the bubble, which would bring the power estimate down. In addition, as previously discussed, we do not see a counter bubble from the presumed counter-jet.

If we include Cygnus X-1 in the jet relation, then the slope of the jet relation is inconsistent with the wind relation by only 1.6σ. However, when we exclude Cygnus X-1 (as it is plausibly associated with a supernova remnant *Russell et al.*, 2007) the slopes of the jet and wind relations are consistent within errors. Although the normalizations are different, a common slope might imply a shared driving mechanism. In Figure 4.4, it is apparent that the jet and wind power normalizations are within a few orders of magnitude, especially at high luminosity. However, correcting for the filamentary and geometric structure of the winds via the filling factor will decrease the wind power normalization by 3 to 4 orders of magnitudes, demonstrating the greater efficiency of the jet power.

4.5.3 Spectral State Dependence

It is also interesting to compare how jet and wind power scale in terms of Eddington fraction to examine the accretion rate dependence. Figure 4.5 shows both the wind and jet power per Eddington luminosity as compared to their Eddington fraction (i.e., bolometric luminosity or Bondi luminosity per Eddington luminosity). The AGN jet power is denoted in red, Cygnus X-1 jet power is denoted in orange, the AGN winds are denoted in black, and the BHB winds are denoted in blue. The solid lines are taken from *Churazov et al.* (2005) and describe the outflow mechanical power (thick line) and radiative power (thin line) for AGN. They postulate that AGN should follow a similar evolution to their stellar-mass counterparts, in that they should have a strong jet dominated phase at low accretion rates, and little-to-no jet production at high accretion rates. This allowed them to present a model for AGN feedback and co-evolution with the host galaxies as a function of mass accretion rate. We assume an efficiency of $\eta = 0.1$ to compare our bolometric luminosity to their mass accretion rate.

A division in the outflow power is seen at approximately $10^{-2} L_{\mathrm{Edd}}$ in our data

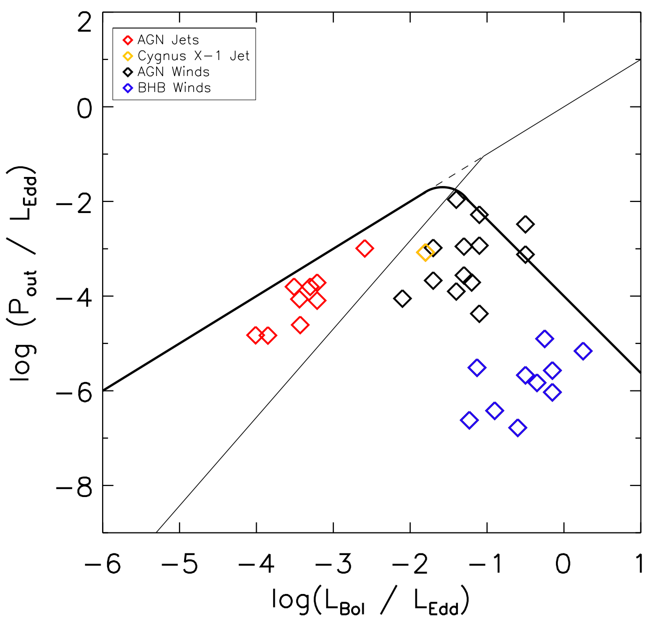

Figure 4.5 The above plot shows the power emitted either from the jet power (AGN:red and BHB:orange) or wind power (AGN:black and BHB:blue) as a compared to the mass accretion rate, which is approximated by the bolometric luminosity on the x axis. A clear turnover at $\dot{M}_{acc} \approx 10^{-2}\dot{M}_{\rm Edd}$ indicates where the power emitted is becoming less efficient. Interesting is the dichotomy between where the jets lie at lower mass accretion rates and where the winds lie at higher accretion rates. The thick black line denotes the output power by outflows, where as the thin line is the power generated by radiation as described by *Churazov et al.* (2005)

set. See Figure 4.5. Below this Eddington fraction, jets dominate and increase in power with bolometric luminosity. At higher Eddington fractions, the wind power dominates but decreases with Eddington fraction. We note that there is an observed dichotomy between the type of outflows seen in stellar mass black holes and their X-ray spectral state already described in the literature. In particular, winds are found in the "high/soft" state, i.e., high mass accretion rate and Eddington fractions ($\gtrsim 10^{-2} L_{\rm Edd}$), and radio jets are observed in the "low/hard" state, i.e. low mass accretion rates and Eddington fractions (*Miller et al.*, 2006a, 2008; *Neilsen and Lee*, 2009). Although our sample is not exhaustive, we do see illustration of a similar trend in the AGN sample where jets persist at low Eddington fractions and winds persist at high Eddington fractions. We note that in one AGN source, NGC 4051, there is evidence for simultaneous winds and jets (*King et al.*, 2011). However, the winds may very well dominate at this high Eddington fraction in NGC 4051. Regardless of the particular outflow seen, Figure 4.5 allows for the prediction of the outflow power as a function of Eddington fraction. *This will be vital to simulations of AGN feedback and co-evolution; both for matching predictions to observations as well as implementing sub-grid physics in cosmological simulations.*

4.5.4 Ultra-Fast Outflows

There are a few wind sources that lie well above the wind relation in Figure 4.3 and much closer to the jet relation in Figure 4.4. This is primarily because of their high velocities, i.e., $v > 0.01c$, as $L_{\rm wind} \propto v^3/\xi$, which increases their power to lie near the jet relation. In Figure 4.6, we include four ultra-fast outflows mentioned in Section 4.3.5. These are denoted in the black squares. The upper squares assume a global filling factor of unity. For comparison, we include estimates of the wind luminosity if the filling factor were as low as $C_v = 10^{-4}$ connected by a dashed line to the original higher estimate. Such a small filling factor is reasonable as it is consistent with their

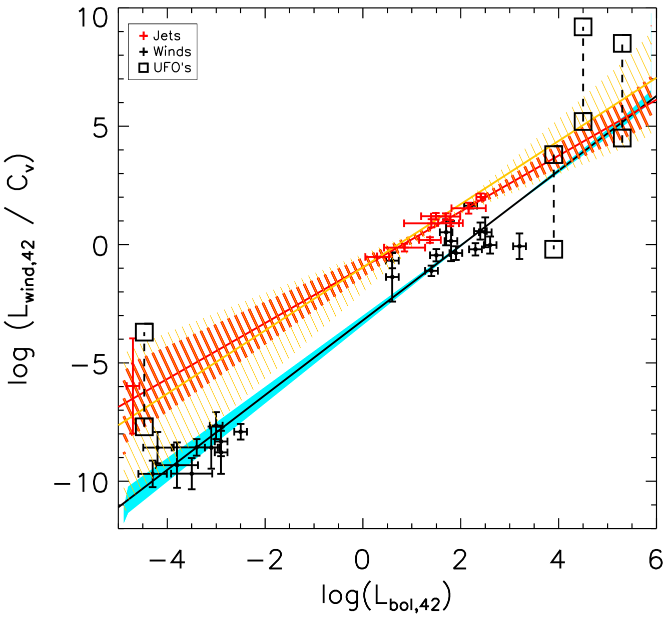

Figure 4.6 This plot is the same as Figure 4.4 but now includes UFO's in black squares ($v > 0.1c$). The upper square is the power estimate with a filling factor of unity. The bottom square connected by the dashed line is the lower estimate of the wind power if the filling factor is as low as $C_v = 10^{-4}$. Even with a smaller filling factor, the UFO's resemble the jet relation more so then the wind relation. Perhaps this is indicated that the winds are reaching a phase where they are being accelerated into jets.

potential transient nature (*Tombesi et al.*, 2011) as well as density diagnostics (*King et al.*, 2012a). We note that variability of these sources can be attributed to both movement across our line-of-sight as well as duty cycle. However, the timescales for variability are short compared to dissipative timescales, and are generally ascribed to filling factor and not duty cycle (e.g., *Elvis et al.*, 2004; *Crenshaw and Kraemer*, 2012; *Risaliti et al.*, 2009). Regardless of the filling factor, these high velocity outflows tend to be much more efficient at their given bolometric luminosity as compared to the other winds. Therefore the ultra-fast outflows may resemble the jet relation, which is plotted in Figure 4.6. As the ultra-fast outflow power approaches that of jets, it suggests that we are seeing the transition from winds as they are being accelerated into jets.

4.5.5 Distance and Mass Dependence Diagnostics

When examining broad relationships, it is important to be wary of a rising trend with a slope of unity; this can indicate that a relation that is driven by a mutual dependence of a third, shared parameter. For example, in the wind relation, both the bolometric and ionizing luminosity are both proportional to the square of the distance, which may have an influence in driving the observed trend. However, we find evidence to the contrary. Not only is the observed slope in the wind relation is greater than unity, but a partial correlation test, described by *Akritas and Siebert* (1996), gives a low probability of $p = 0.035$ that the wind relation is driven by a mutual dependence on distance. This estimate is derived from Kendall's partial $\tau_{K,p}$, which gives the Kendall's τ holding the third parameter, distance, constant. The values we find for the wind relation are $\tau_{K,p} = 0.270$, with an estimated variance, $\sigma_K = 0.128$. Further, the rising trend in the winds is therefore dominated by the velocity and ionization as $L_{\text{wind}} \propto v^3/\xi$, both of which are directly and independently constrained by observations. We also note that the jet sample is not driven by distance. This sample has an even smaller probability of $p < 10^{-6}$ that distance is needed as a third parameter. This is derived from a Kendall's partial correlation test where $\tau_{K,p}$=0.86 and σ_K=0.13.

Similarly, we tested whether the relations are driven by the mass of the black hole. A partial correlation test of the wind sample using mass as a third variable gives a probability of $p = 0.034$ that the relation is driven by a mutual dependence on mass. This probability was derived from a Kendall's partial correlation test where we found $\tau_{K,p}$ is 0.436 with $\sigma_K = 0.206$. The jet sample is even less dependent on mass with a probability of $p = 1.8 \times 10^{-3}$ ($\tau_{K,p} = 0.73$ and $\sigma_K = 0.24$), likely the result of the sample including only 1 BHB and massive ellipticals ($M \sim 10^9 M_{BH}$).

Although the probability in the wind sample is small, it does not rule mass out as a third parameter at a 3σ level like the jet sample does. The nature of these winds

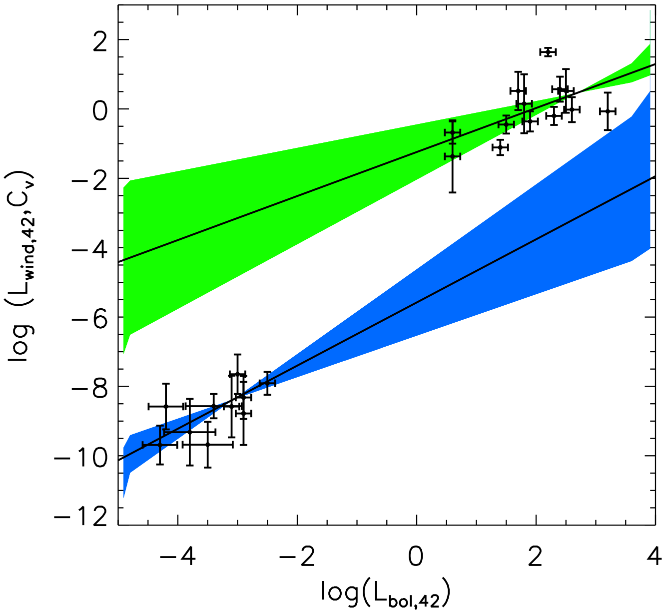

Figure 4.7 This figure shows the best fit linear regressions when the AGN and BHB samples are fit separately. The BHB are described by $\log(L^{\rm BHB}_{\rm wind,42}) = (0.91 \pm 0.31)\log(L^{\rm BHB}_{\rm Bol,42}) - (5.58 \pm 1.68)$ with scatter consistent with zero. The AGN are described by $\log(L^{\rm AGN}_{\rm wind,42}) = (0.63 \pm 0.30)\log(L^{\rm AGN}_{\rm Bol,42}) - (1.24 \pm 0.63)$ with scatter $\sigma_0^{\rm AGN} = 0.58$.

across such a large mass scale has not been studied before. Consequently, we explore the potential for mass dependence in this data set.

We separately fit a linear relation to both the BHB and AGN data sets. We used the same linear regression as in Sections 4.5.1 & 4.5.2, minimizing the χ^2 for the best fit parameters. We find the BHB sample had the best fit parameters of $\alpha^{\rm BHB} = 0.91 \pm 0.31$, $\beta^{\rm BHB} = -(5.58 \pm 1.68)$ and an intrinsic scatter consistent with zero ($\sigma_0^{\rm BHB}$=0). The AGN sample had the best fit parameters of $\alpha^{\rm AGN} = 0.63 \pm 0.30$ and $\beta^{\rm AGN} = -(1.24 \pm 0.63)$ with an intrinsic scatter of $\sigma_0^{\rm AGN} = 0.58$. Figure 4.7 depicts the best fit relation for the BHB and AGN, and Table 4.3 lists these parameters for comparison with previous results.

The slopes of the two individual fits are consistent with each other, although inconsistent with the initial fit to the wind sample at the 2.4σ and 3.1σ level for the

BHB and AGN samples, respectively. However, in order to evaluate whether these parameters are truly inconsistent with the initial fit, we used a bootstrap method to resample the data and estimate the number of trials we would expect with slope $\alpha \geq 1.58$. Using N=10^4 trials, we found that in the BHB sample, 3.1% of the trials gave a slope $\alpha \geq 1.58$. Similarly, in the AGN sample, 1.7% of the trials gave a slope $\alpha \geq 1.58$. Although these parameters are formally inconsistent with the initial fit using the 1 σ error bars, we can not rule them out at more than a 98.3% confidence level. In addition, by fitting the data separately, we are introducing an additional three free parameters and thereby doubling the parameter space. Because we can not directly compare the $\Delta\chi^2$, as the χ^2/ν is fit to be unity, we used a Bayesian analysis to determine which model better describes the data.

The advantage to using Bayesian statistics is that it allows us to compare two different models of the same data without a reduced χ^2 and without the same number of degrees of freedom. This is done via a Bayesian odds ratio, which compares the likelihood of each model over the entire parameter space. In our analysis, we assume a uniform prior distribution in slope ($\alpha \in [-10, 10]$), intercept ($\beta \in [-12, 2]$), and scatter ($\sigma_0 \in [0, 3]$). We find that when comparing the likelihood of the single fit, $\mathcal{L}_1$, to the two individual linear fits, $\mathcal{L}_2$, the odds ratio was $\mathcal{O}_{1,2} = \frac{\mathcal{L}_1}{\mathcal{L}_2} = 0.17$. This means that the two linear fits are slightly favored over the single linear fit, suggesting that mass may have a role in this relation. In Section 4.6.3 we suggest further observations that would also help to distinguish between the two models.

We next fit a plane to the data, which included mass as an additional parameter. A similar linear regression to that used in Section 4.5.1, is used to fit a plane to the entire wind data set. The plane is described by,

$$Z = \alpha_p X + \beta_p Y + \gamma_p \tag{4.9}$$

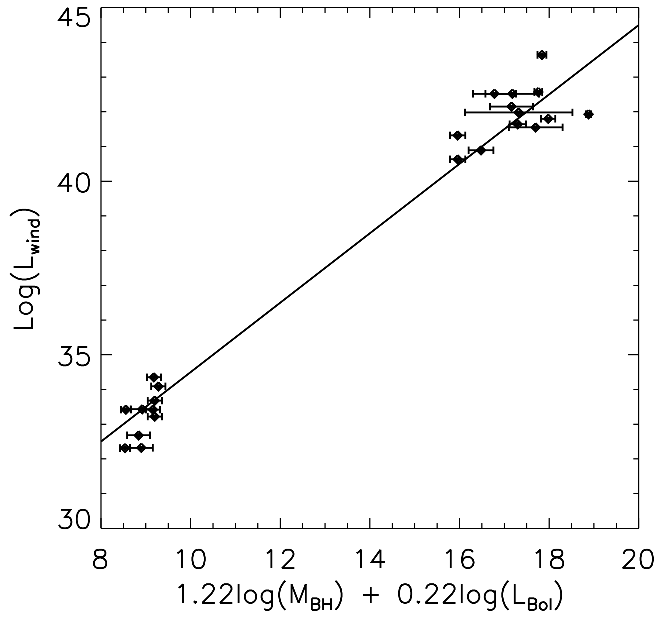

Figure 4.8 The above plot shows the best fit plane of our wind sample when including mass as a third parameter with bolometric luminosity and wind power. The plane is described by $\log(L_{\mathrm{wind}}) = (1.2 \pm 0.3)\log(\mathrm{M_{BH}}) + (0.2 \pm 0.4)\log(\mathrm{L_{Bol}}) + (24.5 \pm 0.2)$ with scatter $\sigma_0 = 0.68$.

where $X = \log(L_{\mathrm{Bol}})$, $Y = \log(M_{\mathrm{BH}})$, $Z = \log(L_{\mathrm{wind}}/C_v)$, and γ_p is the intercept. In order to find the best fit parameters, we minimized the function,

$$\chi^2 \equiv \sum_{i=1}^{N} \frac{(Z_i - \gamma_p - \beta_p Y_i - \alpha_p X_i)^2}{\alpha_p^2 \sigma_{X,i}^2 + \beta_p^2 \sigma_{Y,i}^2 + \sigma_{p,0}^2} \tag{4.10}$$

where $\sigma_{X,i}$ is the $\log(L_{\mathrm{Bol}})$ scatter, $\sigma_{Y,i}$ is the $\log(M_{\mathrm{BH}})$ scatter, and $\sigma_{p,0}$ is the intrinsic scatter of the plane in the Z direction. This is further discussed in *Merloni et al.* (2003) and *Gültekin et al.* (2009a)

We found the data set is best fit by the parameters are $\alpha_p = 0.2 \pm 0.4$, $\beta_p = 1.2 \pm 0.3$ and $\gamma_p = 24.5 \pm 0.2$ with an intrinsic scatter of $\sigma_{p,0} = 0.68$. Figure 4.8 shows the best fit plane.

Ideally, we would like to compare this plane to a plane that describes the jet cavities while including mass. However, the jet cavities are dominated by ellipitical galaxies with masses of approximately $M_{BH} \approx 10^9 M_\odot$, and as demonstrated by the partial correlation test, the data show a relation that is independent of mass at the 99.82% confidence level. Although mass may be an important variable, the data may not span a wide enough parameter space to deduce its effects. However, previous studies that have used radio luminosity instead of X-ray cavities to study jet characteristics, have shown a mass dependence (e.g., *Merloni et al.*, 2003; *Falcke et al.*, 2004a; *Gültekin et al.*, 2009a). As we noted in Section 4.3.4, using radio luminosity to study jet properties involves some uncertainties when converting between radio flux density to jet power (e.g. *Merloni and Heinz*, 2007), and should be treated with caution.

Therefore, we proceed with only a tentative comparison of our relation to the fundamental plane of accretion onto black holes. The wind plane parameters, α and β, are formally consistent with the fundamental plane parameters given by *Gültekin et al.* (2009a), although the overall normalizations differ. See Figure 4.9. The plane given by *Gültekin et al.* (2009a) relates the accretion rate of low-luminosity black holes via the X-ray luminosity and the mass of the central black hole to the radio luminosity of the compact radio source in the host galaxy. We note that we do not include a conversion between radio luminosity and jet power in this comparison, which may be necessary for comparison with our wind sample. In addition, the work by *Gültekin et al.* (2009a) uses X-ray luminosity and does not include the bolometric correction factors that we have used in our work. Both of these caveats should be examined in the future to better understand the connection and consistency between these two relations. Finally, we note that our wind coefficient describing the bolometric luminosity, α_p, is consistent with the coefficient given by *Merloni et al.* (2003), and our mass coefficient, β_p, is only inconsistent with the *Merloni et al.* (2003) coefficient at the 1.3 σ level. Again, *Merloni et al.* (2003) describe a similar plane between the mass, X-ray luminosity and compact radio emission in both stellar- and supermassive

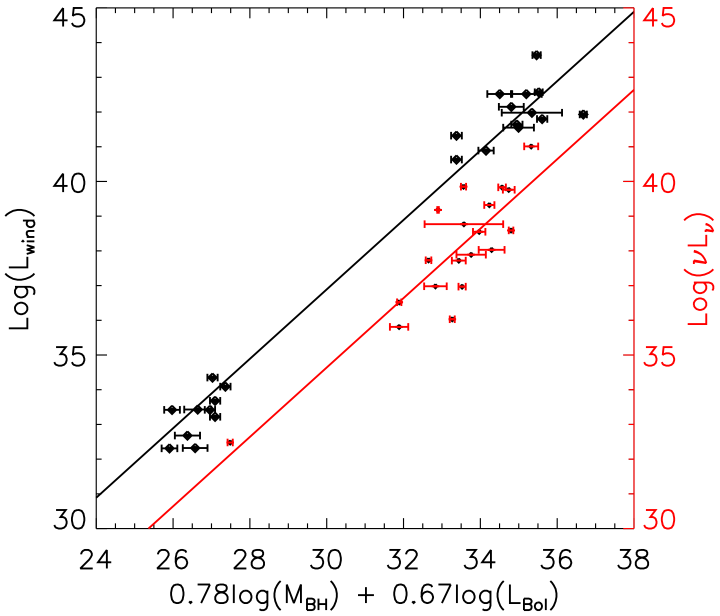

Figure 4.9 This plot shows our wind data plotted against the fundamental plane of black hole activity described by *Gültekin et al.* (2009a). The solid line is used to show the one-to-one correspondence in this plane cross section. ν=5GHz. Although the intercepts are different, the coefficients of mass and X-ray/Bolometric luminosity are consistent between our sample and *Gültekin et al.* (2009a), which may tentatively suggest a common driving mechanism.

black holes.

4.6 Discussion

We have compiled samples of both X-ray winds and relativistic radio jets that span eight orders of magnitude in black hole mass. Each sample has uniform, rigorous selection criteria to ensure consistent comparisons between the various sources. In particular, we demand that the winds be detected through significantly blue-shifted absorption features seen in the X-ray band, and the jets be seen as X-ray bubbles or cavities. By including only the X-ray winds and jets, we aim to probe the outflows associated with the inner accretion disk. These flows may be driven by the accretion disk, and jetted outflows may also tap the spin of the black holes.

For comparison, we also examine the bolometric or Bondi luminosity of each source. In doing so, we find a relation that describes the entire black hole X-ray winds sample as $\log(L_{\rm wind,42}/C_v) = (1.58 \pm 0.07)\log(L_{\rm Bol,42}) - (3.19 \pm 0.19)$ and jet sample as $\log(L_{\rm Jet,42}) = (1.18 \pm 0.24)\log(L_{\rm Bondi,42}) - (0.96 \pm 0.43)$. If we exclude Cygnus X-1 the relation becomes $\log(L_{\rm Jet,42}) = (1.34 \pm 0.50)\log(L_{\rm Bondi,42}) - (0.80 \pm 0.82)$. These relations suggest a common regulation scheme for winds and jets across the mass scale. We also find that when fit individually, the BHB and AGN wind samples have shallower slopes of $\alpha^{BHB} = 0.91 \pm 0.31$ and $\alpha^{AGN} = 0.63 \pm 0.30$, which are also consistent with each other within errors. Although, the two wind fits are preferred slightly over the entire sample fit, a *common* slope between the BHB and AGN is required by the data regardless of the procedure used.

4.6.1 Plausible Outflow Driving Mechanisms

Examining winds specifically, thermal, radiative and magnetic mechanisms are viable methods of driving winds. However, it is not clear that these mechanisms would *collectively* drive this relation in the same way as required by the data. We now turn to whether radiative, thermal or magnetic processes can drive the observed X-ray wind correlation individually.

First we examine whether radiation pressure, and more specifically UV line driving, has enough force to launch winds. If we assume this occurs when the force from the lines, F_{lines}, exceeds that of gravity, F_{grav}, i.e. $F_{lines} > F_{grav}$, it yields the following UV luminosity, L_{UV}, criterion that $L_{UV}\mathcal{M}(t) > L_{\rm Edd}$ (See equation 8 in *Proga and Kallman*, 2002). Here $\mathcal{M}(t)$ is the force multiplier (*Castor et al.*, 1975), and $L_{\rm Edd}$ is the Eddington luminosity. The force multiplier allows us to quantify the contribution of line driving in addition to electron scattering and is a function of the optical depth $t = \sigma_T \rho v_{th} \left|\frac{dv}{dr}\right|^{-1}$, ρ is the density, v_{th} is the thermal velocity and $\left|\frac{dv}{dr}\right|$ is the velocity gradient along the flow (*Castor et al.*, 1975). For most BHB, the strong X-ray radiation can highly ionize the gas, driving the $\mathcal{M}(t)$ to 1 at $\log \xi \approx 2$, and $\mathcal{M}(t)$ to 0.1 at $\log \xi \approx 3$ (*Proga et al.*, 2000). In addition, the BHB spectrum does not have a large relative contribution from the UV, due to the high disk temperatures. This also hinders line-driving of winds consistent with *Proga and Kallman* (2002); *Proga* (2002). On the other hand, AGN spectra peak in the UV, and the AGN winds span a wider range of ionization parameters, suggesting that at low ionization parameters, $\log \xi < 2$, line-driving may be important, which is also consistent with the work by *Proga* (2002). This may partially account for the index of 1.58±0.07 in the initial fit that makes AGN more efficient wind producers. However, it still remains to be seen what drives the higher ionization states found in a majority of the AGN listed here.

Thermal pressure is another plausible driving mechanism. Winds can be driven by thermal pressure if the temperature of the gas is higher than the local escape speed (e.g., *Begelman et al.*, 1983; *Woods et al.*, 1996). It has been shown that thermal winds arise at 0.1–0.2 R_C, the Compton radius. R_C is defined to be $R_C \simeq 10^{10}(M/M_\odot)T_{C8}^{-1}$ cm, where T_{C8} is the Compton temperature in terms of 10^8 K (*Woods et al.*, 1996). Therefore, to launch a thermally driven wind, we require the launching radius, $R_{\rm launch}$, be located at greater than 0.1 R_C. If we then assume that the observed velocity is equal to the local escape velocity, we can solve for the corresponding radius,

$$R'_{\rm launch} \simeq \frac{2GM}{v_{\rm out}^2} \tag{4.11}$$

$$=10^{11}\left(\frac{M}{M_\odot}\right)\left(\frac{v_{\rm out}}{300 km\ s^{-1}}\right)^{-2} cm. \tag{4.12}$$

Setting this radius to be greater than or equal to the launching radius, which is required if the wind is to be thermally driven, we find,

$$R'_{\rm launch} \gtrsim R_{\rm launch} \tag{4.13}$$

$$10\left(\frac{M}{M_\odot}\right)\left(\frac{v_{\rm out}}{300km\ s^{-1}}\right)^{-2} > 0.1\left(\frac{M}{M_\odot}\right)\frac{1}{T_{C8}} \tag{4.14}$$

$$T_{C8} > 10^{-2}\left(\frac{v_{\rm out}}{300km\ s^{-1}}\right)^{2}. \tag{4.15}$$

We can see here that for typical velocities, and low Compton temperature ($< 10^6$ K), driving winds by thermal pressure is difficult. We note that the actual velocity is likely to be greater than the line-of-sight velocity due to inclination effects and transverse velocities across our line-of-sight. If the observed velocity is proportional to the gravitational potential. i.e., $v_{\rm out}^2 \gtrsim GM/R_{\rm launch}$, then a higher velocity would place the gas deeper in the potential well and thus increase the temperature needed to launch a thermally driven wind. In addition, we have assumed that the launching radius is the radius at which the observed velocity equals the escape velocity.

Requiring that the velocity exceeds the escape velocity also requires that the bolometric luminosity to be

$$L_{\rm Bol} \gtrsim (6.4)^{-3/4}(R/R_C)^{-1/2}L_{CR} \tag{4.16}$$

where L_{CR} is the critical luminosity defined as $L_{CR} = 2.88 \times 10^{-2}T_{C8}^{-1/2}L_{\rm Edd}$. (See *Proga et al.*, 2000, for more details.) If the source luminosity is $L_{\rm Bol} \lesssim 2 \times 10^{-2}L_{\rm Edd}$ then it would fail to launch an escaping wind. As seen in Figure 4.5, a majority of the wind sources are above this threshold, so thermal driving is plausible as long as our assumption about the launching radius is correct. If the wind originates closer than $0.1R_C$, then other mechanisms are needed.

Luketic et al. (2010) perform hydrodynamical simulations to explore whether thermal driving could be responsible for the winds seen in X-ray binaries. They conclude that at low densities, thermal driving is possible from an X-ray heated accretion disk. However, at densities higher than $n_e > 10^{12}$ cm^{-3}, Compton heating is not sufficient at driving winds at velocities of $v_{\rm out} \geq 10^2$ km s^{-1}. *Luketic et al.* (2010) compare their work to observations of GRO J1655-40 which has a high density of $n_e \simeq 10^{14}$ cm^{-3} (*Miller et al.*, 2008), and conclude that thermal driving is not responsible for its winds. It is possible that the other X-ray binaries have similar densities, and as Figure 4.1 shows, they have similar velocities as well as high ionizations. Therefore, Compton heating may be an unlikely driving source for these X-ray binaries.

The AGN in Figure 4.1 show a much wider range in ionization but are all outflowing at velocities consistent with $v_{\rm out} > 10^2$ km s^{-1}. If they share a similar density to that of the BHB, then Compton heating is not a viable driving mechanism for them either. *Dorodnitsyn et al.* (2008) also perform hydrodynamical simulations for Compton heated and radiation driven AGN winds. They find similar outflowing velocity and ionization parameters as we show in Figure 4.1 but the density they assume is far lower than what is inferred from observations (e.g., *McKernan et al.*, 2007; *Risaliti et al.*, 2009; *King et al.*, 2012a). In addition, the location of their warm-absorbers are much farther from the central source than those inferred from observations (e.g., *King et al.*, 2012a; *Crenshaw and Kraemer*, 2012).

A third driving mechanism can be magnetic fields, whether through magneto-centrifugal force (*Blandford and Payne*, 1982), or magnetic pressure from the toroidal field generated by MRI in the disk, as suggested by *Contopoulos* (1995), *Miller and Stone* (2000), and *Proga* (2003). These winds tap magnetic field energy generated or sustained in the disk. It has been shown that for at least three of the sources included in our study, GRO 1655-40, NGC 4051, and NGC 4151, magnetic processes are likely driving the observed winds (*Kraemer et al.*, 2005; *Miller et al.*, 2008; *King et al.*, 2012a; *Neilsen and Homan*, 2012). Because these sources (the BHB, GRO 1655-40, and Seyfert-1's, NGC 4051 and NGC 4151) are included in this relation, and span orders of magnitude in mass, it raises the possibility that magnetic forces may drive this wind relation.

Jets are also thought to be driven by magnetic processes in the disk or near the black hole (e.g., *Lovelace*, 1976; *Blandford and Payne*, 1982; *Blandford and Znajek*, 1977; *Krolik and Hawley*, 2010). The jet power relation is determined to be $\log(L_{\mathrm{Jet},42}) = (1.18 \pm 0.24)\log(L_{\mathrm{Bol},42}) - (0.96 \pm 0.43)$. If we exclude Cygnus X-1, then the jet relation becomes $\log(L_{\mathrm{Jet},42}) = (1.34 \pm 0.50)\log(L_{\mathrm{Bol},42}) - (0.80 \pm 0.82)$ (See Figure 4.4). When we include Cygnus X-1 in the jet relation the slope of the jet relation and the initial wind relation are inconsistent at the 1.6σ level. When we exclude Cygnus X-1, the jet relation slope is formally consistent with that of the single wind relation. Further, if we examine the individual wind fits, the jet relation including or excluding Cygnus X-1 is consistent with the BHB slope. When comparing the jet relation to the AGN sample, the slopes are only inconsistent at the 1.4σ and 1.2σ level, including and excluding Cygnus X-1, respectively. Finally, we very tentatively suggest that the plane fit to the wind sample is consistent with the fundamental plane of accretion onto black holes (*Gültekin et al.*, 2009a), which would be further evidence of the similar dependence on mass accretion rate (as well as mass) of both the winds and jets.

If the two types of outflows are regulated by the mass accretion rate in the same fashion, then the same driving mechanism may also be at work, as the geometry or mass loading of the magnetic fields may be driven by the mass accretion rate as well. This may explain the formal consistency of the slopes between the jet and wind relations. A *Blandford and Payne* (1982) scenario may be a viable solution for driving these outflows, and could be possibly aided by *Blandford and Znajek* (1977) scenario for jets. In addition, *Ohsuga and Mineshige* (2011) show that MHD accretion flows can drive both jets and winds depending on the mass accretion rate, qualitatively consistent with Figure 4.5.

The ultra-fast outflows appear to follow the jet relation (See Figure 4.6). These are winds whose observed velocity exceeds $v > 0.01c$. This raises the question of how these ultra-fast winds are accelerated to such high velocities. Are we seeing the phase at which these winds are being collimated into jets, as the power associated with the winds is very comparable to the jet power? Again, this could point to a shared driving mechanism between winds and jets, such as MHD (*Lovelace*, 1976; *Blandford and Payne*, 1982), if we are truly observing this transition phase between the two.

4.6.2 Implications for Feedback

The characterization of these outflows allows us to determine that X-ray AGN winds are more efficient at removing material than are X-ray BHB winds. Interestingly, *Hopkins and Elvis* (2010) show that only 0.5% of the bolometric luminosity needs to be converted into mechanical power in order to regulate black hole growth and affect feedback in the host galaxy. As shown in Figure 4.10, the majority of the AGN lie above (or are consistent with) $5 \times 10^{-3} L_{\mathrm{Bol}}$. A few sources lie above $5 \times 10^{-2} L_{\mathrm{Bol}}$ (the dotted line). *Crenshaw and Kraemer* (2012), in a study focusing only on AGN winds, show that up to half of their AGN are consistent with $\gtrsim 5 \times 10^{-3} L_{\mathrm{Bol}}$. However, if the filling factor is much less than unity, the wind power will be far less than the $5 \times 10^{-3} L_{\mathrm{Bol}}$ limit for influential feedback. This may imply that the X-ray winds do not have a large impact on feedback.

In addition, Figure 4.2 shows a stratification of the kinetic wind luminosity as a function of ionization in the AGN. The low ionization components ($\log \xi < 2$) tend to have a much higher kinetic luminosity as compared to the medium ionization components ($2 < \log \xi < 3$) and high ionization components ($3 < \log \xi$). The reason for this may again be because the filling factor is not included in this analysis. As mentioned in Section 4.4, these black hole X-ray winds are thought to be clumpy and filamentary. Moreover, observations of ionized stellar winds indicate that the less

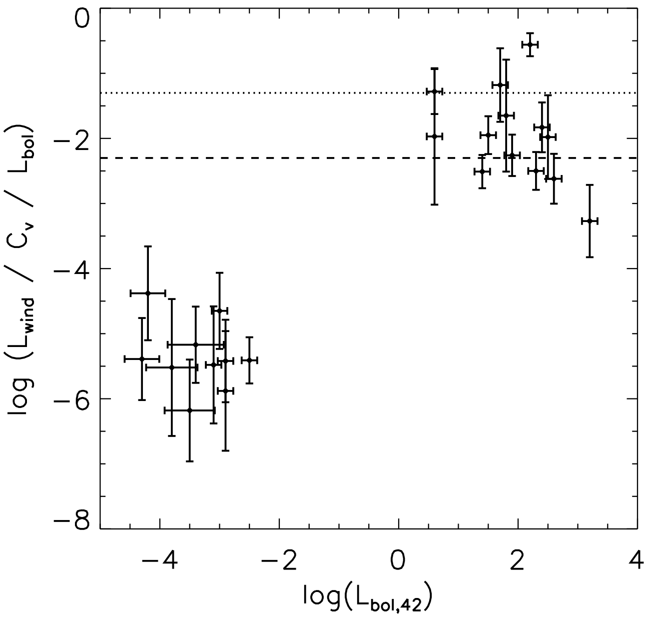

Figure 4.10 This plot shows the correlation between kinetic wind luminosity per filling factor divided by the bolometric luminosity as compared to the bolometric luminosity. The dotted line is 5% L_{Bol}, while the dashed line is 0.5% L_{Bol}. These are the limits of the kinetic wind power reported by *Di Matteo et al.* (2005) and *Hopkins and Elvis* (2010), respectively, for mechanical feedback to have an influence on black hole growth and feedback. We expect these winds to have a small filling factor which would make the wind power estimate lower, and perhaps below 0.5% L_{Bol}.

ionized gas should be more clumpy, i.e. have a lower filling factor, due to pressure confinement from the hot surrounding gas (e.g., *Sako et al.*, 1999). This would imply that the low ionization components seen in Figure 4.2 would likely have a lower filling factor than the high ionization components. If the filling factors were included, the low ionization components would no longer rise above the higher ionization components. This would serve to flatten the initial wind relation, making the wind slope even more consistent with the jet relation slope. Feedback from the lowest ionization components would no longer dominate the relation.

On the other hand, the low ionization components may also be consistent with being radiatively driven, and therefore would not follow the same relation as the high ionization components anyway. As shown in Section 4.5.1, the high ionization components do follow a shallower slope of $\alpha^{\log\xi>2} = 1.42 \pm 0.06$, which is consistent with both jet relations, i.e. including and excluding Cygnus X-1.

Regardless of the ionization of the winds, jets are more efficient at a given bolometric luminosity, compared to X-ray winds. When considering power alone, jets may have a greater impact on mechanical feedback and galaxy evolution then winds. Depending on the mass accretion rate, for which we use the bolometric or Bondi luminosity as a proxy, we can now characterize the associated jet and wind power. Figure 4.5 shows exactly how the outflow power scales with Eddington fraction. There is a division between dominant outflow at approximately $10^{-2}L_{\rm Edd}$. If both the winds and jets share a common launching mechanism, this division may be strongly driven by the mass accretion rate. Mass loading or even the geometry of the magnetic fields in the disk would have an important role as well, and can again be directly regulated by the mass accretion rate. The transition seen at approximately $10^{-2}L_{\rm Edd}$ is also interesting because this is the regime where winds begin to prevail over jet production, especially seen the spectral state dependence in X-ray binaries.

We can now describe the outflow power as a function of Eddington fraction directly associated with the inner-accretion disk surrounding a black hole, vital for cosmic simulations. This is important because as Figure 4.5 demonstrates, outflows are present in a range of Eddington fractions, not just low Eddington fractions. As galaxies evolve through their “Quasar” and “radio” modes of accretion, we are still able to prescribe the outflowing power to assess the mechanical feedback in those systems and explore the implications for galactic co-evolution.

4.6.3 Potential Caveats

Before using these descriptions, it is important to understand the caveats involved in assembling this data set. As shown in Figure 4.5, there is a potential state dependence of outflow type on accretion rate (also see *Miller et al.*, 2006a, 2008; *Neilsen and Lee*, 2009; *Ponti et al.*, 2012). However, it is not clear if this is a result of a selection bias toward high luminosity AGN. One could imagine that at low X-ray luminosity, i.e. ellipticals and BHB in the “low/hard” state, detections of winds could be hampered by low signal-to-noise. This would be most pertinent to our jet sample, which is dominated by low luminosity AGN accreting at low accretion rates. However, even if winds were to coexist in these low accretion rates, just as they do in Seyfert 1 NGC 4051 (*King et al.*, 2011), jet power is likely to dominate by orders of magnitude, as the wind power is proportional to the ionizing luminosity, which would be small. In addition, in BHB strong limits to wind detection have been made in the “low/hard” state (e.g., *Neilsen and Lee*, 2009) as well as strong upper limits to jet production in the “high/soft” state (e.g., *King et al.*, 2012b). Therefore, we stress that this work is focused on the dominant outflow.

We also note the difficulty in placing upper limits on wind detections using absorption features in the X-ray band. As these features can be seen at an array of different velocities and ionization states, there is no specific wavelength one would expect to find an absorption feature denoting an outflow. Further, the wind power estimates do not depend on the strength of the line, but only the wavelength and ionization state, making estimates of upper limits rather difficult. These issues of detection affect both BHB and AGN in the same manner, and we stress that the lack of detection of these absorption features is not evidence for the absence of a wind, but may be the absence of evidence. Again, the state dependence of outflows seen in BHB and now in AGN (Figure 4.5) is likely to be driven by accretion rate. However, longer integrations to improve signal-to-noise of BHB in the "low/hard" state and AGN at low accretion rates are needed to be confident of this assessment (e.g., *Miller et al.*, 2012). Next, we note that there are outflows other than the ones examined in our analysis that are still important in removing substantial amounts of material from their accretion disks and host galaxies. In particular, broad absorption line (BAL) quasars have particularly powerful outflows (*Moe et al.*, 2009; *Dunn et al.*, 2010; *Brandt et al.*, 2000). However, these outflows are observed in the optical and ultra-violet regime and have much lower ionization parameters than the X-ray winds discussed here. Therefore, they are not as readily associated with - or driven by - the inner accretion disk, and have not been included in our analysis. *Crenshaw and Kraemer* (2012) also show a positive correlation between ionization parameter, U, and column density in local AGN in their figure 3. This demonstrates that the bulk of the outflow material is being observed in the X-ray regime.

A broader range of ionization parameters are probed in the AGN as compared to the BHB (See Figure 4.1), which may also contribute to the AGN scatter. The mix of ξ in AGN calls into question whether we are probing the same physics, i.e. closest to the black holes. Because ionization is dependent on the distance as $\xi = L(nr^2)^{-1}$, similar ionization states should probe the same distance from the black hole for a given luminosity. Consequently, similar micro-physics at a given radius and ionization should be at work. Further, in Section 4.6.2, examining the high ionization components alone results in a shallower slope when comparing bolometric luminosity to wind power. A shallower relation is more consistent with the jet relation. This demonstrates the clear need for a much larger sample size. Fortunately, *Astro-H* will provide the needed coverage in the highest ionization band. This will not only allow for the detection of additional sources, but also detection of the highest ionization states for comparison with stellar-mass black holes.

Although we see a large range in ionization, we do not see as large of a range in velocity. It is only when we include the ultra-fast outflows that three orders of magnitude in velocity are probed as compared to the six orders of magnitude in the ionization parameter. This trend is important in understanding whether inclination has an effect on the given L_{wind} vs L_{Bol} correlation. As BHB winds are thought to be observed in nearly edge-on sources (e.g. *Miller et al.*, 2006a,b; *Ponti et al.*, 2012), and AGN winds, especially Seyfert 1 AGN winds, are thought to be observed in face-on sources (e.g., *Wu and Han*, 2001), inclination could have the potential to bias our results. However, the data show no trend in velocity as a function of inclination. In addition, when examining BHB sources individually, face-on sources (e.g., GX 339–4, XTE J1817–330) do not show absorption features in the Fe K band when they are in the "high/soft" state, contrary to their edge-on counterparts. This is due to limited sensitivity, since low inclination sources tend to be softer and to give less signal through the Fe K band. As noted in *Ponti et al.* (2012), the limits on flux in face-on sources are not very constraining, and lines as weak as those in H1743-322 (*Miller et al.*, 2006b) could not have detected in e.g. XTE J1817-330. For instance, there is likely a simple absence of evidence for BHB winds in face-on systems.

One may also expect inclination to have an effect on the estimated kinetic jet power. For example, those sources for which the jet is directed along our line of sight may suffer from Doppler boosting. However, this would primarily affect the radio luminosity of such sources, and not the kinetic power, which is taken from estimates of cavity sizes. On the other hand, the jet power may be influenced by the spin of the black hole. If jets are driven by the *Blandford and Znajek* (1977) mechanism, then spin may play a large role in the power released by the jets. However, the common slopes between the jet and wind relation points to more of a *Blandford and Payne* (1982) scenario, where the spin of the black hole does not affect the power released. Further, the fact that the jet and wind power seem to be present at certain Eddington fractions, point to the idea that mass accretion rate may be the throttle that is ultimately driving the type and power of the outflow. We note that spin is unlikely to play a large role in the X-ray wind power regardless, as winds are thought to originate further out in the accretion disk.

An additional concern with the jet power is that the estimate is a long-term average and not instantaneous as are the wind power estimates. If the jet production occurs on timescales that are much shorter than the dynamical timescale of the cavity, than the power estimates would increase. Unfortunately, this is a limit of this technique when using cavities to estimate power. However, long term estimates of power are more pertinent for feedback estimates.

Finally, as this sample is small in size, the results must be regarded cautiously and tested in the future. It is imperative that we obtain more observations at all masses and mass accretion rates. Specifically, black holes accreting at $L_{Bol} \sim 10^{41} - 10^{42}$ ergs s^{-1} could distinguish whether one linear fit is required across the entire wind sample or if the BHB and AGN are better fit by individual linear fits. This could either be a small Seyfert galaxy with mass on order of $M \sim 10^5 M_\odot$ accreting at a few percent of Eddington, or a large SMBH, $M \sim 10^9 M_\odot$, accreting at a very low Eddington rate. In addition, non-simultaneity of AGN luminosities could have a dramatic effect on the observed scatter seen in the X-ray winds. Although the AGN timescales for disk evolution are longer than BHB, observations made years apart may not probe the same accretion regime.

4.7 Conclusions

- In this study, we find that winds are consistent with being regulated according to a simple relation across a large mass scale. In particular, we find the trend is described as $\log L_{\mathrm{wind},42} \propto (1.58 \pm 0.07) \log L_{\mathrm{Bol},42}$. The slope is greater than unity, so it may imply that the SMBH are more efficient at expelling material than BHBs.

- If we fit the BHB and AGN populations separately, they still require consistent slopes of $\alpha^{BHB} = 0.91 \pm 0.31$ and $\alpha^{AGN} = 0.63 \pm 0.30$. Further, if we assume mass is influencing this relation and fit a plane to the data, we find the best fit relation to be $\log(L_{\mathrm{wind}}) = (1.2 \pm 0.3) \log(\mathrm{M}_{\mathrm{BH}}) + (0.2 \pm 0.4) \log(\mathrm{L}_{\mathrm{Bol}}) + (24.5 \pm 0.2)$ with scatter $\sigma_0 = 0.68$ consistent with the "fundamental plane" of accretion onto black holes.

- It remains possible that different processes tied to the mass accretion rate-thermal driving in stellar-mass black holes and radiative driving in AGN - are actually at work in driving winds. However, it is not clear that these different mechanisms should agree so well and follow the same slope in these wind relations. Moreover, it seems that a magnetic wind must be at work in GRO 1655−40, NGC 4051, and NGC 4151 (*Miller et al.*, 2008; *King et al.*, 2012a; *Kraemer et al.*, 2005), which fall on the relation. This may also suggest a role for magnetic driving across the mass scale.

- Furthermore, when we examine jet power, the data may be consistent with winds and jets being regulated in a common fashion. Since radiative and thermal processes are not likely to drive relativistic jets, a mechanism like magnetocentrifugal or MHD winds are plausible explanations (e.g., *Blandford and Payne*, 1982; *Proga*, 2003).

- The ultra-fast winds appear to obey the same regulation scheme as slower, more common winds, if they have a low filling factor and the slow winds have a high filling factor close to unity. However, some ultra-fast winds appear to carry as much kinetic luminosity as jets, even after accounting for filling factors. This suggests that we may be seeing a phase where winds finally are accelerated into jets.

- Figure 4.5 provides a direct way to quantify the outflow power as a function of mass accretion rate. A division between dominant outflow state is observed at approximately $10^{-2}L_{\rm Edd}$. This trend has broad implications, especially for theoretical simulations that need prescriptions for feedback to study galactic dynamics and evolution.

- A larger sample will help us to distinguish between these proposed relations as well as quantify the intrinsic scatter. As it stands now, *Chandra* will play an integral part in future studies. Looking further ahead, *Astro-H* will have improved sensitivity in the Fe K band, enabling unprecedented looks at the most ionized and innermost flows in the accretion disks of both BHB and AGN.

Acknowledgements

The authors would like to thank the anonymous referee for their invaluable comments to improve this paper. ALK acknowledges support from NASA through the NESSF program. JMM thanks NASA for support through its guest observer programs.

CHAPTER V

Conclusions

5.1 Summary

In Chapter II, I examined the disk-jet connection in the smallest known supermassive black hole with robust mass measurements, NGC 4395. Utilizing simultaneous X-ray and radio observations made over two months, I discovered that the X-ray flux had much more intrinsic variability than the radio flux densities. This held true even after the variable intrinsic neutral absorption had be modeled. Comparing the data to the fundamental plane of black hole activity, we find that the $L_X - L_R$ relation for simultaneous observations of NGC 4395 is flatter than the nominal AGN relation. When comparing the scaled luminosities of NGC 4395 to the stellar-mass black holes, we find that it lies on the transition region between the steeper $L_X - L_R$ track and the nominal $L_X - L_R$ track. This poses an interesting question as to whether all AGN follow a similar trend, where in simultaneous monitoring observations, the X-ray emission is much more variable than the radio emission causing the $L_X - L_R$ relation to always be flat; or, do AGN follow the two tracks traced out by the stellar-mass black holes? Do NGC 4395 and NGC 4051 merely happen to be in the transition between the two tracks?

In Chapter III, I discovered the fastest wind ever observed from a stellar-mass black hole. The high ionization and high velocity imply that the wind is emerging from very close to the central black hole, i.e., $\sim 1000 R_G$. Assuming typical wind densities of stellar-mass black holes, we find that the mass outflow rate rivals the mass accretion rate, which is determined via the X-ray luminosity. This wind has the highest significance of detection of either stellar-mass or AGN ultra-fast winds, and as this high velocity wind resembles those from several AGN (*Tombesi et al.*, 2013), it suggests flows are real and that ultra-fast outflows in AGN can be responsible for a substantial portion of the feedback necessary on galactic scales. Feedback from winds may be a more favorable than jets as they have a large covering fraction, and thus large interaction cross-section as compared to highly collimated jets, though the magnitude of AGN wind energetics remains to be quantified.

Finally, in Chapter IV, I examined the disk-wind-jet connection in an ensemble of black holes across the mass scale. This study was a natural extension of the work done on the fundamental plane of black hole activity. It examined the role of jet production (via radio luminosities) as a function of mass and mass accretion rate (via X-ray luminosity). I found that the wind power can be fit with a universal relation when compared to bolometric luminosity, i.e., mass accretion rate. A universal relation would imply that winds in stellar-mass and supermassive black holes have fundamentally the same (scaleable) properties, and a common regulation mechanism. Though this is a small sample, this would imply that winds are driven via magnetic mechanisms across the mass scale, and winds and jets are also driven by the same mechanism.

In all three studies, comparing outflows in one setting with their high or low mass counter parts has revealed new information, placing the outflow into a greater context. Such comparisons allow one to discover whether local plasma physics or global physical processes are driving these outflows, as stellar-mass and supermassive black holes have a wide range in mass, density and temperature. Moving forward, theories of both wind and jet production will need to explain both stellar-mass and supermassive behavior. The goal of future observers is to then put together the best ensembles of sources for like comparison across the mass scale, determining which properties are ubiquitous between outflows and which are unique to each mass extreme and type of outflow.

5.2 Open Questions

5.2.1 Radiative Efficiency

There remains a number of open questions that can be addressed in the near future. For instance, What is the radiative efficiency of jets, and is this efficiency constant with increasing jet power? The fundamental plane of black hole activity indicates that radio luminosity increases with mass and X-ray luminosity, i.e., mass accretion rate. However, the most massive and X-ray luminous sources are less efficient at producing radio emission (*Merloni et al.*, 2003; *Falcke et al.*, 2004a; *Gültekin et al.*, 2009a). Is this a result of relatively weaker jets at high Eddingotn fracitons, or are the jets just less radiative efficient at high Eddington fractions and more energy goes into kinetic energy? Figure 1.4 suggests the time averaged kinetic energy from a jet scales with radio luminosity as $\log L_K = (0.81 \pm 0.11) \log L_R + 11.9^{+4.1}_{-4.4}$ (*Merloni and Heinz*, 2007). This indicates that the jet is becoming less kinetic energy dominated and more radiatively dominated as the radio luminosity increases. Together with the fundamental plane, this indicates that jets are producing relatively less power at higher Eddington rates both radiatively and kinetically.

This needs further investigation, as it is not clear if the brightest cluster galaxies in the sample from *Merloni and Heinz* (2007) can be readily extrapolated to all the sources utilized in the fundamental plane. New upgrades to the *Karl Jansky Very Large Array* (VLA) will be able to detect more cavities, potentially surrounding "regular" AGN to confirm or deny this trend. In addition, the duty cycle of jets needs to be well determined in order to associate the time average kinetic power estimates using radio and X-ray cavities to the instantaneous radio luminosities that are observed from the jets. Finally, the radio luminosity themselves need to be better quantified as typical radio measurements are taken at 5 GHz, and the spectral energy density should depend on both mass and mass accretion rate (*Falcke et al.*, 2004a). Again the VLA will be crucial in this endeavor, as the upgraded bandpasses will allow for broad bandwidth observations quantifying the SED's.

5.2.2 Powering Jets

With respect to jets and the amount of power they produce, it still remains unclear as what is the main driving mechanism. There is a strong debate amongst the stellar-mass community as to whether the magnetic fields tap the angular momentum of the black hole to power the jet or not (e.g, *Russell et al.*, 2013; *Steiner et al.*, 2013). In the AGN community, it appears that the launching mechanism is simply assumed to tap the spin of the black hole, and this is used to explain the difference in radio-loud and radio-quiet jets (e.g., *Moderski et al.*, 1998; *McNamara et al.*, 2011). However, in detail, the spin of the black hole does not appear to be the major contributor to jet power, though may set an upper envelope to the amount of power a jet can produce (e.g., *King et al.*, 2013a).

Moving forward, studies of black hole spin in the AGN community need to be undertaken in not just Seyfert galaxies but in ellipticals and Quasars as well. Though spin measurements via iron line analysis in the X-ray band will be challenging in ellipticals, stacking efforts may prove a viable avenue of exploration. In addition, gravitationally lensed sources have proven a powerful asset in obtaining spin measurements of high redshift quasars and will expand the sample not just in type but in cosmic age as well (*Reis et al.*, 2014).

5.2.3 Structure of Winds

As high resolution observations with *Chandra* and, soon, *Astro-H* resolve more X-ray absorption features, we are able to quantify a number of different wind properties including: velocity, ionization and density. One thing that remains to be determined is the wind structure in both stellar-mass and supermassive black hole winds. Because we can only examine each source at a single inclination, it is necessary to use ensembles of wind detections from multiple sources in order to determine the structure above the accretion disk. Stellar-mass black hole winds are predominantly observed in X-ray "dipping" sources, which indicate the source is nearly edge-on, as material from the accretion disk is thought to eclipse our line-of-sight causing the "dips" in flux (*Ponti et al.*, 2012). This indicates that stellar-mass black hole winds are predominantly equatorial. In supermassive black holes, it is not as clear whether winds are strictly equatorial or have a more uniform, spherical geometry.

Future investigations need to examine exactly how wind density, column density, velocity and ionization vary with inclination in both stellar-mass and supermassive black holes. This will ultimately determine exactly what the geometry of the wind is, how much material is liberated, and with what energy is it deposited into the surrounding ISM and IGM, quantifying their feedback potentials. The geometry of the wind will also give clues to the launching and driving mechanisms that generate these winds.

5.2.4 Winds Across the Mass Scale

In determining the wind geometry, this will also answer the question as to whether winds from stellar-mass and supermassive black holes are one and the same. Chapter IV discusses evidence that supports a common regulating mechanism between stellar-mass and supermassive black holes. However, the sample of sources is small, and there is a large hole in parameter space at $\log L_X \sim 10^{41}$ ergs s^{-1} that needs to be probed

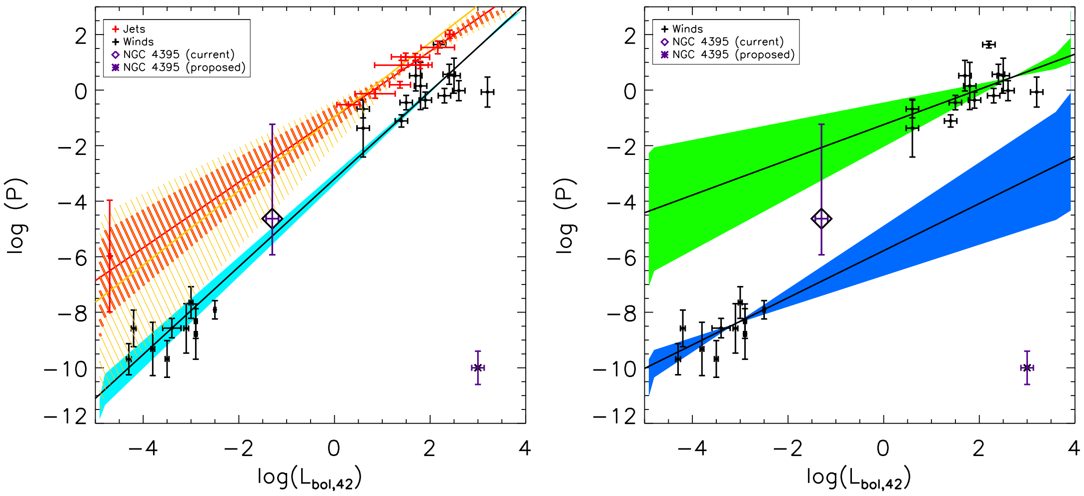

(a) (b)

Figure 5.1 *Left panel*: shows the correlation between bolometric and kinetic luminosity using a single linear relation to describe both stellar-mass and supermassive black holes for jets (red) and winds (black) respectively (*King et al.*, 2013c). *Right panel*: This figure shows the best fit linear regressions when the wind samples are fit separately *King et al.* (2013c). The purple diamond data point is the current NGC 4395 estimate, while the purple star shows our reduced error estimates using future observations. By observing a source at $L_{Bol} \approx 10^{-41}$ ergs/s, we can distinguish between these two different X-ray wind models at a 99.97% confidence.

in order to unify or separate the wind relations. Targeting a low-mass supermassive black hole that is accreting at a high Eddington fraction would probe this region of parameter space. Figure 5.1 shows the tentative winds from the supermassive black hole in the dwarf galaxy NGC 4395. Current observations have only a tentative detection, and are not constraining between either a single or dual wind relations. *Chandra* or *Astro-H* observations of NGC 4395 or another dwarf AGN will also be able to determine whether winds are generated by the same mechanisms across the mass scale. This is vital to our studies of feedback in galaxies on both local and galactic scales because it allows us to narrow down the launching and driving mechanism, constraining the disk-wind coupling.

5.2.5 Winds Versus Jets

Finally, the relationship between winds and jets has yet to be resolved. My work suggests there is a connection between winds and jets based on power output as a function of bolometric luminosity (*King et al.*, 2013c). Still, there are many unresolved questions as to whether winds and jets can coexist; do winds quench jets or vice-versa; and which type of outflow carries the most feedback. Future work will not only need to add additional sources to my sample but will need to study individual sources with great detail, employing extensive, multi-epoch, simultaneous observing campaigns. Efforts will need to target stellar-mass black holes because of their short timescales to traverse several different accretion states and outflow production. In addition, campaigns targeting AGN will need to be able to quantify the impact and efficiency how well winds and jets couple to their local environments. These studies will ultimately determine the most important role of these outflows, i.e., the co-evolution between the black hole and its host environments via the accretion driven outflows.

BIBLIOGRAPHY

BIBLIOGRAPHY

Akritas, M. G., and J. Siebert (1996), A test for partial correlation with censored astronomical data, *MNRAS*, *278*, 919–924.

Alexander, T. (2013), Improved AGN light curve analysis with the z-transformed discrete correlation function, *ArXiv e-prints*.

Allen, S. W., R. J. H. Dunn, A. C. Fabian, G. B. Taylor, and C. S. Reynolds (2006), The relation between accretion rate and jet power in X-ray luminous elliptical galaxies, *MNRAS*, *372*, 21–30, doi:10.1111/j.1365-2966.2006.10778.x.

Altamirano, D., et al. (2011a), RXTE observations strengthen the similarities between the black hole candidates IGR J17091-3624 and GRS 1915+105., *The Astronomer's Telegram*, *3299*, 1.

Altamirano, D., et al. (2011b), The faint "heartbeats" of IGR J17091-3624: an exceptional black-hole candidate, *ApJ*, submitted.

Arnaud, K., B. Dorman, and C. Gordon (1999), XSPEC: An X-ray spectral fitting package, astrophysics Source Code Library.

Asada, K., M. Nakamura, A. Doi, H. Nagai, and M. Inoue (2014), Discovery of Sub- to Superluminal Motions in the M87 Jet: An Implication of Acceleration from Sub-relativistic to Relativistic Speeds, *apjl*, *781*, L2, doi:10.1088/2041-8205/781/1/L2.

Bautista, M. A., and T. R. Kallman (2001), The XSTAR Atomic Database, *ApJS*, *134*, 139–149, doi:10.1086/320363.

Beckwith, K., J. F. Hawley, and J. H. Krolik (2008), The Influence of Magnetic Field Geometry on the Evolution of Black Hole Accretion Flows: Similar Disks, Drastically Different Jets, *ApJ*, *678*, 1180–1199, doi:10.1086/533492.

Begelman, M. C., C. F. McKee, and G. A. Shields (1983), Compton heated winds and coronae above accretion disks. I Dynamics, *ApJ*, *271*, 70–88, doi:10.1086/161178.

Blackburn, J. K. (1995), FTOOLS: A FITS Data Processing and Analysis Software Package, in *Astronomical Data Analysis Software and Systems IV*, *Astronomical Society of the Pacific Conference Series*, vol. 77, edited by R. A. Shaw, H. E. Payne, and J. J. E. Hayes, p. 367.

Blandford, R. D., and A. Konigl (1979), Relativistic jets as compact radio sources, *ApJ*, *232*, 34.

Blandford, R. D., and D. G. Payne (1982), Hydromagnetic flows from accretion discs and the production of radio jets, *MNRAS*, *199*, 883–903.

Blandford, R. D., and R. L. Znajek (1977), Electromagnetic extraction of energy from Kerr black holes, *MNRAS*, *179*, 433–456.

Blum, J. L., J. M. Miller, E. Cackett, K. Yamaoka, H. Takahashi, J. Raymond, C. S. Reynolds, and A. C. Fabian (2010), Suzaku Observations of the Black Hole H1743-322 in Outburst, *ApJ*, *713*, 1244–1248, doi:10.1088/0004-637X/713/2/1244.

Blustin, A. J., M. J. Page, S. V. Fuerst, G. Branduardi-Raymont, and C. E. Ashton (2005), The nature and origin of Seyfert warm absorbers, *A&A*, *431*, 111–125, doi:10.1051/0004-6361:20041775.

Brandt, W. N., A. Laor, and B. J. Wills (2000), On the Nature of Soft X-Ray Weak Quasi-stellar Objects, *ApJ*, *528*, 637–649, doi:10.1086/308207.

Cadolle Bel, M., et al. (2011), Overview of an extensive multi-wavelength study of GX 339-4 during the 2010 outburst, *A&A*, *534*, A119, doi:10.1051/0004-6361/201117684.

Cash, W. (1979), Parameter estimation in astronomy through application of the likelihood ratio, *ApJ*, *228*, 939–947, doi:10.1086/156922.

Castor, J. I., D. C. Abbott, and R. I. Klein (1975), Radiation-driven winds in Of stars, *ApJ*, *195*, 157–174, doi:10.1086/153315.

Cavagnolo, K. W., B. R. McNamara, P. E. J. Nulsen, C. L. Carilli, C. Jones, and L. Bîrzan (2010), A Relationship Between AGN Jet Power and Radio Power, *ApJ*, *720*, 1066–1072, doi:10.1088/0004-637X/720/2/1066.

Chartas, G., W. N. Brandt, S. C. Gallagher, and G. P. Garmire (2002), CHANDRA Detects Relativistic Broad Absorption Lines from APM 08279+5255, *ApJ*, *579*, 169–175, doi:10.1086/342744.

Chartas, G., W. N. Brandt, S. C. Gallagher, and D. Proga (2007), XMM-Newton and Chandra Spectroscopy of the Variable High-Energy Absorption of PG 1115+080: Refined Outflow Constraints, *AJ*, *133*, 1849–1860, doi:10.1086/512364.

Chiaberge, M., A. Capetti, and A. Celotti (2002), Understanding the nature of FR II optical nuclei: A new diagnostic plane for radio galaxies, *A&A*, *394*, 791–800, doi:10.1051/0004-6361:20021204.

Churazov, E., R. Sunyaev, W. Forman, and H. Böhringer (2002), Cooling flows as a calorimeter of active galactic nucleus mechanical power, *MNRAS*, *332*, 729–734, doi:10.1046/j.1365-8711.2002.05332.x.

Churazov, E., S. Sazonov, R. Sunyaev, W. Forman, C. Jones, and H. Böhringer (2005), Supermassive black holes in elliptical galaxies: switching from very bright to very dim, *MNRAS*, *363*, L91–L95, doi:10.1111/j.1745-3933.2005.00093.x.

Collier, S., et al. (2001), Multiwavelength Monitoring of the Narrow-Line Seyfert 1 Galaxy Arakelian 564. II. Ultraviolet Continuum and Emission-Line Variability, *ApJ*, *561*, 146–161, doi:10.1086/323234.

Contopoulos, J. (1995), A Simple Type of Magnetically Driven Jets: an Astrophysical Plasma Gun, *ApJ*, *450*, 616, doi:10.1086/176170.

Corbel, S., M. A. Nowak, R. P. Fender, A. K. Tzioumis, and S. Markoff (2003), Radio/X-ray correlation in the low/hard state of GX 339-4, *A&A*, *400*, 1007–1012, doi:10.1051/0004-6361:20030090.

Corbel, S., P. Kaaret, R. P. Fender, A. K. Tzioumis, J. A. Tomsick, and J. A. Orosz (2005), Discovery of X-Ray Jets in the Microquasar H1743-322, *ApJ*, *632*, 504–513, doi:10.1086/432499.

Corbel, S., M. Coriat, C. Brocksopp, A. K. Tzioumis, R. P. Fender, J. A. Tomsick, M. M. Buxton, and C. D. Bailyn (2013), The 'universal' radio/X-ray flux correlation: the case study of the black hole GX 339-4, *MNRAS*, *428*, 2500–2515, doi:10.1093/mnras/sts215.

Coriat, M., et al. (2011), Radiatively efficient accreting black holes in the hard state: the case study of H1743-322, *MNRAS*, *414*, 677–690, doi:10.1111/j.1365-2966.2011.18433.x.

Crenshaw, D. M., and S. B. Kraemer (2012), Feedback from Mass Outflows in Nearby Active Galactic Nuclei. I. Ultraviolet and X-Ray Absorbers, *ApJ*, *753*, 75, doi: 10.1088/0004-637X/753/1/75.

Crenshaw, D. M., S. B. Kraemer, and I. M. George (2003), Mass Loss from the Nuclei of Active Galaxies, *ARA&A*, *41*, 117–167, doi: 10.1146/annurev.astro.41.082801.100328.

Croton, D. J., et al. (2006), The many lives of active galactic nuclei: cooling flows, black holes and the luminosities and colours of galaxies, *MNRAS*, *365*, 11–28, doi: 10.1111/j.1365-2966.2005.09675.x.

Dai, X., G. Chartas, M. Eracleous, and G. P. Garmire (2004), A Study of Quasar Evolution in the X-Ray Band with the Aid of Gravitational Lensing, *ApJ*, *605*, 45–57, doi:10.1086/382205.

de Gasperin, F., A. Merloni, P. Sell, P. Best, S. Heinz, and G. Kauffmann (2011), Testing black hole jet scaling relations in low-luminosity active galactic nuclei, *MNRAS*, *415*, 2910–2919, doi:10.1111/j.1365-2966.2011.18904.x.

Denney, K. D., et al. (2010), Reverberation Mapping Measurements of Black Hole Masses in Six Local Seyfert Galaxies, *ApJ*, *721*, 715–737, doi:10.1088/0004-637X/721/1/715.

Di Matteo, T., A. Celotti, and A. C. Fabian (1999), Magnetic flares in accretion disc coronae and the spectral states of black hole candidates: the case of GX339-4, *MNRAS*, *304*, 809–820, doi:10.1046/j.1365-8711.1999.02375.x.

Di Matteo, T., S. W. Allen, A. C. Fabian, A. S. Wilson, and A. J. Young (2003), Accretion onto the Supermassive Black Hole in M87, *ApJ*, *582*, 133–140, doi:10.1086/344504.

Di Matteo, T., V. Springel, and L. Hernquist (2005), Energy input from quasars regulates the growth and activity of black holes and their host galaxies, *Nature*, *433*, 604–607, doi:10.1038/nature03335.

Dickey, J. M., and F. J. Lockman (1990), H I in the Galaxy, *ARA&A*, *28*, 215–261, doi:10.1146/annurev.aa.28.090190.001243.

Doeleman, S. S., et al. (2012), Jet-Launching Structure Resolved Near the Supermassive Black Hole in M87, *Science*, *338*, 355–, doi:10.1126/science.1224768.

Dorodnitsyn, A., T. Kallman, and D. Proga (2008), An Axisymmetric, Hydrodynamical Model for the Torus Wind in Active Galactic Nuclei. II. X-Ray-Excited Funnel Flow, *ApJ*, *687*, 97–110, doi:10.1086/591418.

Dunn, J. P., M. Bautista, N. Arav, M. Moe, K. Korista, E. Costantini, C. Benn, S. Ellison, and D. Edmonds (2010), The Quasar Outflow Contribution to AGN Feedback: VLT Measurements of SDSS J0318-0600, *ApJ*, *709*, 611–631, doi:10.1088/0004-637X/709/2/611.

Dunn, R. J. H., and A. C. Fabian (2004), Particle energies and filling fractions of radio bubbles in cluster cores, *MNRAS*, *355*, 862–873, doi:10.1111/j.1365-2966.2004.08365.x.

Ebrero, J., et al. (2011), Multiwavelength campaign on Mrk 509. V. Chandra-LETGS observation of the ionized absorber, *A&A*, *534*, A40, doi:10.1051/0004-6361/201117067.

Elvis, M., G. Risaliti, F. Nicastro, J. M. Miller, F. Fiore, and S. Puccetti (2004), An Unveiling Event in the Type 2 Active Galactic Nucleus NGC 4388:A Challenge for a Parsec-Scale Absorber, *ApJ*, *615*, L25–L28, doi:10.1086/424380.

Evans, D. A., D. M. Worrall, M. J. Hardcastle, R. P. Kraft, and M. Birkinshaw (2006), Chandra and XMM-Newton Observations of a Sample of Low-Redshift FR I and FR II Radio Galaxy Nuclei, *ApJ*, *642*, 96–112, doi:10.1086/500658.

Fabian, A. C. (2012), Observational Evidence of Active Galactic Nuclei Feedback, *ARA&A*, *50*, 455–489, doi:10.1146/annurev-astro-081811-125521.

Fabian, A. C., C. S. Crawford, A. C. Edge, and R. F. Mushotzky (1994), Cooling flows and the X-ray luminosity-temperature relation for clusters, *MNRAS*, *267*, 779.

Fabian, A. C., R. V. Vasudevan, R. F. Mushotzky, L. M. Winter, and C. S. Reynolds (2009), Radiation pressure and absorption in AGN: results from a complete unbiased sample from Swift, *MNRAS*, *394*, L89–L92, doi:10.1111/j.1745-3933.2009.00617.x.

Fabian, A. C., M. L. Parker, D. R. Wilkins, J. M. Miller, E. Kara, C. S. Reynolds, and T. Dauser (2014), On the determination of the spin and disc truncation of accreting black holes using X-ray reflection, *MNRAS*, *439*, 2307–2313, doi: 10.1093/mnras/stu045.

Falcke, H., E. Körding, and S. Markoff (2004a), A scheme to unify low-power accreting black holes. Jet-dominated accretion flows and the radio/X-ray correlation, *A&A*, *414*, 895–903, doi:10.1051/0004-6361:20031683.

Falcke, H., E. Körding, and N. M. Nagar (2004b), Compact radio cores: from the first black holes to the last, *nar*, *48*, 1157–1171, doi:10.1016/j.newar.2004.09.029.

Fanaroff, B. L., and J. M. Riley (1974), The morphology of extragalactic radio sources of high and low luminosity, *MNRAS*, *167*, 31P–36P.

Fender, R., and T. Belloni (2012), Stellar-Mass Black Holes and Ultraluminous X-ray Sources, *Science*, *337*, 540–, doi:10.1126/science.1221790.

Fender, R. P., A. M. Stirling, R. E. Spencer, I. Brown, G. G. Pooley, T. W. B. Muxlow, and J. C. A. Miller-Jones (2006), A transient relativistic radio jet from Cygnus X-1, *MNRAS*, *369*, 603–607, doi:10.1111/j.1365-2966.2006.10193.x.

Ferland, G. J., K. T. Korista, D. A. Verner, J. W. Ferguson, J. B. Kingdon, and E. M. Verner (1998), CLOUDY 90: Numerical Simulation of Plasmas and Their Spectra, *PASP*, *110*, 761–778, doi:10.1086/316190.

Foellmi, C. (2009), What is the closest black hole to the Sun?, *NA*, *14*, 674–691, doi:10.1016/j.newast.2009.04.003.

Fruscione, A., et al. (2006), CIAO: Chandra's data analysis system, in *Society of Photo-Optical Instrumentation Engineers (SPIE) Conference Series*, *Society of Photo-Optical Instrumentation Engineers (SPIE) Conference Series*, vol. 6270, doi: 10.1117/12.671760.

Gallo, E., R. P. Fender, and G. G. Pooley (2003), A universal radio-X-ray correlation in low/hard state black hole binaries, *MNRAS*, *344*, 60–72, doi:10.1046/j.1365-8711.2003.06791.x.

Gallo, E., R. Fender, C. Kaiser, D. Russell, R. Morganti, T. Oosterloo, and S. Heinz (2005), A dark jet dominates the power output of the stellar black hole Cygnus X-1, *Nature*, *436*, 819–821, doi:10.1038/nature03879.

Gallo, E., B. P. Miller, and R. Fender (2012), Assessing luminosity correlations via cluster analysis: evidence for dual tracks in the radio/X-ray domain of black hole X-ray binaries, *MNRAS*, *423*, 590–599, doi:10.1111/j.1365-2966.2012.20899.x.

Gandhi, P., et al. (2010), Rapid optical and X-ray timing observations of GX339-4: multicomponent optical variability in the low/hard state, *MNRAS*, *407*, 2166–2192, doi:10.1111/j.1365-2966.2010.17083.x.

Gaspari, M., F. Brighenti, A. D'Ercole, and C. Melioli (2011), AGN feedback in galaxy groups: the delicate touch of self-regulated outflows, *MNRAS*, *415*, 1549–1568, doi:10.1111/j.1365-2966.2011.18806.x.

George, I. M., T. J. Turner, H. Netzer, K. Nandra, R. F. Mushotzky, and T. Yaqoob (1998), ASCA Observations of Seyfert 1 Galaxies. III. The Evidence for Absorption and Emission Due to Photoionized Gas, *ApJS*, *114*, 73, doi:10.1086/313067.

Ghisellini, G., and A. Celotti (2001), The dividing line between FR I and FR II radio-galaxies, *A&A*, *379*, L1–L4, doi:10.1051/0004-6361:20011338.

Gibson, R. R., et al. (2009), A Catalog of Broad Absorption Line Quasars in Sloan Digital Sky Survey Data Release 5, *ApJ*, *692*, 758–777, doi:10.1088/0004-637X/692/1/758.

Giroletti, M., and F. Panessa (2009), The faintest seyfert radio cores revealed by vlbi, *ApJ*, *706*(2), L260–L264.

Giustini, M., and D. Proga (2012), On the diversity and complexity of absorption line profiles produced by outflows in Active Galactic Nuclei, *ArXiv e-prints*.

Greiner, J., J. G. Cuby, and M. J. McCaughrean (2001), An unusually massive stellar black hole in the Galaxy, *Nature*, *414*, 522–525.

Gültekin, K., E. M. Cackett, J. M. Miller, T. Di Matteo, S. Markoff, and D. O. Richstone (2009a), The Fundamental Plane of Accretion onto Black Holes with Dynamical Masses, *ApJ*, *706*, 404–416, doi:10.1088/0004-637X/706/1/404.

Gültekin, K., et al. (2009b), The M-σ and M-L Relations in Galactic Bulges, and Determinations of Their Intrinsic Scatter, *ApJ*, *698*, 198–221, doi:10.1088/0004-637X/698/1/198.

Haehnelt, M. G., and G. Kauffmann (2000), The correlation between black hole mass and bulge velocity dispersion in hierarchical galaxy formation models, *MNRAS*, *318*, L35–L38, doi:10.1046/j.1365-8711.2000.03989.x.

Hardcastle, M. J., D. A. Evans, and J. H. Croston (2006), The X-ray nuclei of intermediate-redshift radio sources, *MNRAS*, *370*, 1893–1904, doi:10.1111/j.1365-2966.2006.10615.x.

Hardcastle, M. J., D. A. Evans, and J. H. Croston (2009), The active nuclei of z < 1.0 3CRR radio sources, *MNRAS*, *396*, 1929–1952, doi:10.1111/j.1365-2966.2009.14887.x.

Harlaftis, E. T., and J. Greiner (2004), The rotational broadening and the mass of the donor star of GRS 1915+105, *A&A*, *414*, L13–L16, doi:10.1051/0004-6361:20031754.

Heinz, S., and M. C. Begelman (2000), Jet Acceleration by Tangled Magnetic Fields, *ApJ*, *535*, 104–117, doi:10.1086/308820.

Heinz, S., Y.-Y. Choi, C. S. Reynolds, and M. C. Begelman (2002), Chandra ACIS-S Observations of Abell 4059: Signs of Dramatic Interaction between a Radio Galaxy and a Galaxy Cluster, *ApJ*, *569*, L79–L82, doi:10.1086/340688.

Hjellming, R. M., and M. P. Rupen (1995), Episodic ejection of relativistic jets by the X-ray transient GRO J1655 - 40, *Nature*, *375*, 464–468, doi:10.1038/375464a0.

Homan, J., J. M. Miller, R. Wijnands, M. van der Klis, T. Belloni, D. Steeghs, and W. H. G. Lewin (2005), High- and Low-Frequency Quasi-periodic Oscillations in the X-Ray Light Curves of the Black Hole Transient H1743-322, *ApJ*, *623*, 383–391, doi:10.1086/424994.

Hopkins, P. F., and M. Elvis (2010), Quasar feedback: more bang for your buck, *MNRAS*, *401*, 7–14, doi:10.1111/j.1365-2966.2009.15643.x.

Hopkins, P. F., L. Hernquist, T. J. Cox, T. Di Matteo, P. Martini, B. Robertson, and V. Springel (2005), Black Holes in Galaxy Mergers: Evolution of Quasars, *ApJ*, *630*, 705–715, doi:10.1086/432438.

Iwasawa, K., Y. Tanaka, and L. C. Gallo (2010), The Suzaku broadband X-ray spectrum of the dwarf Seyfert galaxy NGC 4395, *A&A*, *514*, A58, doi:10.1051/0004-6361/200912431.

Jones, S., I. McHardy, D. Moss, N. Seymour, E. Breedt, P. Uttley, E. Körding, and V. Tudose (2011), Radio and X-ray variability in the Seyfert galaxy NGC 4051, *MNRAS*, *412*, 2641–2652, doi:10.1111/j.1365-2966.2010.18105.x.

Kalberla, P. M. W., W. B. Burton, D. Hartmann, E. M. Arnal, E. Bajaja, R. Morras, and W. G. L. Pöppel (2005), The Leiden/Argentine/Bonn (LAB) Survey of Galactic HI. Final data release of the combined LDS and IAR surveys with improved stray-radiation corrections, *A&A*, *440*, 775–782, doi:10.1051/0004-6361:20041864.

Kallman, T., and M. Bautista (2001), Photoionization and High-Density Gas, *ApJS*, *133*, 221–253, doi:10.1086/319184.

Kallman, T. R., M. A. Bautista, S. Goriely, C. Mendoza, J. M. Miller, P. Palmeri, P. Quinet, and J. Raymond (2009), Spectrum Synthesis Modeling of the X-Ray Spectrum of GRO J1655-40 Taken During the 2005 Outburst, *ApJ*, *701*, 865–884, doi:10.1088/0004-637X/701/2/865.

Kaspi, S., et al. (2002), The Ionized Gas and Nuclear Environment in NGC 3783. I. Time-averaged 900 Kilosecond Chandra Grating Spectroscopy, *ApJ*, *574*, 643–662, doi:10.1086/341113.

King, A. L., J. M. Miller, E. M. Cackett, A. C. Fabian, S. Markoff, M. A. Nowak, M. Rupen, K. Gültekin, and M. T. Reynolds (2011), A Distinctive Disk-Jet Coupling in the Seyfert-1 Active Galactic Nucleus NGC 4051, *ApJ*, *729*, 19, doi: 10.1088/0004-637X/729/1/19.

King, A. L., J. M. Miller, and J. Raymond (2012a), Warm Absorbers and Outflows in the Seyfert-1 Galaxy NGC 4051, *ApJ*, *746*, 2.

King, A. L., J. M. Miller, J. Raymond, A. C. Fabian, C. S. Reynolds, T. R. Kallman, D. Maitra, E. M. Cackett, and M. P. Rupen (2012b), An Extreme X-Ray Disk Wind in the Black Hole Candidate IGR J17091−3624, *ApJ*, *746*, L20, doi:10.1088/2041-8205/746/2/L20.

King, A. L., J. M. Miller, and K. Gültekin (2013a), Magnetic flux Paradigm in Neutron Stars, *ApJ*, in Prep.

King, A. L., J. M. Miller, M. T. Reynolds, K. Gültekin, E. Gallo, and D. Maitra (2013b), A Distinctive Disk-Jet Coupling in the Lowest-mass Seyfert, NGC 4395, *ApJ*, *774*, L25, doi:10.1088/2041-8205/774/2/L25.

King, A. L., et al. (2013c), Regulation of Black Hole Winds and Jets across the Mass Scale, *ApJ*, *762*, 103, doi:10.1088/0004-637X/762/2/103.

Körding, E. G., S. Jester, and R. Fender (2006), Accretion states and radio loudness in active galactic nuclei: analogies with X-ray binaries, *MNRAS*, *372*, 1366–1378, doi:10.1111/j.1365-2966.2006.10954.x.

Kraemer, S. B., et al. (2005), Simultaneous Ultraviolet and X-Ray Observations of Seyfert Galaxy NGC 4151. I. Physical Conditions in the X-Ray Absorbers, *ApJ*, *633*, 693–705, doi:10.1086/466522.

Krimm, H. A., et al. (2011), Swift/BAT reports renewed activity from IGR J17091-3624, *The Astronomer's Telegram*, *3144*, 1.

Krolik, J. H., and J. F. Hawley (2010), General Relativistic MHD Jets, in *Lecture Notes in Physics, Berlin Springer Verlag*, *Lecture Notes in Physics, Berlin Springer Verlag*, vol. 794, edited by T. Belloni, p. 265, doi:10.1007/978-3-540-76937-8-10.

Krongold, Y., F. Nicastro, M. Elvis, N. Brickhouse, L. Binette, S. Mathur, and E. Jiménez-Bailón (2007), The Compact, Conical, Accretion-Disk Warm Absorber of the Seyfert 1 Galaxy NGC 4051 and Its Implications for IGM-Galaxy Feedback Processes, *ApJ*, *659*, 1022–1039, doi:10.1086/512476.

Kubota, A., et al. (2007), Suzaku Discovery of Iron Absorption Lines in Outburst Spectra of the X-Ray Transient 4U 1630-472, *PASJ*, *59*, 185–198.

Lee, J. C. (2005), Black Hole Systems Seen at High Spectral Resolution: Inflow and Outflow, *Ap&SS*, *300*, 67–70, doi:10.1007/s10509-005-1191-x.

Lira, P., A. Lawrence, P. O'Brien, R. A. Johnson, R. Terlevich, and N. Bannister (1999), Optical and X-ray variability in the least luminous active galactic nucleus, NGC 4395, *MNRAS*, *305*, 109–124, doi:10.1046/j.1365-8711.1999.02388.x.

Loeb, A. (2005), The Environmental Impact of Supermassive Black Holes, in *Growing Black Holes: Accretion in a Cosmological Context*, edited by A. Merloni, S. Nayakshin, and R. A. Sunyaev, pp. 18–29, doi:10.1007/11403913-2.

Lovelace, R. V. E. (1976), Dynamo model of double radio sources, *Nature*, *262*, 649–652, doi:10.1038/262649a0.

Luketic, S., D. Proga, T. R. Kallman, J. C. Raymond, and J. M. Miller (2010), On the Properties of Thermal Disk Winds in X-ray Transient Sources: A Case Study of GRO J1655-40, *ApJ*, *719*, 515–522, doi:10.1088/0004-637X/719/1/515.

Maitra, D., S. Markoff, and H. Falcke (2009), A time-dependent jet model for the emission from Sagittarius A*, *A&A*, *508*, L13–L16, doi:10.1051/0004-6361/200913163.

Maitra, D., J. M. Miller, S. Markoff, and A. King (2011), A Jet Model for the Broadband Spectrum Of the Seyfert 1 Galaxy NGC 4051, *ApJ*, *735*, 107, doi:10.1088/0004-637X/735/2/107.

Marti, J., L. F. Rodriguez, I. F. Mirabel, and J. M. Paredes (1996), A search for arcminute-scale radio jets in Cygnus X-1., *A&A*, *306*, 449.

McHardy, I. M., K. F. Gunn, P. Uttley, and M. R. Goad (2005), MCG-6-30-15: long time-scale X-ray variability, black hole mass and active galactic nuclei high states, *MNRAS*, *359*, 1469–1480, doi:10.1111/j.1365-2966.2005.08992.x.

McKernan, B., T. Yaqoob, and C. S. Reynolds (2007), A soft X-ray study of type I active galactic nuclei observed with Chandra high-energy transmission grating spectrometer, *MNRAS*, *379*, 1359–1372, doi:10.1111/j.1365-2966.2007.11993.x.

McLure, R. J., and M. J. Jarvis (2004), The relationship between radio luminosity and black hole mass in optically selected quasars, *MNRAS*, *353*, L45–L49, doi:10.1111/j.1365-2966.2004.08305.x.

McMullin, J. P., B. Waters, D. Schiebel, W. Young, and K. Golap (2007), CASA Architecture and Applications, in *Astronomical Data Analysis Software and Systems XVI*, *Astronomical Society of the Pacific Conference Series*, vol. 376, edited by R. A. Shaw, F. Hill, and D. J. Bell, p. 127.

McNamara, B. R., M. Rohanizadegan, and P. E. J. Nulsen (2011), Are Radio Active Galactic Nuclei Powered by Accretion or Black Hole Spin?, *ApJ*, *727*, 39, doi:10.1088/0004-637X/727/1/39.

Merloni, A., and S. Heinz (2007), Measuring the kinetic power of active galactic nuclei in the radio mode, *mnras*, *381*, 589–601, doi:10.1111/j.1365-2966.2007.12253.x.

Merloni, A., S. Heinz, and T. di Matteo (2003), A Fundamental Plane of black hole activity, *mnras*, *345*, 1057–1076, doi:10.1046/j.1365-2966.2003.07017.x.

Meyer, E. T., G. Fossati, M. Georganopoulos, and M. L. Lister (2011), From the Blazar Sequence to the Blazar Envelope: Revisiting the Relativistic Jet Dichotomy in Radio-loud Active Galactic Nuclei, *ApJ*, *740*, 98, doi:10.1088/0004-637X/740/2/98.

Migliari, S., J. A. Tomsick, S. Markoff, E. Kalemci, C. D. Bailyn, M. Buxton, S. Corbel, R. P. Fender, and P. Kaaret (2007), Tracing the Jet Contribution to the Mid-IR over the 2005 Outburst of GRO J1655-40 via Broadband Spectral Modeling, *ApJ*, *670*, 610–623, doi:10.1086/522023.

Miller, J. M., J. Raymond, A. Fabian, D. Steeghs, J. Homan, C. Reynolds, M. van der Klis, and R. Wijnands (2006a), The magnetic nature of disk accretion onto black holes, *Nature*, *441*, 953–955, doi:10.1038/nature04912.

Miller, J. M., J. Raymond, C. S. Reynolds, A. C. Fabian, T. R. Kallman, and J. Homan (2008), The Accretion Disk Wind in the Black Hole GRO J1655-40, *ApJ*, *680*, 1359–1377, doi:10.1086/588521.

Miller, J. M., J. Raymond, A. C. Fabian, C. S. Reynolds, A. L. King, T. R. Kallman, E. M. Cackett, M. van der Klis, and D. T. H. Steeghs (2012), The Disk-Wind-Jet Connection in the Black Hole H 1743-322, *ArXiv e-prints*.

Miller, J. M., et al. (2006b), Simultaneous Chandra and RXTE Spectroscopy of the Microquasar H1743-322: Clues to Disk Wind and Jet Formation from a Variable Ionized Outflow, *ApJ*, *646*, 394–406, doi:10.1086/504673.

Miller, K. A., and J. M. Stone (2000), The Formation and Structure of a Strongly Magnetized Corona above a Weakly Magnetized Accretion Disk, *ApJ*, *534*, 398–419, doi:10.1086/308736.

Miller-Jones, J. C. A., et al. (2012), Disc-jet coupling in the 2009 outburst of the black hole candidate H1743-322, *MNRAS*, *421*, 468–485, doi:10.1111/j.1365-2966.2011.20326.x.

Miniutti, G., et al. (2014), The properties of the clumpy torus and BLR in the polar-scattered Seyfert 1 galaxy ESO 323-G77 through X-ray absorption variability, *MNRAS*, *437*, 1776–1790, doi:10.1093/mnras/stt2005.

Mirabel, I. F., and L. F. Rodríguez (1999), Sources of Relativistic Jets in the Galaxy, *ARA&A*, *37*, 409–443, doi:10.1146/annurev.astro.37.1.409.

Mirabel, I. F., V. Dhawan, S. Chaty, L. F. Rodriguez, J. Marti, C. R. Robinson, J. Swank, and T. Geballe (1998), Accretion instabilities and jet formation in GRS 1915+105, *A&A*, *330*, L9–L12.

Mocz, P., J. C. Lee, K. Iwasawa, and C. R. Canizares (2011), A Detection of an X-ray Wind and an Ionized Disk in the Chandra HETGS Observation of the Seyfert 2 Galaxy IRAS 18325-5926, *ApJ*, *729*, 30, doi:10.1088/0004-637X/729/1/30.

Moderski, R., M. Sikora, and J.-P. Lasota (1998), On the spin paradigm and the radio dichotomy of quasars, *MNRAS*, *301*, 142–148, doi:10.1046/j.1365-8711.1998.02009.x.

Moe, M., N. Arav, M. A. Bautista, and K. T. Korista (2009), Quasar Outflow Contribution to AGN Feedback: Observations of QSO SDSS J0838+2955, *ApJ*, *706*, 525–534, doi:10.1088/0004-637X/706/1/525.

Moran, E. C., M. Eracleous, K. M. Leighly, G. Chartas, A. V. Filippenko, L. C. Ho, and P. R. Blanco (2005), Extreme X-Ray Behavior of the Low-Luminosity Active Nucleus in NGC 4395, *AJ*, *129*, 2108–2118, doi:10.1086/429522.

Mortlock, D. J., et al. (2011), A luminous quasar at a redshift of z = 7.085, *Nature*, *474*, 616–619, doi:10.1038/nature10159.

Narayan, R., and J. E. McClintock (2008), Advection-dominated accretion and the black hole event horizon, *New Astronomy Review*, *51*, 733–751, doi: 10.1016/j.newar.2008.03.002.

Nardini, E., and G. Risaliti (2011), The effects of X-ray absorption variability in NGC 4395, *MNRAS*, *417*, 2571–2576, doi:10.1111/j.1365-2966.2011.19423.x.

Neilsen, J., and J. Homan (2012), A Hybrid Magnetically/Thermally Driven Wind in the Black Hole GRO J1655-40?, *ApJ*, *750*, 27, doi:10.1088/0004-637X/750/1/27.

Neilsen, J., and J. C. Lee (2009), Accretion disk winds as the jet suppression mechanism in the microquasar GRS 1915+105, *Nature*, *458*, 481–484, doi: 10.1038/nature07680.

Neilsen, J., and J. C. Lee (2010), The Chandra HETGS View Of The Disk-jet Connection In The Microquasar GRS 1915+105, in *American Astronomical Society Meeting Abstracts #215*, *Bulletin of the American Astronomical Society*, vol. 42, p. 371.04.

Ohsuga, K., and S. Mineshige (2011), Global Structure of Three Distinct Accretion Flows and Outflows around Black Holes from Two-dimensional Radiation-magnetohydrodynamic Simulations, *ApJ*, *736*, 2, doi:10.1088/0004-637X/736/1/2.

Orosz, J. A., and C. D. Bailyn (1997), Optical Observations of GRO J1655-40 in Quiescence. I. A Precise Mass for the Black Hole Primary, *ApJ*, *477*, 876, doi: 10.1086/303741.

Ostriker, J. P., E. Choi, L. Ciotti, G. S. Novak, and D. Proga (2010), Momentum Driving: Which Physical Processes Dominate Active Galactic Nucleus Feedback?, *ApJ*, *722*, 642–652, doi:10.1088/0004-637X/722/1/642.

Peres, C. B., A. C. Fabian, A. C. Edge, S. W. Allen, R. M. Johnstone, and D. A. White (1998), A ROSAT study of the cores of clusters of galaxies - I. Cooling flows in an X-ray flux-limited sample, *MNRAS*, *298*, 416–432, doi:10.1046/j.1365-8711.1998.01624.x.

Perley, R. A., and B. J. Butler (2013), An Accurate Flux Density Scale from 1 to 50 GHz, *ApJS*, *204*, 19, doi:10.1088/0067-0049/204/2/19.

Peterson, B. M., et al. (2004), Central Masses and Broad-Line Region Sizes of Active Galactic Nuclei. II. A Homogeneous Analysis of a Large Reverberation-Mapping Database, *ApJ*, *613*, 682–699, doi:10.1086/423269.

Peterson, B. M., et al. (2005), Multiwavelength Monitoring of the Dwarf Seyfert 1 Galaxy NGC 4395. I. A Reverberation-based Measurement of the Black Hole Mass, *ApJ*, *632*, 799–808, doi:10.1086/444494.

Plotkin, R. M., S. Markoff, B. C. Kelly, E. Körding, and S. F. Anderson (2012), Using the Fundamental Plane of black hole activity to distinguish X-ray processes from weakly accreting black holes, *MNRAS*, *419*, 267–286, doi:10.1111/j.1365-2966.2011.19689.x.

Ponti, G., R. P. Fender, M. C. Begelman, R. J. Dunn, J. Neilsen, and M. Coriat (2012), Ubiquitous Equatorial Accretion Disc Winds in Black Hole Soft States, *MNRAS*, submitted.

Press, W. H., S. A. Teukolsky, W. T. Vetterling, and B. P. Flannery (1992), *Numerical recipes in FORTRAN. The art of scientific computing.*

Proga, D. (2000), Winds from Accretion Disks Driven by Radiation and Magnetocentrifugal Force, *ApJ*, *538*, 684–690, doi:10.1086/309154.

Proga, D. (2002), Dynamics of Line-Driven Disk Winds, in *Mass Outflow in Active Galactic Nuclei: New Perspectives*, *Astronomical Society of the Pacific Conference Series*, vol. 255, edited by D. M. Crenshaw, S. B. Kraemer, and I. M. George, p. 309.

Proga, D. (2003), Numerical Simulations of Mass Outflows Driven from Accretion Disks by Radiation and Magnetic Forces, *ApJ*, *585*, 406–417, doi:10.1086/345897.

Proga, D., and T. R. Kallman (2002), On the Role of the Ultraviolet and X-Ray Radiation in Driving a Disk Wind in X-Ray Binaries, *ApJ*, *565*, 455–470, doi:10.1086/324534.

Proga, D., J. M. Stone, and T. R. Kallman (2000), Dynamics of Line-driven Disk Winds in Active Galactic Nuclei, *ApJ*, *543*, 686–696, doi:10.1086/317154.

Protassov, R., D. A. van Dyk, A. Connors, V. L. Kashyap, and A. Siemiginowska (2002), Statistics, Handle with Care: Detecting Multiple Model Components with the Likelihood Ratio Test, *ApJ*, *571*, 545–559, doi:10.1086/339856.

Raymond, J. C. (1993), A model of an X-ray-illuminated accretion disk and corona, *ApJ*, *412*, 267–277, doi:10.1086/172917.

Raymond, J. C., J. J. Hester, D. Cox, W. P. Blair, R. A. Fesen, and T. R. Gull (1988), Spatial and spectral interpretation of a bright filament in the Cygnus Loop, *ApJ*, *324*, 869–892, doi:10.1086/165945.

Reid, M. J., J. E. McClintock, R. Narayan, L. Gou, R. A. Remillard, and J. A. Orosz (2011), The Trigonometric Parallax of Cygnus X-1, *ApJ*, *742*, 83, doi:10.1088/0004-637X/742/2/83.

Reis, R. C., M. T. Reynolds, J. M. Miller, and D. J. Walton (2014), Reflection from the strong gravity regime in a lensed quasar at redshift z = 0.658, *Nature*, *507*, 207–209, doi:10.1038/nature13031.

Reynolds, C. S. (1997), An X-ray spectral study of 24 type 1 active galactic nuclei, *MNRAS*, *286*, 513–537.

Reynolds, C. S., D. Garofalo, and M. C. Begelman (2006), Trapping of Magnetic Flux by the Plunge Region of a Black Hole Accretion Disk, *ApJ*, *651*, 1023–1030, doi:10.1086/507691.

Richstone, D., et al. (1998), Supermassive black holes and the evolution of galaxies., *Nature*, *395*, A14.

Risaliti, G., et al. (2009), Variable Partial Covering and A Relativistic Iron Line in NGC 1365, *ApJ*, *696*, 160–171, doi:10.1088/0004-637X/696/1/160.

Rodriguez, J., S. Corbel, I. Caballero, J. A. Tomsick, T. Tzioumis, A. Paizis, M. Cadolle Bel, and E. Kuulkers (2011), First simultaneous multi-wavelength observations of the black hole candidate IGR J17091-3624. ATCA, INTEGRAL, Swift, and RXTE views of the 2011 outburst, *A&A*, *533*, L4, doi:10.1051/0004-6361/201117511.

Russell, D. M., R. P. Fender, E. Gallo, and C. R. Kaiser (2007), The jet-powered optical nebula of Cygnus X-1, *MNRAS*, *376*, 1341–1349, doi:10.1111/j.1365-2966.2007.11539.x.

Russell, D. M., E. Gallo, and R. P. Fender (2013), Observational constraints on the powering mechanism of transient relativistic jets, *MNRAS*, *431*, 405–414, doi:10.1093/mnras/stt176.

Sako, M., D. A. Liedahl, S. M. Kahn, and F. Paerels (1999), The X-Ray Spectrum and Global Structure of the Stellar Wind in VELA X-1, *ApJ*, *525*, 921–934, doi:10.1086/307924.

Shahbaz, T., F. van der Hooft, J. Casares, P. A. Charles, and J. van Paradijs (1999), The mass of X-ray Nova Scorpii1994 (=GRO J1655-40), *MNRAS*, *306*, 89–94, doi: 10.1046/j.1365-8711.1999.02481.x.

Shakura, N. I., and R. A. Sunyaev (1973), Black holes in binary systems. Observational appearance., *A&A*, *24*, 337–355.

Shih, D. C., K. Iwasawa, and A. C. Fabian (2003), Evidence for an intermediate-mass black hole and a multi-zone warm absorber in NGC 4395, *MNRAS*, *341*, 973–980, doi:10.1046/j.1365-8711.2003.06482.x.

Soltan, A. (1982), Masses of quasars, *MNRAS*, *200*, 115–122.

Steeghs, D., J. M. Miller, D. Kaplan, and M. Rupen (2003), IGR/XTE J17464-3213: New radio position and optical counterpart, *The Astronomer's Telegram*, *146*, 1.

Steenbrugge, K. C., J. S. Kaastra, A. J. Blustin, G. Branduardi-Raymont, M. Sako, E. Behar, S. M. Kahn, F. B. S. Paerels, and R. Walter (2003), Chandra LETGS and XMM-Newton observations of NGC 4593, *A&A*, *408*, 921–928, doi:10.1051/0004-6361:20031021.

Steiner, J. F., J. E. McClintock, and M. J. Reid (2012), The Distance, Inclination, and Spin of the Black Hole Microquasar H1743-322, *ApJ*, *745*, L7, doi:10.1088/2041-8205/745/1/L7.

Steiner, J. F., J. E. McClintock, and R. Narayan (2013), Jet Power and Black Hole Spin: Testing an Empirical Relationship and Using it to Predict the Spins of Six Black Holes, *ApJ*, *762*, 104, doi:10.1088/0004-637X/762/2/104.

Taylor, G. B., J. S. Sanders, A. C. Fabian, and S. W. Allen (2006), The low-power nucleus of PKS 1246-410 in the Centaurus cluster, *MNRAS*, *365*, 705–711, doi: 10.1111/j.1365-2966.2005.09705.x.

Tombesi, F., R. M. Sambruna, J. N. Reeves, V. Braito, L. Ballo, J. Gofford, M. Cappi, and R. F. Mushotzky (2010), Discovery of Ultra-fast Outflows in a Sample of Broad-line Radio Galaxies Observed with Suzaku, *ApJ*, *719*, 700–715, doi:10.1088/0004-637X/719/1/700.

Tombesi, F., R. M. Sambruna, J. N. Reeves, C. S. Reynolds, and V. Braito (2011), X-ray evidence for the accretion disc-outflow connection in 3C 111, *MNRAS*, *418*, L89–L93, doi:10.1111/j.1745-3933.2011.01149.x.

Tombesi, F., M. Cappi, J. N. Reeves, R. S. Nemmen, V. Braito, M. Gaspari, and C. S. Reynolds (2013), Unification of X-ray winds in Seyfert galaxies: from ultra-fast outflows to warm absorbers, *MNRAS*, *430*, 1102–1117, doi:10.1093/mnras/sts692.

Tremaine, S., et al. (2002), The Slope of the Black Hole Mass versus Velocity Dispersion Correlation, *ApJ*, *574*, 740–753, doi:10.1086/341002.

Ueda, Y., H. Murakami, K. Yamaoka, T. Dotani, and K. Ebisawa (2004), Chandra High-Resolution Spectroscopy of the Absorption-Line Features in the Low-Mass X-Ray Binary GX 13+1, *ApJ*, *609*, 325–334, doi:10.1086/420973.

Ueda, Y., K. Yamaoka, and R. Remillard (2009), GRS 1915+105 in "Soft State": Nature of Accretion Disk Wind and Origin of X-ray Emission, *ApJ*, *695*, 888–899, doi:10.1088/0004-637X/695/2/888.

Urry, C. M., and P. Padovani (1991), Altered luminosity functions for relativistically beamed objects. II - Distribution of Lorentz factors and parent populations with complex luminosity functions, *ApJ*, *371*, 60–68, doi:10.1086/169870.

Vasudevan, R. V., and A. C. Fabian (2009), Simultaneous X-ray/optical/UV snapshots of active galactic nuclei from XMM-Newton: spectral energy distributions for the reverberation mapped sample, *MNRAS*, *392*, 1124–1140, doi:10.1111/j.1365-2966.2008.14108.x.

Verner, D. A., E. M. Verner, and G. J. Ferland (1996), Atomic Data for Permitted Resonance Lines of Atoms and Ions from H to Si, and S, Ar, Ca, and Fe, *Atomic Data and Nuclear Data Tables*, *64*, 1, doi:10.1006/adnd.1996.0018.

Vierdayanti, K., S. Mineshige, and Y. Ueda (2010), Probing the Peculiar Behavior of GRS 1915+105 at Near-Eddington Luminosity, *PASJ*, *62*, 239–.

Volonteri, M. (2012), The Formation and Evolution of Massive Black Holes, *Science*, *337*, 544–, doi:10.1126/science.1220843.

Weaver, R., R. McCray, J. Castor, P. Shapiro, and R. Moore (1977), Interstellar bubbles. II - Structure and evolution, *ApJ*, *218*, 377–395, doi:10.1086/155692.

Woods, D. T., R. I. Klein, J. I. Castor, C. F. McKee, and J. B. Bell (1996), X-Ray–heated Coronae and Winds from Accretion Disks: Time-dependent Two-dimensional Hydrodynamics with Adaptive Mesh Refinement, *ApJ*, *461*, 767, doi:10.1086/177101.

Wrobel, J. M., and L. C. Ho (2006), Radio Emission on Subparsec Scales from the Intermediate-Mass Black Hole in NGC 4395, *ApJ*, *646*, L95–L98, doi:10.1086/507102.

Wu, Q., X. Cao, L. C. Ho, and D.-X. Wang (2013), A Physical Link between Jet Formation and Hot Plasma in Active Galactic Nuclei, *ApJ*, *770*, 31, doi:10.1088/0004-637X/770/1/31.

Wu, X.-B., and J. L. Han (2001), Inclinations and Black Hole Masses of Seyfert 1 Galaxies, *ApJ*, *561*, L59–L62, doi:10.1086/324408.

Yaqoob, T., B. McKernan, S. B. Kraemer, D. M. Crenshaw, J. R. Gabel, I. M. George, and T. J. Turner (2003), The Kinematics and Physical Conditions of the Ionized Gas in Markarian 509. I. Chandra High Energy Grating Spectroscopy, *ApJ*, *582*, 105–124, doi:10.1086/344541.

Zhang, S. N., Q. S. Gu, L. Ji, and Z. X. Peng (2011a), Serendipitous discovery of warm absorbes in Seyfert 2 galaxy IRAS 18325-5926, *Res. Astro. Astrophys.*, *11*, 1171–1184, doi:10.1111/j.1365-2966.2010.17595.x.

Zhang, S. N., L. Ji, H. L. Marshall, A. L. Longinotti, D. Evans, and Q. S. Gu (2011b), Chandra and XMM-Newton view of the warm absorbing gas in Mrk 290, *MNRAS*, *410*, 2274–2290, doi:10.1111/j.1365-2966.2010.17595.x.